

Technical Report

TR-19-19

September 2019



Earthquake simulations performed to assess the long-term safety of a KBS-3 repository

Overview and evaluation of results produced after SR-Site

Harald Hökmark

Billy Fälth

Margareta Lönnqvist

Raymond Munier

SVENSK KÄRNBRÄNSLEHANTERING AB

SWEDISH NUCLEAR FUEL
AND WASTE MANAGEMENT CO

Box 3091, SE-169 03 Solna
Phone +46 8 459 84 00
skb.se

SVENSK KÄRNBRÄNSLEHANTERING

ISSN 1404-0344

SKB TR-19-19

ID 1700766

September 2019

Earthquake simulations performed to assess the long-term safety of a KBS-3 repository

Overview and evaluation of results produced after SR-Site

Harald Hökmark, Billy Fälth, Margareta Lönnqvist
Clay Technology AB

Raymond Munier, Svensk Kärnbränslehantering AB

Keywords: Seismicity, Dynamic Simulations, Secondary Displacements, Critical radii, Safety margins.

A pdf version of this document can be downloaded from www.skb.se.

© 2019 Svensk Kärnbränslehantering AB

Abstract

One of the issues addressed in the latest SKB safety report (SR-Site) on the handling of spent nuclear fuel in deep geological repositories is the risk that spent fuel canisters could be damaged by seismically induced shear displacements (secondary slip) along repository host rock fractures that intersect canister positions. In SR-site so called critical radii, i.e. the radii of the smallest fractures that must be avoided when deciding on canister positions at different distances from differently sized potential earthquake faults, are specified.

The SR-Site critical radii are based on results of dynamic numerical simulations performed using models including the rupturing earthquake fault as well as a population of differently oriented host rock fractures (“target fractures”) located at different distances from the rupturing fault (the “primary fault”). None of the simulations included in the SR-Site background material are based on site data or on any specific load scenario, e.g. thermal or end-glacial loads.

After the publication of SR-Site the work on dynamic simulations of seismically induced slip along host rock fractures has been continued with site-specific input assumptions regarding in-situ stresses, thermal and glacial load additions, fault geometries etc. Models relevant to the Forsmark site as well models relevant to the Olkiluoto site in Finland have been analyzed and described in a number of studies (see reference list in this report). In the continued work it has been possible to take advantage of the steadily ongoing development of the numerical tool (the 3DEC code) and the steadily increasing computer capacity, which, in turn, has made it possible to perform relevant code benchmarks and to try, for instance, alternative and more realistic rupture models. It has also been possible to analyze larger models and to test the impact of different kinds of fault inhomogeneities.

In this overview the essence of the results of the many simulations performed within the continued work, is summarized and discussed, i.e:

- The moment magnitude and the rupture area of the synthetic 3DEC earthquakes.
- The resulting maximum target fracture slip at the different fault-fracture distances considered in the models.

A first overall conclusion is that the critical radii suggested in the SR-site background material are, with good margins, lower bounds. i.e. the results of the continued work appear to increase the confidence in the conservativeness of the SR-Site layout rules.

The results do, however, also point to the possibility of improving the Forsmark tunnel capacity utilization and to reconsider whether or not the modestly sized steeply dipping deformation zones located within or in the immediate vicinity of the Forsmark repository footprint would require more than very modest, if any at all, respect distances. As described in the last chapter of this overview, some work remains, however, to finally verify this.

Sammanfattning

Ett av problemen som adresseras i SKBs senaste säkerhetsrapport (SR-Site) rörande deponering av använt kärnbränsle i djupa geologiska förvar är risken för att kapslar med använt kärnbränsle skulle kunna skadas av seismiskt inducerade skjuvrörelser längs bergssprickor som skär igenom kapselpositioner. I SR-Site specificeras s.k. kritiska radier, d.v.s. radierna hos de minsta sprickorna som måste undvikas när man beslutar om kapselpositioner på olika avstånd från potentiella jordskalvszoner.

De kritiska radierna i SR-Site är baserade på resultat av dynamiska numeriska simuleringar som gjorts med modeller som inkluderar både den aktiva jordskalvszonen och en uppsättning bergssprickor ("målsprickor") med olika orienteringar och som befinner sig på olika avstånd från jordskalvszonen ("primärförkastningen"). Inga av de simuleringar som ingår SR-Site materialet är baserade på platsdata eller på något speciellt lastscenario, t ex termiska eller endglaciala laster.

Efter publiceringen av SR-Site har arbetet med dynamiska simuleringar av seismiskt inducerade rörelser längs sprickor i förvarsberget fortsatt med platspecifika antaganden gällande in-situ spänningar, termiska och glaciala spänningstillskott, geometrier hos förkastningsplan etc. Både modeller relevanta för Forsmark och modeller relevanta för Olkiluoto i Finland har analyserats och beskrivits i ett antal olika studier. I det fortsatta arbetet har det varit möjligt att dra fördel av den ständigt fortgående utvecklingen av beräkningsverktyget (3DEC-koden) och av den ständigt ökande beräkningskapaciteten vilket, i sin tur, har gjort det möjligt att genomföra relevanta benchmarks av koden och att testa, t ex, alternativa och mer realistiska brottpropageringsmekanismer. Det har också blivit möjligt att analysera större modeller och undersöka inverkan av olika typer av inhomogeniteter hos förkastningsplanet.

I denna översikt summeras och diskuteras essensen av resultaten av de många simuleringar som genomförts inom ramen för det fortsatta arbetet, dvs:

- Momentmagnituden och brottsarean hos de syntetiska 3DEC-skalven.
- De resulterande maxrörelserna hos målsprickorna på de olika avstånd från förkastningsplanet som ingår i de olika modellerna.

En första slutsats är att de kritiska radier som föreslås i SR-Site-materialet, med goda marginaler, kan betraktas som undre gränser. Resultaten av det fortsatta arbetet har alltså visat sig styrka tilltron till konservatismen i de layoutregler som gäller i SR-Site.

Resultaten pekar emellertid också på möjligheten att förbättra utnyttjandegraden av tunnlarna i Forsmark och att ompröva ifall de relativt små brantstående deformationszoner inom eller i den omedelbara närheten av förvarsområdet i Forsmark fordrar mer än mycket måttliga, om ens några överhuvudtaget, respektavstånd. Som beskrivs i det sista kapitlet av denna översikt, återstår en del arbete för att slutgiltigt verifiera detta.

Contents

1	Introduction and background	7
1.1	General	7
1.1	Problem statement	8
1.1.1	Primary fault displacements	9
1.1.2	Secondary displacements	11
2	Secondary displacements – numerical assessment	13
2.1	Early work	13
2.2	SR-Can and SR-Site	13
2.3	SR-Site critical radii and respect distances	14
3	Continued work	19
3.1	General	19
3.2	Comments on stress and stability	19
3.2.1	General	19
3.2.2	Glacially induced stresses	20
3.2.3	In-situ stress model and local Forsmark fault stability evolution	20
3.2.4	The forebulge issue, local Forsmark zones	22
3.2.5	Forebulge issue, large deformation zones	22
3.3	Model method verification	22
3.4	Rupture models	23
4	Continued work – results overview	25
4.1	General	25
4.2	Scope and objectives of this overview	26
4.2.1	Moment magnitude – rupture area	26
4.2.2	Induced fracture slip	26
4.2.3	Fault-fracture distances	29
4.3	Overview structure	29
4.4	Earthquakes occurring on small and medium-sized local DZ's	30
4.5	Earthquakes occurring on large DZ's	34
5	Critical radii at different fault-fracture distances	39
5.1	General	39
5.2	Earthquakes on ZFMA2	39
5.3	Earthquakes on large, gently dipping deformation zones	42
5.4	Earthquakes on large, steeply dipping deformation zones	44
5.5	Critical radii – steeply dipping fractures	47
6	Thermally induced earthquakes	49
7	Additional comments on conservatism and margins	51
7.1	Magnitude exaggeration and edge effects	51
7.2	Impact of fracture non-planarity	52
7.3	Target fracture propagation	52
7.4	Impact of fracture network	52
7.5	Impact of buffer-canister system	53
7.6	Model discretization	54
7.7	Elastic properties of the repository host rock	54
7.8	Target fracture pre-slip	54
8	Discussion and conclusions	55
8.1	General	55
8.2	Critical radii at different distances from deformation zones with trace lengths between 3 000 m and 5 000 m.	56

8.3	Critical radii at different distances from deformation zones with trace lengths larger than 5 000 m	56
8.3.1	Steeply dipping deformation zones	56
8.3.2	Gently dipping deformation zones	57
8.4	Concluding remarks	57
9	Remaining work	61
	References	63
Appendix A	Thermally induced earthquakes in Forsmark	69
Appendix B	Influence of a Discrete Fracture Network on Seismically Induced Fracture Shear Displacements	81

1 Introduction and background

1.1 General

Earthquakes have been recognised to potentially threaten long term safety since the early days of the Swedish nuclear waste programme (SKBf/KBS 1977, 1983). Using probabilistic arguments, these assessments concluded that “block movement” indeed could be induced by earthquakes also in cratonic bedrock, but also concluded that such movements would be very small, in the order of less than a mm over a million years, and with very low probability of occurrence. These conclusions were supported by the instrumental record of Scandinavian earthquakes and by findings that tunnels are very much more resistant to earthquakes than surface structures (e.g. Dowding and Rozen 1978). Altogether, therefore, the impact of earthquakes upon the repository performance was, then, regarded insignificant.

This view also prevailed in the following safety assessment, SKB 91 (SKB 1992), in which it was additionally concluded that, based on an analysis by Slunga (1990), “...*the aseismic movements i.e. movements that do not give rise to earthquakes – are probably of greater importance...*” (SKB 1992, p 40). It must be noted, however, that SKB 91 served as a basis for testing a system of efficient procedures for carrying out safety assessments, i.e. a test of methodology for safety assessments, using the Finnsjön site as a tentative location for the repository. Some limited modelling efforts (e.g. Barton and Chryssanthakis 1989) were performed to address the impact of glaciations upon fracture stability but these were not in any obvious way included in the safety assessment.

Although findings of large fault scarps indicative of large earthquakes in Scandinavia (example shown in Figure 1-1) were reported early (Du Rietz 1937, Kujansuu 1964), these records passed fairly unnoticed by the geoscientific community or were regarded upon with a certain degree of scepticism. However, in the late seventies, paleoseismology became an emerging, and accepted, branch of geosciences in Scandinavia, much triggered by the findings of exceptionally impressive fault scarps in Lapland (Lundqvist and Lagerbäck 1976, Mörner 1978, Henkel et al. 1983, Olesen 1985, Johnston 1987). The newly discovered scarps altered the prevailing view on seismicity in cratonic, formerly glaciated, regions. SKB did initiate a comprehensive research program to address the paleoseismic records in Sweden (e.g. Bäckblom and Stanfors 1989, Ericsson and Stanfors 1993, Stanfors and Ericsson 1993 and references therein) but an earthquake scenario, proper, was not introduced to safety assessments until SR97 (SKB 1999).



Figure 1-1. The Stenberget fault scarp displays about 6–7 m offset, which is indicative of an earthquake of magnitude 7–8. This, and many other similar observations, are compelling evidence that the Baltic shield is indeed seismically active, albeit with longer recurrence rates (Photo Raymond Munier 2012).

Using idealised geometries and conservative assumptions the seismic impact upon the canister integrity was addressed by La Pointe et al. (1997, 1999, 2002) in SR97 with the result that earthquakes were recognised to, indeed, impose a realistic threat to the canister integrity. Following the initial work of La Pointe et al. (1997), a number of efforts were initiated within the research programme (SKB 2001) to evaluate the conservativeness (La Pointe et al. 2000), to corroborate modelling results with tunnel observations (Bäckblom and Munier 2002, Bäckblom et al. 2004) and to identify alternative modelling concepts (Munier and Hökmark 2004). This emanated in an intensified research programme (SKB 2004) to develop adequate methods to compute the seismic impact, to populate the models with realistic data and to progress the results of these analyses to safety assessments. The development of the modelling methodology and the increasing wealth of modelling results are summarised in this report, and references herein.

This report, thus, aims at describing the numerical background material produced up to the present day to devise defensible protocols for a safe handling of the seismic risk for a KBS-3 repository at the Forsmark site. For the long term safety, it was early concluded that the only earthquake-related process that would constitute a risk for the integrity of the buffer-canister system would be shear displacements along fractures intersecting canister positions (Fälth et al. 2010). Liquefaction, for instance (i.e. a soil-water system behaves as a liquid because of shaking, stress increases or liquid pressure increases), was early ruled out as a problem because of the high density of the compacted bentonite buffer (Börgesson and Hernelind 2006). Other earthquake-related processes that potentially could constitute a risk for the integrity of the canisters, the bentonite buffer and the tunnel backfill material (shaking, rock failure in walls of tunnels and deposition holes, hydraulic disturbances) are discussed, commented and ruled out as realistic risks in Fälth et al. (2010) based on conclusions and observations made by, for instance, Muir-Wood and King (1993), La Pointe et al. (1997), Bäckblom and Munier (2002) and Aydan et al. (2010).

1.1 Problem statement

The review by Dowding and Rozen (1978) recognised that tunnels are far less vulnerable to earthquakes than surface constructions. This conclusion was again confirmed by an extensive review which included previously unpublished material (Bäckblom and Munier 2002). Unless located in soft sediments or rocks and close to the ground surface, damage in tunnels is essentially constrained to lining and other support, infrastructures such as piping and wiring and where stress can be concentrated such as intersection of tunnels, sharp bends, portals, etc. Should the earthquake generating fault intersect the tunnel, damage is constrained to within 100–200 m from its intersection with the tunnel (Munier and Hökmark 2004). If major deformation zones are avoided in the tunnel system, therefore, backfilled tunnels ought to be essentially immune to the negative impact of earthquakes. However, more important to the context of this report, large fractures or small deformation zones might be reactivated by nearby earthquakes due to static and dynamic stress redistribution that might render the structures in the repository volume unstable (Figure 1-2). In the terminology commonly used in seismology, this is called “distributed faulting”. In this report we call the reactivated structures “target fractures” as we perceive them of being subject to loads imposed from a distant source. We call the earthquake generating fault the “source” or “primary fault”, where appropriate.

Even if there are numerous reports on distributed faulting (or aftershocks) and their spatio-temporal relation to the primary event, there are a few, if any, records on the size and geometry of the target fractures, i.e. the fractures being reactivated by the fault. The properties of the target fractures is an extremely important factor as it enables SKB to, by repository design and underground characterisation, avoid structures amenable to host slip exceeding the canister failure criterion, 50 mm, which is based on numerical analyses of the canister and the buffer-canister system (SKB 2009a). Hence, as there is no empirical information available SKB has been resolved to address the issue by numerical modelling.

In short, the modelling consists of i) modelling the rupture on the primary fault and ii) modelling the target fracture response. These two aspects are briefly introduced in following chapters.

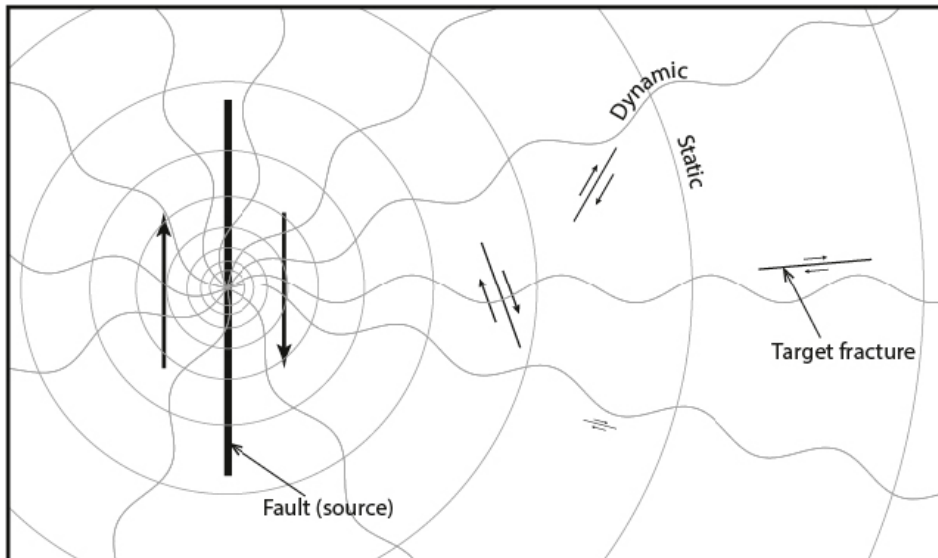


Figure 1-2. Schematic cartoon aiming to illustrate the static and dynamic impact on target fracture stability caused by a nearby earthquake.

1.1.1 Primary fault displacements

Figure 1-3a shows maximum fault displacements versus moment magnitude for crustal earthquakes as presented by Wells and Coppersmith (1994). Some of the large slip – low magnitude earthquakes are explicitly labelled. If a lower magnitude bound is tried as shown in the figure and extrapolated well outside the observation interval it would give around magnitude 4.0 for a 50 mm maximum primary fault displacement.

The blue plot symbols in Figure 1-3a correspond to low magnitude events for which no displacement data and no surface data are included in the Wells-Coppersmith catalogue. The maximum displacements plotted here for these events have been estimated using the catalogue values for the seismic moment M_0 (direct function of the moment magnitude M_w , and the rupture area RA , see Figure 1-3b, to calculate the average fault displacement D as (Hanks and Kanamori 1979):

$$D = \frac{M_0}{G \cdot RA}$$

assuming the rock shear modulus G to be 30 GPa. Finally, the maximum fault displacements have been assumed to be 1.75D. This ratio between maximum and average fault displacements is an uncertain quantity. In the Wells-Coppersmith database it varies in the range 1.2–5.

The focal depths of the four yellow-labelled events plotting below the suggested lower bound line in Figure 1-3a are 8 km, 7.5 km, 10 km and 10 km for the $RA=3 \text{ km}^2$, $RA=4 \text{ km}^2$, $RA=4 \text{ km}^2$ and $RA=5 \text{ km}^2$ events, respectively (Nábelek and Suárez 1983, Ohio Geological Survey 1986, Langer and Bollinger 1991). At these depths, large displacements can occur also on modest rupture areas assuming stress drops that are not even theoretically possible in the low stress region one or two kilometres below ground surface. For the 1983 Goodnow earthquake (yellow labelled 4 km^2 RA in Figure 1-3a), for instance, Nábelek and Suárez (1983) estimated the stress drop to be 26.5 MPa. In the low stress region one or two kilometres below ground surface an earthquake of similar magnitude would have a significantly lower stress drop, a larger rupture area and a smaller average and maximum displacement, i.e. it would plot to the left of the lower bound line suggested in Figure 1-3a. At repository depth in Forsmark, for instance, the maximum shear stress is around 15 MPa for the “Most Likely Stress Model” and about 22 MPa for the “Maximum Stress Model” (SKB 2009b). Given that the stress drop typically is one order of magnitude smaller than the total stress (Scholz 2002), it appears that events plotting in Figure 1-3 as for, instance, the 1983 Goodnow earthquake are not realistic at repository depth in Forsmark where stress drops would not amount to more than a few MPa.

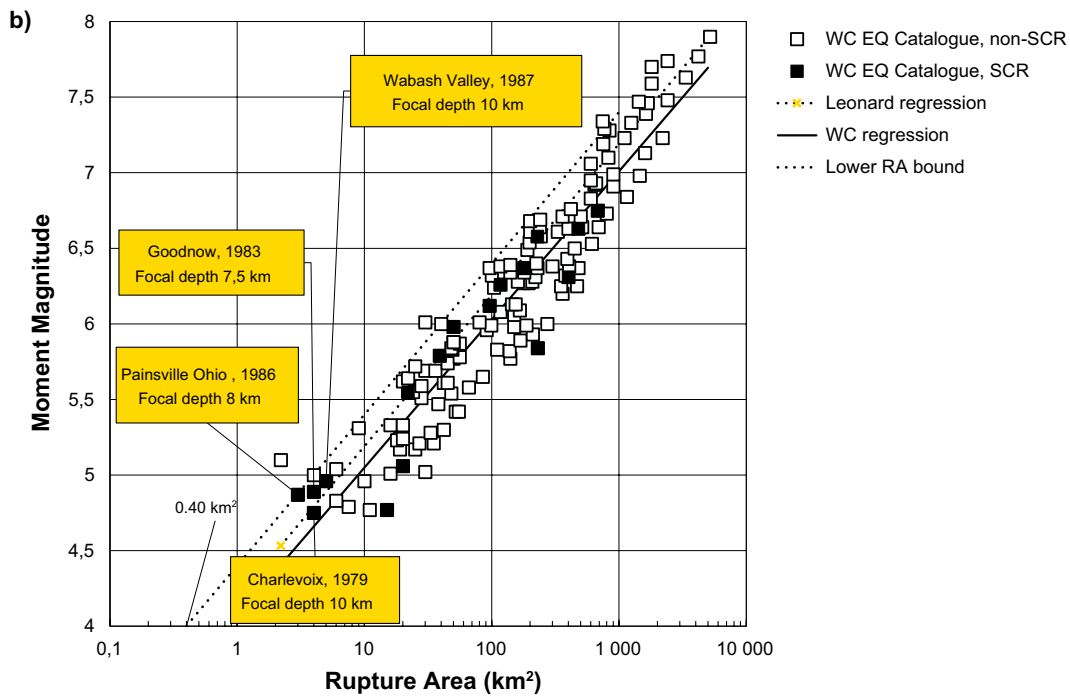
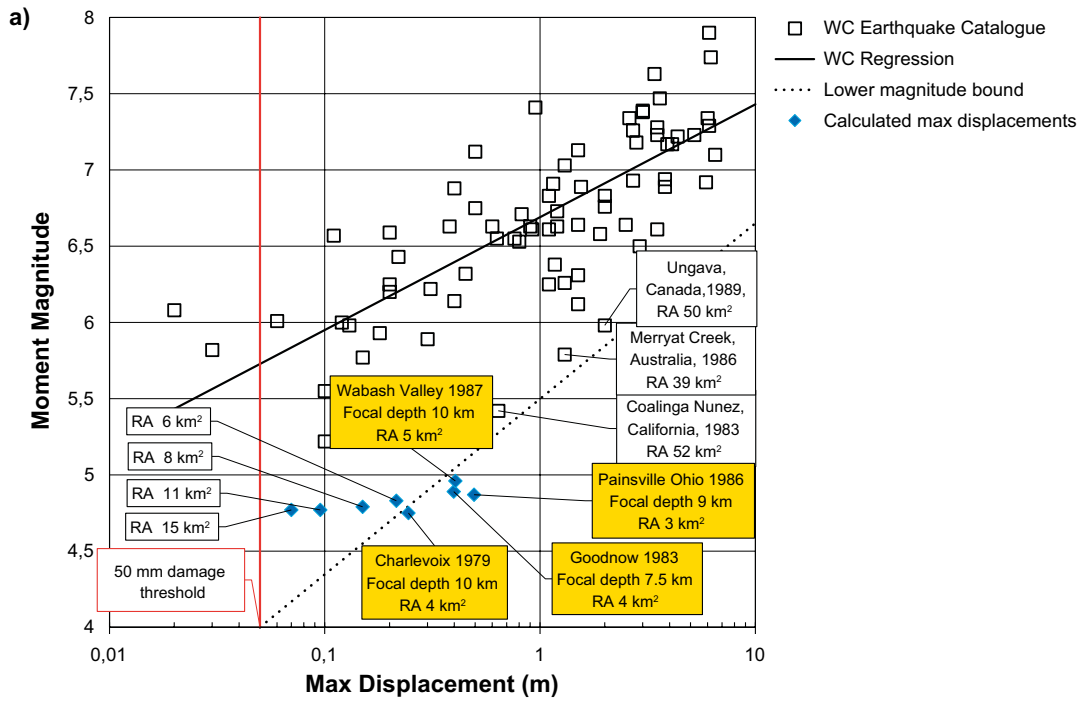


Figure 1-3. a) Moment magnitude versus maximum displacement. Data and regression are from Wells and Coppersmith (1994) while the approximate lower magnitude bound has been added here for this study. Blue plot symbols, also added here for this study, denote low magnitude, deep-seated, Wells-Coppersmith (WC) events for which no displacement data are included in the WC catalogue. See associated text for additional information on these events in general and on those with coloured legends in particular. b) Moment magnitude versus rupture area. SCR (see legend) means Stable Continental Region earthquakes. Data and regressions are from Wells and Coppersmith (1994) and Leonard (2010). The approximate lower RA bound has been added here for this study.

To conclude: for earthquakes occurring at shallow depths, e.g. at about repository depth, there are good reasons to trust the lower bound line also outside the observation interval and to establish M_w 4.0 as the lowest moment magnitude required for a maximum slip of 50 mm.

Figure 1-3b shows moment magnitude vs rupture area for earthquakes in the Wells and Coppersmith (1994) catalogue along with regressions established by Wells and Coppersmith (1994) and Leonard (2010). Moment magnitudes are in the range 4.75-7.9. A lower rupture area bound line is added and extrapolated to magnitude 4.0. Note that the lower RA bound is drawn well to the left of all Stable Continental Region (SCR) earthquakes (and that focal depths of SCR earthquakes occurring on small rupture areas typically are larger than about 7 km). Trusting the bound and the extrapolation it appears that 0.40 km^2 would be a safe lower bound estimate of the rupture area required for a moment magnitude 4.0 earthquake, i.e. for an earthquake with a maximum slip of 50 mm (occurring at depths of a few km, cf. discussion above on the lower magnitude bound in Figure 1-3a).

For completeness it should be mentioned that the lower rupture area bound for an earthquake with a maximum fault slip of 50 mm was suggested to be 2 km^2 in the SR-Site background material (Fälth et al. 2010). The 0.4 km^2 lower bound suggested here is the result of an even more conservative handling of the datapoints in Figure 1-3a (i.e. the issue of uncertain extrapolation).

Accordingly, even if the extrapolations are uncertain processes, both bounds (lower magnitude bound in Figure 1-3a and lower RA bound in Figure 1-3b) may be concluded to be sufficiently distanced from the catalogue outliers for the 0.40 km^2 area to be a relevant lower bound estimate of the fault size required for 50 mm slip at one or two kilometres depth below ground surface. It should finally be noted that the bound suggested in Figure 1-3b regards rupture areas, not fault areas, meaning that there is an additional built-in, but uncertain, fault size margin. For instance, if it is assumed that 50 % of the fault area ruptures, then the lower bound fault area would be 0.8 km^2 . Using correlations between surface rupture and fault length presented by Slemmons and Chung (1982), roughly 30 % of the fault surface is involved in the rupture which corresponds to a fault area of 1.3 km^2 .

1.1.2 Secondary displacements

As outlined in the previous section it would be easy to ensure, with very good margins, that no canisters will be located in positions intersected by faults or fractures large enough to host earthquakes with slip movements of 50 mm or more. The 0.4 km^2 lower rupture area estimate corresponds approximately to a 700 m diameter fracture or fault, provided that the entire fault surface ruptures, which is unlikely, and about 1 km if 50 % of the fault area ruptures.

There is, however, the theoretical possibility that also modestly sized fractures could slip in response to dynamic and quasi static stress effects of an earthquake occurring on a nearby or distant fault. Since such secondary, seismically induced, fracture shear displacements would be powered and controlled by complicated combinations of stress wave effects and stress redistribution effects rather than by the type of stresses powering the seismic events considered by Wells and Coppersmith (1994), there is no way of using the empirical data shown in Figure 1-3 to obtain lower area bounds to fractures that potentially could slip by 50 mm or more in response to a nearby earthquake. Since there does not seem, at the present time, to exist any systematic compilation of empirical data relevant to this issue, estimates of secondary off-fault fracture displacements for different types of earthquakes will have to be based on results of numerical simulations.

In this overview, the results of the many attempts made, both in the past with very schematic input assumptions and more recently with input assumptions based on Forsmark and Olkiluoto site data, to set bounds to seismically induced secondary displacements are compiled.

2 Secondary displacements – numerical assessment

2.1 Early work

Over the years several studies, with levels of complexity and realism following the steadily increasing computational capacity, have been carried out to make estimates of secondary fracture shear displacements. La Pointe et al. (1997, 1999, 2000) used the Poly3D code (Thomas 1993) to explore the static effects of schematically modelled earthquakes on discrete fracture network (DFN) populations of zero shear strength fractures in an initially stress-free, perfectly elastic, medium. The results of the static Poly3D calculations (La Pointe et al. 1997) were used as part of the input to SKBs first attempt to handle the earthquake scenario in the SR-97 assessment of the long term safety of a KBS-3 repository (SKB 1999). Dynamic aspects were first addressed by Baker et al. (2004b) using the Wave code (Hildyard et al. 1995) to simulate a rupturing fault. Then, Christianson (2004) and Baker et al. (2004a) used the output of the Wave code to specify dynamic boundary conditions for a box-shaped FLAC3D (Itasca 1997) model containing one single target fracture. In following development steps, additional Wave models as well as FLAC3D models in which the earthquake fault (the “primary fault”) and one single target fracture were both explicitly modelled, have been analysed (Munier and Hökmark 2004).

2.2 SR-Can and SR-Site

Neither the Wave code nor the FLAC3D code were judged to be tools fully suitable for analysing general problems with arbitrarily sized, shaped and oriented earthquake zones (“primary faults”) and with numerous, arbitrarily sized and oriented off-fault host rock fractures (“target fractures”) responding to both dynamic and quasi-static stress effects. For the continued work with seismically induced fracture shear displacements related to the assessment of the risk for the KBS-3 repository, the well-established rock mechanics code 3DEC (Itasca 2013) has been used. 3DEC (3-Dimensional Distinct Element Code) is a simulation tool based on the distinct element method (Cundall 1971). 3DEC simulates the response of discontinuous media subjected to static or dynamic loads using an explicit time-stepping solution scheme. Joint planes (boundary between blocks in Itasca terminology) can be kept active to model an assemblage of blocks or glued together to simulate a continuum. Blocks may behave either as rigid or deformable material. Deformable blocks are discretized using finite-difference elements, while forces and relative movements along their boundaries are controlled by so-called subcontacts. For dynamic problems, different damping schemes are available, and boundaries can be designed to suppress irrelevant wave reflections. 3DEC has a built-in programming language, FISH, which enables the user to define new variables and functions. When modelling earthquakes, FISH can be used to control in detail, for instance, the style of rupture initiation and propagation. For the safety assessment SR-Can Fälth and Hökmark (2006a) used 3DEC to calculate secondary displacements induced by the combined dynamic and static stress effects of Magnitude 6 earthquakes occurring on a nearby fault zone in models with generic stress-fields. For the most recent safety assessment SR-Site (SKB 2011), Fälth et al. (2010), again using the 3DEC code, calculated secondary displacements induced by differently sized earthquakes. The 3DEC models in Fälth and Hökmark (2006a) and in Fälth et al. (2010) were all based on generic assumptions regarding the stress-field and the strength properties of the earthquake fault. The rupture was initiated at a predefined hypocentre and programmed to propagate at a predefined velocity until the entire fault had ruptured. The strength breakdown at the rupture front was accomplished by down-ramping of the shear strength over a specified reduction time interval. The stress field was deliberately set to give earthquakes of magnitudes well above typical magnitudes of crustal earthquakes occurring on similarly sized faults, assuming the rupture to result in a total loss of the fault shear strength. The numerical modelling results reported by Fälth et al. (2010) were used to determine critical fracture radii at different distances from differently sized deformation zones, i.e. the radii of the smallest fracture (target fracture) that could slip by 50 mm in response to an earthquake occurring on that zone. Figure 2-1 shows the outlines of the type of models analysed by Fälth et al. (2010). The model includes both the rupturing fault and a number of 300 m diameter target fractures. Because of the symmetry plane (necessary to keep the model within computationally affordable size at the time) the rupturing fault could, in that particular suite of models, not be arbitrarily oriented relative to the initial stress field.

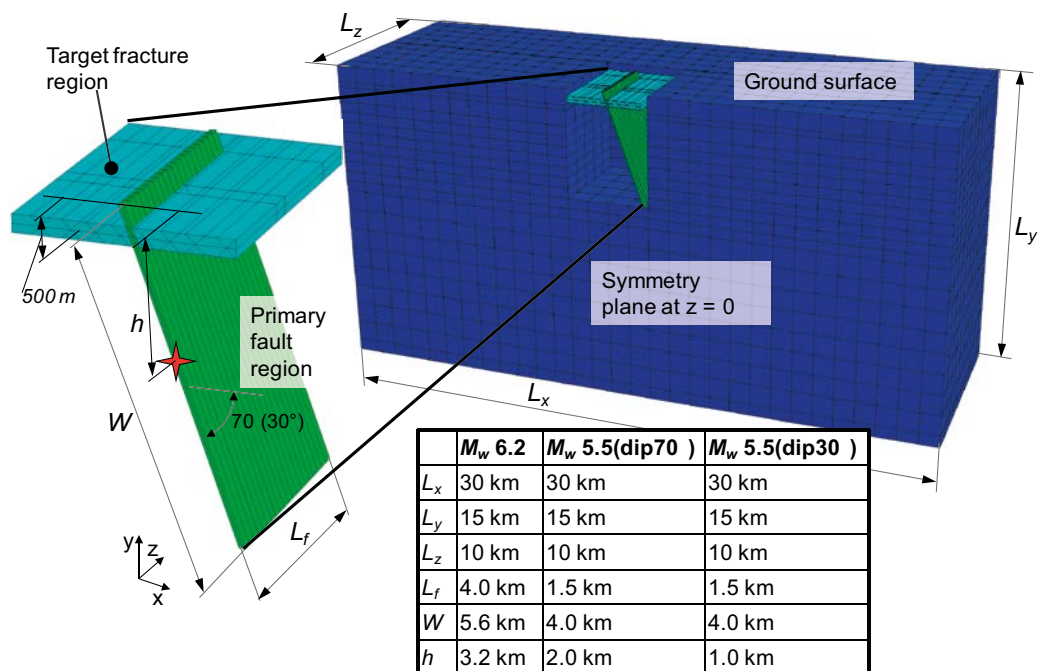


Figure 2-1. Example of 3DEC model outline. From Fälth et al. (2010).

2.3 SR-Site critical radii and respect distances

Figure 2-2 shows some of the results reported by Fälth et al. (2010) used to establish critical radii for the handling of the seismic risk in SR-Site. The “critical radius” is the radius of a fracture that potentially could slip by 50 mm and “critical fractures” are fractures with radii \geq the critical radius (SKB 2010), i.e. fractures that must be avoided when deciding on canister positions.

The upper diagrams in Figure 2-2 show actual calculation results in terms of cumulative graphs, the lower row shows idealized cumulative graphs based on the actual results. Note that results obtained from model versions where the maximum fault slip velocity exceeded 100 % of the maximum fault slip reported for the magnitude 7.6 Chi-Chi 1999, Taiwan, earthquake have been disregarded as unrealistic. The Chi-Chi earthquake is specifically reputed for its high slip velocities (Ma et al. 2003). It should be noted that the maximum Chi-Chi slip velocity (4.5 m/s) was found only on a small near surface portion of the rupturing Chelungpu Fault, whereas the even higher velocities in the disregarded 3DEC models were found along substantial fault trace fractions. The exact reasons for the high slip velocities found in the three disregarded magnitude 7.5 models are difficult to determine: Combinations of exaggerated stress drops, complicated effects of questionable symmetry planes (necessary at the time of these simulations because of the limited processor capacity), details of the rupture protocol etc.

Although it is not within the scope of this report to defend or justify the use of fault slip velocity as a discriminating factor, it should also be mentioned that none of the models with reasonably realistic primary faults planes analysed after the appearance of the SR-Site background material (i.e. Fälth et al. 2010) has produced secondary displacements that are even close to 60 mm on 300 m diameter target fractures (see following chapters of this report). This verifies that the results interpretation (Figure 2-2, lower right) should hold as a basis for safe upper bound estimates. However, since it has appeared to be difficult to ensure that slip velocities obtained in numerical models and velocities estimated from field observations are based on comparable time (and area) averages, the slip velocity has not been used in the continued work to judge on the relevance of any 3DEC models.

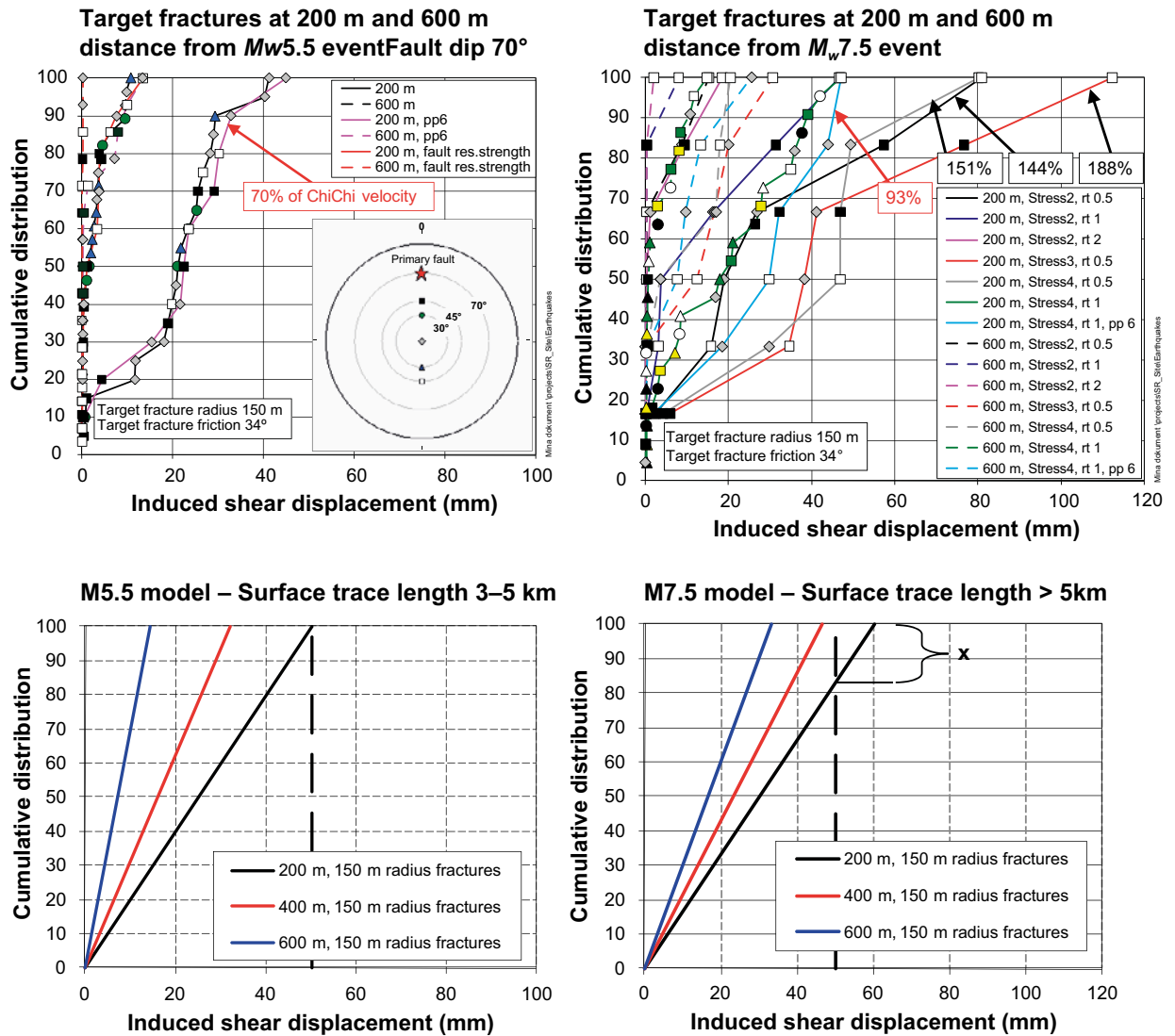


Figure 2-2. Upper: Cumulative graphs of numerical fracture slip results reported by Fälth et al. (2010). Lower: Cumulative graphs simplified for use as input in layout decisions. The 400 m results are interpolations between the 200 m and the 600 m results. The lower row graphs are based on slip results for gently dipping fractures (dip between 0 and 55 degrees). For steeply dipping fractures, the calculated slip is typically more than 25% smaller. “x” denotes the fraction of 300 diameter gently dipping fractures that would slip by more than 50 mm. The percentages given in the upper right regard the max fault slip velocity in relation to the max slip velocity of the Chi-Chi 1999, Taiwan, earthquake, see Fälth et al. (2010) for details on this issue. Only results from models with max fault slip velocities < 100% of the max Chi-Chi fault slip velocity have been taken into account when establishing the schematic cumulative distributions shown in the bottom row. Graphs from Fälth et al. (2010).

The results in Figure 2-2 regard gently dipping fractures. Due to the reverse faulting stress regime assumed in all models analysed and reported in Fälth et al. (2010), steeply dipping fractures were significantly more stable initially and consequently less prone to slip in response to the seismic disturbances. For steeply dipping fractures, idealized cumulative plots corresponding to those shown in Figure 2-2 (lower), but with 25 % smaller secondary slip at all distances, were concluded to be both relevant and conservative. For details on this issue, see Fälth et al. (2010). This difference between slip on steeply dipping and gently dipping fractures has been shown to hold within good margins also in the Forsmark and Olkiluoto model work performed after SR-Site, see discussion in Fälth et al. (2015) and text associated with Figure 4-2 in the following chapter. The systematic difference found between slip on steeply dipping and gently dipping fractures is a logical consequence of the differences

in the initial fracture stability for differently oriented fractures in highly anisotropic stress fields, such as the reverse faulting stress fields at repository depth in Forsmark and Olkiluoto. During the period of particular concern, i.e. the time of ice retreat after a glaciation, gently dipping fractures will be further destabilized, and steeply dipping fractures stabilized. The dip range of transition from stabilization to destabilization depends on the details of the in-situ stress field and the details of the glacial stress evolution. In an Olkiluoto study (Hökmark and Fälth 2014), the transition dip range at repository depth was found to be 65–70 degrees for all combinations of stress models and ice models giving more than insignificant stability effects, see Figures 4-13 through 4-18 in Hökmark and Fälth (2014).

Figure 2-3 shows the idealized results in Figure 2-2 (lower) translated to critical radii at different distances from differently sized faults. These schematic layout sketches do also illustrate the respect distance concept and the associated layout rules applied for the Forsmark repository in SR-Site:

- No canisters should be positioned within 100 m from deformation zone boundaries.
- The critical radius at distances between 100 m and 200 m from the deformation zone boundaries is 50 % of the critical radius for the 200 m distance.

The critical radii shown for the different distance ranges are those calculated for the range limit closest to the fault. It should be noted that the many different values of critical radii shown in Figure 2-3 are determined assuming that fracture slip scales with fracture radius. This, which is strictly true for planar, circular fractures subjected to uniform quasi-static load changes (cf. Eshelby 1957), has been shown to hold also for corresponding fractures under the type of dynamic loads typically generated by the synthetic 3DEC earthquakes (Fälth et al. 2010). For completeness it should be mentioned that, considering the frequencies of importance to secondary slip (order of 1 Hz, see for instances (Fälth and Hökmark 2015), and the difference in stress effects at different distances from the rupturing fault plane, the scaling should not be expected to hold for km-sized fractures. For fractures with diameters of few hundred meters the scaling can, as demonstrated by Fälth et al. (2010), be regarded as a good enough approximation.

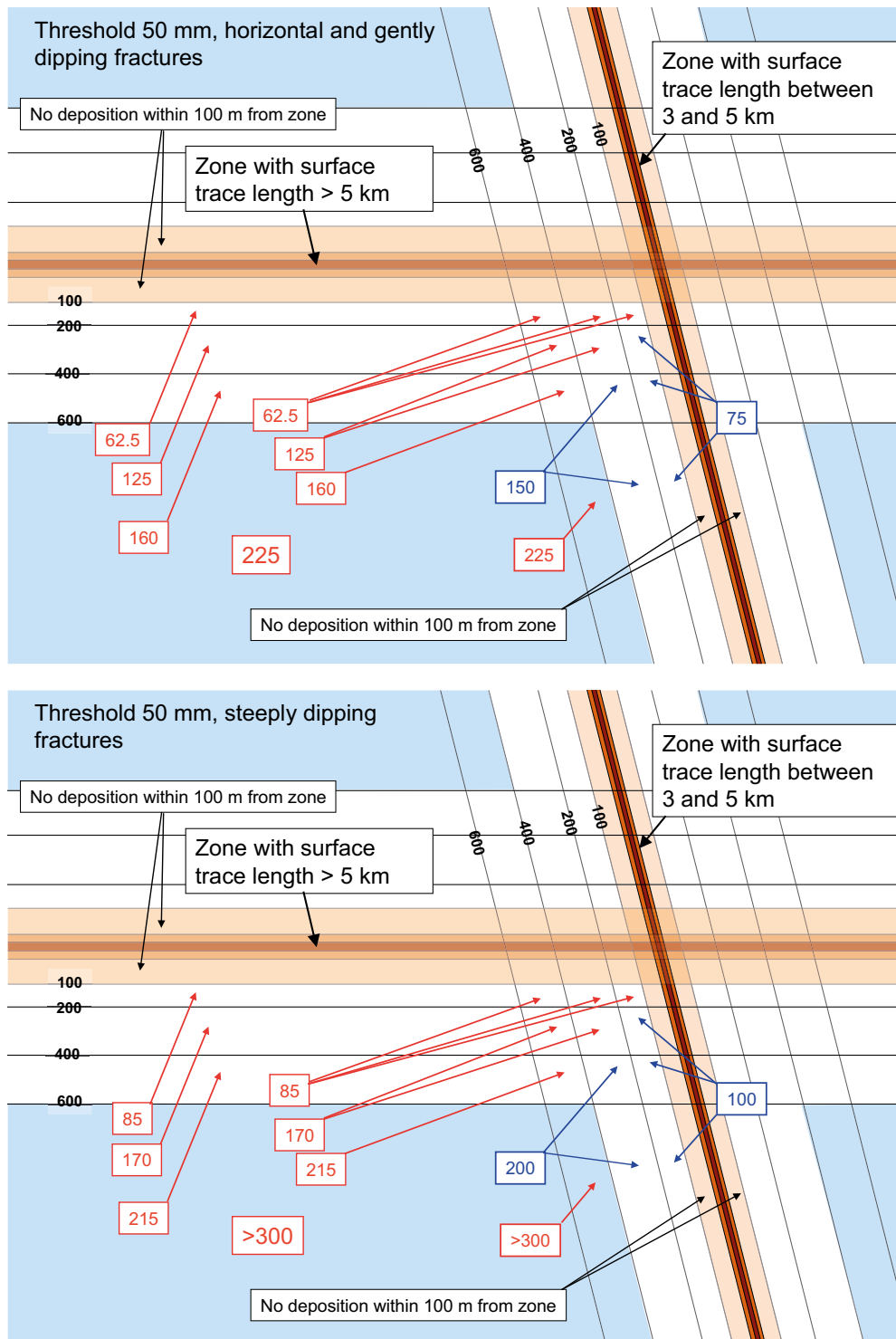


Figure 2-3. Critical radii at different distances from differently sized faults. Upper: gently dipping target fractures. Lower: steeply dipping target fractures. Blue legends regard critical radii determined by distance to small deformation zone. From Fäth et al. (2010).

3 Continued work

3.1 General

The 3DEC models analysed by Fälth and Hökmark (2006a) and Fälth et al. (2010) for the SR-Can and SR-Site safety analyses, briefly summarized in the previous chapter, were based on generic geometries, properties and stress fields. All target fracture slip results were, for conservativeness, obtained from models with input assumptions designed for secondary slip overestimates, e.g.:

- Rupture of the entire fault area
- Complete loss of shear strength at the rupture front
- Significantly exaggerated magnitudes given the rupture areas
- Perfectly planar target fractures

However, at the time of these analyses, the computational resources did not allow for numerous analyses of large and finely discretized models with numerous, differently oriented, target fractures. Additionally, the use of symmetry planes, necessary for computational purposes (cf. Figure 2-1), meant that deformation zones could not be arbitrarily oriented, e.g. according to site models. In conclusion: even if the results in Fälth et al. (2010) concerning target fracture slips appear to be upper bounds with margins sufficient for the idealized cumulative graphs in Figure 2-2 and the associated critical radii estimates shown in Figure 2-3 to be a relevant and safe input to the assessment of the long term seismic risk at Forsmark, development of the modelling method and continued work with site-specific models has been judged to be necessary. In this chapter some of the site-specific issues addressed in the continued work, i.e. the modelling work on seismically induced slip on host rock fractures performed after finalising the SR-Site background material, are commented. The models and the results are presented and overviewed in the following chapter.

It should also be mentioned here that the continued work includes models with different degrees of coupling to site data:

- For models of earthquakes on local, modestly sized and reasonably well characterized deformation zones, site data are, with minor simplifications, used according to the site model at hand at the time of modelling.
- For models of earthquakes occurring on large deformation zones, more or less hypothetical assumptions of the actual fault sizes are made to account for fault width and length uncertainties. For large deformation zone models the stress field at depths below a few kilometres has systematically been set to maximize the fault instability, i.e. strike-slip stress regimes are assumed for models involving steeply dipping deformation zones and reverse faulting stress regimes for models involving gently dipping zones.

All simulations of earthquakes on large deformation zones have been performed within the Posiva simulation program set up for the Olkiluoto site. Considering the hypothetical, worst case, approach typically taken regarding fault sizes and stress fields, the results of these models are judged to be as relevant for the Forsmark site as for the Olkiluoto site. This approach is justified also by the reasonably similar Forsmark and Olkiluoto stress fields at repository depth and the almost identical Forsmark and Olkiluoto glacial stress evolutions (Lund et al. 2009, Lund and Schmidt 2011).

3.2 Comments on stress and stability

3.2.1 General

As opposed to the models analysed by (Fälth et al. 2010), i.e. the SR-Site background material, the continued work on Forsmark models described in the following chapters is based on site-specific present-day stresses with (when required) glacially induced stress contributions.

3.2.2 Glacially induced stresses

Figure 3-1 shows the glacial stress evolution assumed for the Forsmark site. These glacial stresses are obtained by Lund et al. (2009) from ice/crust/mantle analyses performed using the UMISM reconstruction of the Weichselian glaciation. Since large end-glacial earthquakes are known to have occurred (at least in parts of the Baltic shield) in connection with the latest, Weichselian glaciation, the main focus in the simulations overviewed in following chapters is on the time of ice retreat (“ice margin passing”), i.e. when substantial fractions of the glacially induced horizontal stresses remain (≈ 10 MPa) while the stabilising vertical ice load has been lost. As seen in Figure 3-1 there is also some stability loss related to the reduced compression of steeply dipping deformation zones at the time of the forebulge

3.2.3 In-situ stress model and local Forsmark fault stability evolution

Figure 3-2 (left) shows the in-situ stress model assumed in the continued 3DEC work (full lines). At 500 m depth the 3DEC stress model agrees with the “most likely” Forsmark stress model (dashed lines), suggested to be valid down to at least one km depth (Martin 2007). At depths below about 2.5 km the 3DEC model stress regime changes from reverse to strike-slip. This (reverse stress regime at shallow depths and strike slip-regime below a few kilometres depth) is in qualitative agreement with measurements made in the Siljan region (Lund and Zoback 1999) and earthquake source mechanisms in the Baltic Shield analysed by Slunga (1991). The notion of a reverse stress regime down to at least 1 km depth is also in agreement with conclusions made by Stephansson et al. (1991) regarding stresses in the Fennoscandian shield.

Comparing the “most likely model” horizontal stress anisotropy with the corresponding 3DEC model stress anisotropy at 1000 m depth, it appears that the “3DEC stress model”, i.e. the stress model assumed in all Forsmark models analysed within the continued work described in following sections of this overview, overestimates the horizontal stress anisotropy considerably. If the “most likely” Forsmark stress model is extrapolated to a few kilometres depth (dotted lines) the horizontal stress anisotropy would practically disappear making all steeply dipping local deformation zones extremely stable.

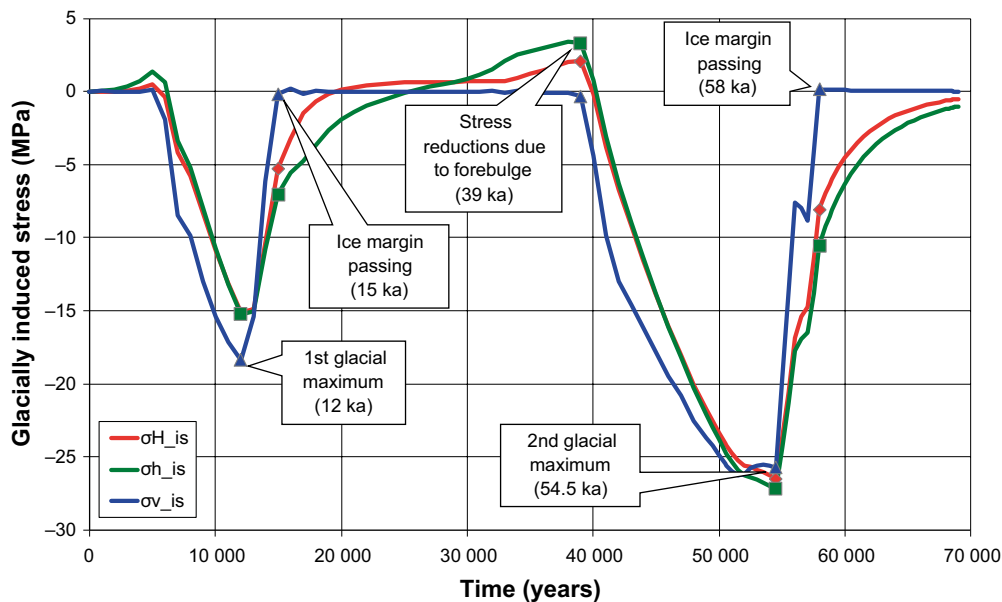


Figure 3-1. Glacially induced stresses as calculated by Lund et al. (2009). From Hökmark et al. (2010).

Figure 3-2 (right) shows (assuming the “3DEC stress model” to apply) the stability of all local Forsmark deformation zones with surface trace lengths > 3km at three different depths under present-day, end-glacial and forebulge stress conditions. The stability is given in terms of the *CFS* (Coulomb Failure Stress) quantity:

$$CFS = \tau - \mu(\sigma_n - P) - c.$$

Here τ and σ_n are the shear- and normal stresses acting on the fault plane while μ , P and c is the coefficient of friction, the pore pressure and the cohesion, respectively. Positive *CFS* values mean instability. The coefficient of friction is set at 0.65, the pore pressure is assumed to be hydrostatic (for present-day and forebulge conditions) and the cohesion is set at zero. For end-glacial conditions, excess pore pressures of 1, 2 and 3 MPa, respectively, are assumed for the three different depths in order to account, at least approximately, for potential effects of liquid pressures remaining behind the retreating ice margin (cf. Lönnqvist and Hökmark 2015a).

The ZFMA2 deformation zone has a dip angle of about 20 degrees while the others dip by between 85 and 90 degrees. The surface trace lengths of the steeply dipping zones are, from left to right, 7.9, 5.1, 3.1, 3.3, 3.1 and 3.5 km, respectively. Looking at catalogue data (e.g. Coppersmith et al. 2009) it appears that the fault width typically is significantly smaller than the fault length, i.e. earthquakes occurring on any of the steeply dipping faults would not involve fault segments much deeper than about 3 km.

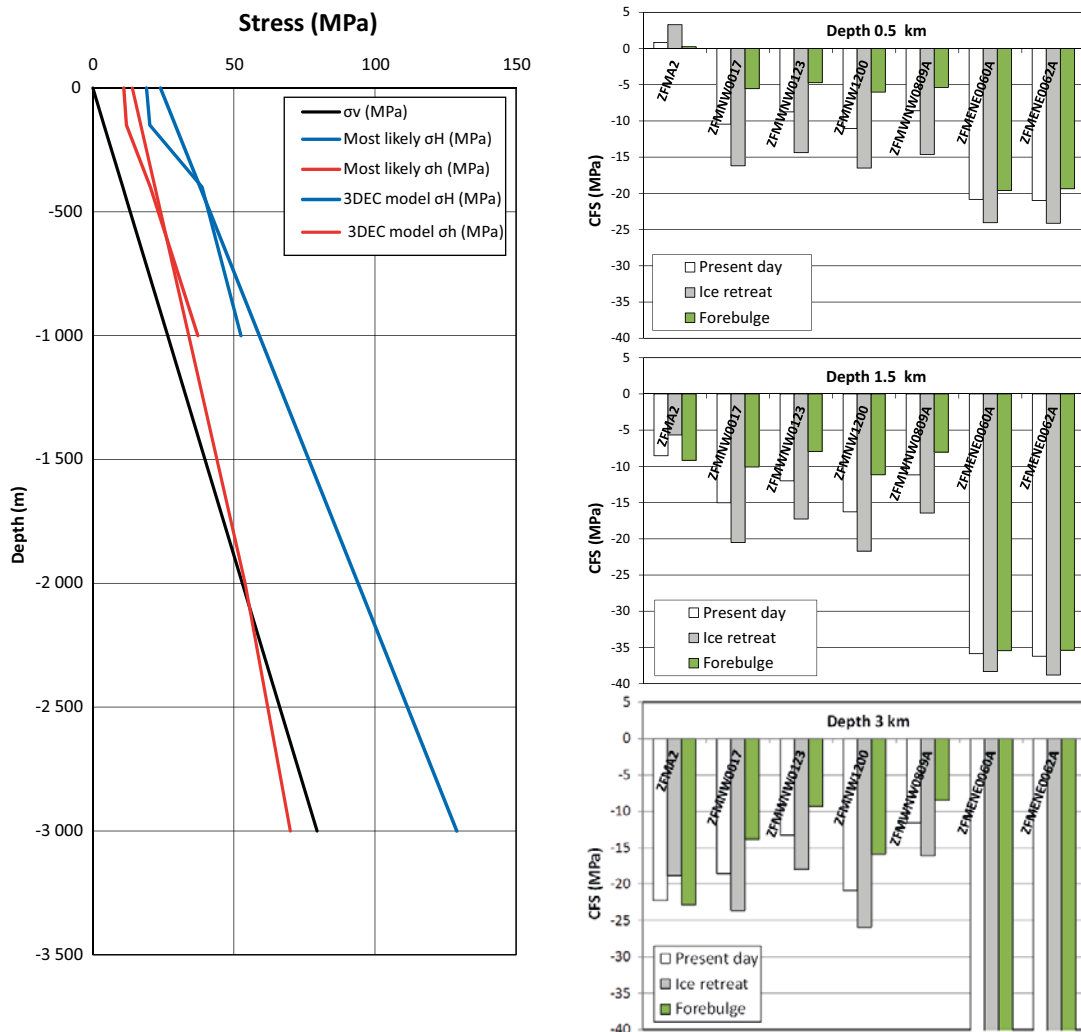


Figure 3-2. Left: Most likely Forsmark stress model (dashed lines) and the 3DEC in-situ stress model used in the continued work on earthquakes occurring on Forsmark deformation zones. Right: *CFS* stability (based on the 3DEC stress model) of all local Forsmark zones with trace lengths > 3m. Dip angles are from left to right: 20, 85, 83, 85, 90, 85 and 85 degrees.

Regardless of the many uncertainties concerning the stress conditions and the actual maximum depth of the local Forsmark deformation zones it seems clear that the zone that, with good margins, has the lowest initial stability at depths down to 1.5–2 km is the gently dipping ZFMA2 zone. It is also the only zone that loses stability during the time of ice retreat, i.e. the time period during which seismicity in parts of the Baltic shield potentially could be significant. At depths down to 1.5–2 km, all steeply dipping zones are significantly more stable than the ZFMA2 zone under present-day conditions and are even further stabilized under end-glacial conditions. For the main local scenario, i.e. that a present-day or end-glacial earthquake would occur on any of the local Forsmark deformation zones, only the ZFMA2 zone has been considered in the continued work summarized in the following chapter. This does also imply that, as far as end-glacial and present-day earthquakes are concerned, the only local Forsmark deformation zone that would require any respect distance (Munier and Hökmark 2004, Munier et al. 2008) would be the ZFMA2 zone.

3.2.4 The forebulge issue, local Forsmark zones

As seen in Figure 3-2 (right) all steeply dipping local Forsmark zones lose, in agreement with the glacial stress evolution pictured in Figure 3-1, stability under forebulge stress conditions. This raises (even if the forebulge stability of these zones is larger at all depths than the end-glacial and present-day stability of the ZFMA2 zone at depths down to about 1.5 km) the question of whether or not earthquakes large enough to induce significant secondary displacements on repository host rock fractures could occur during the forebulge period of a future glaciation. It should be noted that the stability of the local steeply dipping zones under present-day and forebulge conditions (based on the “3DEC stress model”) shown in these graphs is considerably underestimated at depths below about 500 m compared to the stability that would result from the modest horizontal stress anisotropy associated with the “most likely stress model”, Figure 3-2 (left)

Preliminary calculations indicate that the largest steeply dipping fault (ZFMNW0017) will not slip at all under forebulge stress conditions, even for rupture protocols that, when applied to the ZFMA2 deformation under end-glacial conditions, generate fault slip as well as moment magnitudes well in excess of the outliers in the Wells-Coppersmith diagrams shown in Figure 1-3 (cf. e.g. “ZFMA2, Base Case” and “ZFMA2 Inc Res” results in Figure 4-4 and Figure 4-6 in the following chapter).

It remains to check whether or not any of the local zones with the lowest forebulge stability, e.g. the ZFMWNW123 zone, would slip sufficiently to induce more than insignificant secondary host rock fracture displacements when modelled as the ZFMNW0017 zone.

A strategy for a credible and safe assessment of the risk of large secondary host rock fracture displacements caused by forebulge earthquakes on any of the local, steeply dipping Forsmark deformation zones is suggested and discussed in the concluding chapter of this overview.

3.2.5 Forebulge issue, large deformation zones

For large, steeply dipping, deformation zones, reaching depths with very uncertain stress conditions, forebulge earthquakes is a theoretical possibility. The continued work overviewed in the following chapter includes simulations of forebulge earthquakes on large Olkiluoto deformation zones. Because of the hypothetical and exaggerated assumptions made regarding the extension (zone length and zone width) and the stresses in these Olkiluoto models, the model results are judged to be as relevant for Forsmark as for Olkiluoto.

3.3 Model method verification

In a study addressing the suitability of the 3DEC code for the type of analyses performed within the scope of the SKB safety assessment, the code was benchmarked for waveforms and for propagation of waves generated on 3DEC joint planes located within the model volume (Fälth et al. 2015). A first attempt to apply the method in a site-specific Forsmark model was also made by Fälth et al. (2015). One of the benchmark models was later on used by Fälth and Hökmark (2015) for a check of the frequencies (and the associated requirements on model discretization) relevant for the process of seismically induced slip on target fractures.

3.4 Rupture models

The dynamic simulations reported in the SR-Site background material were all based on a time-weakening rupture model, with a rupture programmed to propagate from a predefined hypocentre at a constant predefined velocity and with a predefined time specified to accomplish the strength breakdown at the rupture front. This rupture model has also been applied in the majority of the simulations performed within the continued work considered in this overview, including all Forsmark models. For the site-specific models analysed within the continued work, however, a small residual fault strength has, in contrast to the generic SR-Site work, been assumed for the rupturing fault in order to suppress irrelevant post-rupture fault oscillations. In one of the Olkiluoto studies (Fälth et al. 2019) a more developed rupture mechanism (the “slip-weakening model” as opposed to the “time-weakening model”) allowing for spontaneous propagation of the rupture was adopted. As far as the impact on the resulting induced slip on surrounding host rock fractures is concerned, the differences between results obtained from model based on the “time-weakening” and the “slip-weakening” rupture models do not differ much. In the results overview in the following chapter, details on rupture protocols and parameter values are not included or commented.

One issue related to the implementation of the “time-weakening model” has turned out to be that of a shear stress peak that potentially could grow without limits ahead of the travelling rupture front at long hypocentre distances (if no measures are taken to handle this). In the Forsmark “Alt Hypo Case” described in following sections this may have contributed to exaggerated off-fault effects (Fälth et al. 2016).

4 Continued work – results overview

4.1 General

Over the last five to six years, a large number of dynamic simulations of earthquakes, assumed to occur on differently sized and oriented Olkiluoto and Forsmark deformation zones, have been performed and reported. All simulations are, as in the SR-Site work, performed using the 3DEC code, see Section 2.2.

In some of the simulations, deterministic deformation zones were modelled with width along the dip direction and length along the strike direction set according to estimates made in the Olkiluoto or Forsmark site description versions at hand at the time of the modelling work. In other cases, earthquakes were simulated on large hypothetical fault planes in order to explore the potential impact of large earthquakes occurring on undetected faults or faults that are detected and categorized but could turn out to be of much larger extension in reality. Up to the present day, such large hypothetical earthquakes have been modelled only for the Olkiluoto site. Most of the general conclusions of these analyses would, however, be valid also for corresponding earthquakes occurring on large, similarly sized and oriented, hypothetical deformation zones at the Forsmark site.

All 3DEC synthetic Olkiluoto and Forsmark earthquakes modelled up to the present day within the Posiva and SKB programs to address the seismic risk for the Olkiluoto and Forsmark repositories are listed below. Early similar work (Fälth and Hökmark 2006a, Fälth et al. 2010) on generic models without coupling to any specific site or to any specific load scenario are not further discussed within this overview.

Olkiluoto

- End-glacial earthquakes on deformation zones BFZ021, BFZ100 and BFZ214 (Fälth and Hökmark 2011). Deformation zones sized and oriented approximately according to site description.
- End-glacial earthquakes on deformation zones BFZ021, BFZ039 and BFZ100 (Fälth and Hökmark 2012). Deformation zones sized and oriented approximately according to site description.
- Present-day earthquakes on hypothetically extended version of BFZ214 (Fälth and Hökmark 2015).
- Forebulge earthquakes on hypothetically extended version of BFZ214 (Fälth et al. 2019).
- Present-day, thermally-induced and end-glacial earthquakes occurring on a system of connected, deformation zones consisting of the gently dipping BFZ020, BFZ021 and BFZ099 zones. All these deformation zones intersect the repository footprint and belong to the Olkiluoto zones that, given the in-situ stress conditions and the expected stress evolution during future glaciations, appear as suggested by Hökmark and Fälth (2014), to be the ones that could constitute a reasonably realistic seismic risk for the Olkiluoto repository. For this system of deformation zones, a number of different models are analysed, including models with fault geometries and areas based on site description best estimates and models with different, hypothetical, degrees of fault size exaggeration. Also different assumptions of hypocentre location, style of fault interaction, fault plane property distributions and rupture propagation were tested (Fälth et al. 2019).

Note that none of the result obtained in the first Olkiluoto study (Fälth and Hökmark 2011) are included in the following results compilation. That study is listed here for completeness. The results of the more complete expansion study (Fälth and Hökmark 2012) are sufficient to cover for the cases addressed in the first study.

Forsmark

- End-glacial earthquakes on ZFMA2 (Fälth et al. 2015, 2016).
- Thermally induced earthquakes on ZFMA2 (Fälth and Hökmark 2013; Summarised in Appendix A).
- Present-day earthquake on ZFMA2 (Fälth and Hökmark 2013).

In the near vicinity of the Forsmark repository, only the gently dipping ZFMA2 deformation zone has been considered as a potential earthquake fault (Fälth et al. 2016). As shown in Figure 3-2 (right), the ZFMA2 zone is, as opposed to the other zones located within or in the near vicinity of the repository footprint, close to the stability limit ($CFS=0$) under present-day conditions. Gently dipping zones, such as ZFMA2, would also, as opposed to other zones, all steeply dipping, be further destabilized at the time of ice retreat after a future glaciation, while the steeply dipping deformation zones would be further stabilized.

All deformation zones modelled within the studies listed above have been assumed to be perfectly planar. The details of the rupture mechanism have been specified to produce ruptures that are in principle seismologically credible (e.g. time-weakening rupture models with rupture propagation in keeping with empirical data or, in some of the cases, slip-weakening models with spontaneous rupture propagation) but also, in most cases, with stress drop parameters (i.e. parameters controlling the shear strength before and after rupture) set to give moment magnitudes that are higher than typical magnitudes reported in the literature for earthquakes with similarly sized rupture areas. In all simulations listed above, the critical output has been the seismically induced slip on explicitly modelled target fractures located at different distances from the rupturing fault.

4.2 Scope and objectives of this overview

The purpose of this overview is to summarize the most important results of the studies listed in the previous section, i.e.:

- The main characteristics of all earthquakes modelled, i.e. rupture area and moment magnitude. For all Forsmark models and some of the Olkiluoto models also the maximum fault displacements are presented and compared with empirical data.
- For each earthquake modelled: The largest seismically induced target fracture slip found at each of the different distances considered in the model.

4.2.1 Moment magnitude – rupture area

In the following sections the moment magnitudes of all 3DEC earthquakes listed above are plotted vs rupture area along with corresponding data for real earthquakes in diagrams of the type shown in Figure 4-1 (upper). In this example plot, only a few of the many synthetic 3DEC earthquakes simulated and described in the reports listed above are included. As in the complete plots shown in following sections, moment magnitudes of the synthetic 3DEC earthquakes typically plot above, or well above, regressions established between rupture area and magnitude for real earthquakes. It is worthwhile to note that the synthetic 3DEC earthquakes systematically involve the entire, full size, area of the fault hosting the earthquake, while the rupture area for real earthquakes typically would make out some fraction of the fault area. Data on these relations are scarce but Slemmons and Chung (1982), cited in Krinitzsky et al. (1993), estimated the rupture to constitute about 15–40 % of the fault trace length. In Figure 4-1 (lower) it has arbitrarily been assumed that the rupture area of a typical database earthquake makes out 50 % of the total fault area. Although the 50 % assumption is very arbitrary, it seems clear that there is a considerable built-in magnitude overestimate in most of the synthetic 3DEC earthquakes (100 % of the fault area ruptured).

4.2.2 Induced fracture slip

For the earthquake simulations considered in this overview (see list in introduction section) the main concern has been to arrive at estimates of induced shear displacement along differently oriented host rock fractures (target fractures) located at different distances from the rupturing (principal or primary) fault, sometimes referred to as distributed faulting Coppersmith and Youngs (2000). Figure 4-2 shows an example of the format used to present the results in the studies listed in Section 4.1. In this example a number of 300 m diameter target fractures, located at repository depth at distances between 300 and 4500 m from a hypothetically extended version of the steeply dipping, nearly vertical, Olkiluoto BFZ214 deformation zone, slip in response to a strike-slip earthquake occurring on that fault zone under present-day stress conditions (Fälth and Hökmark 2015). There are two separate regions of

target fractures: one around fault mid-length (Region #1) where stress concentrations around a maximally sharp fault inhomogeneity tend to give rise to considerable secondary effects at the smallest distances. In Region #2, away from the inhomogeneity and the stress concentrations, the secondary effects are modest.

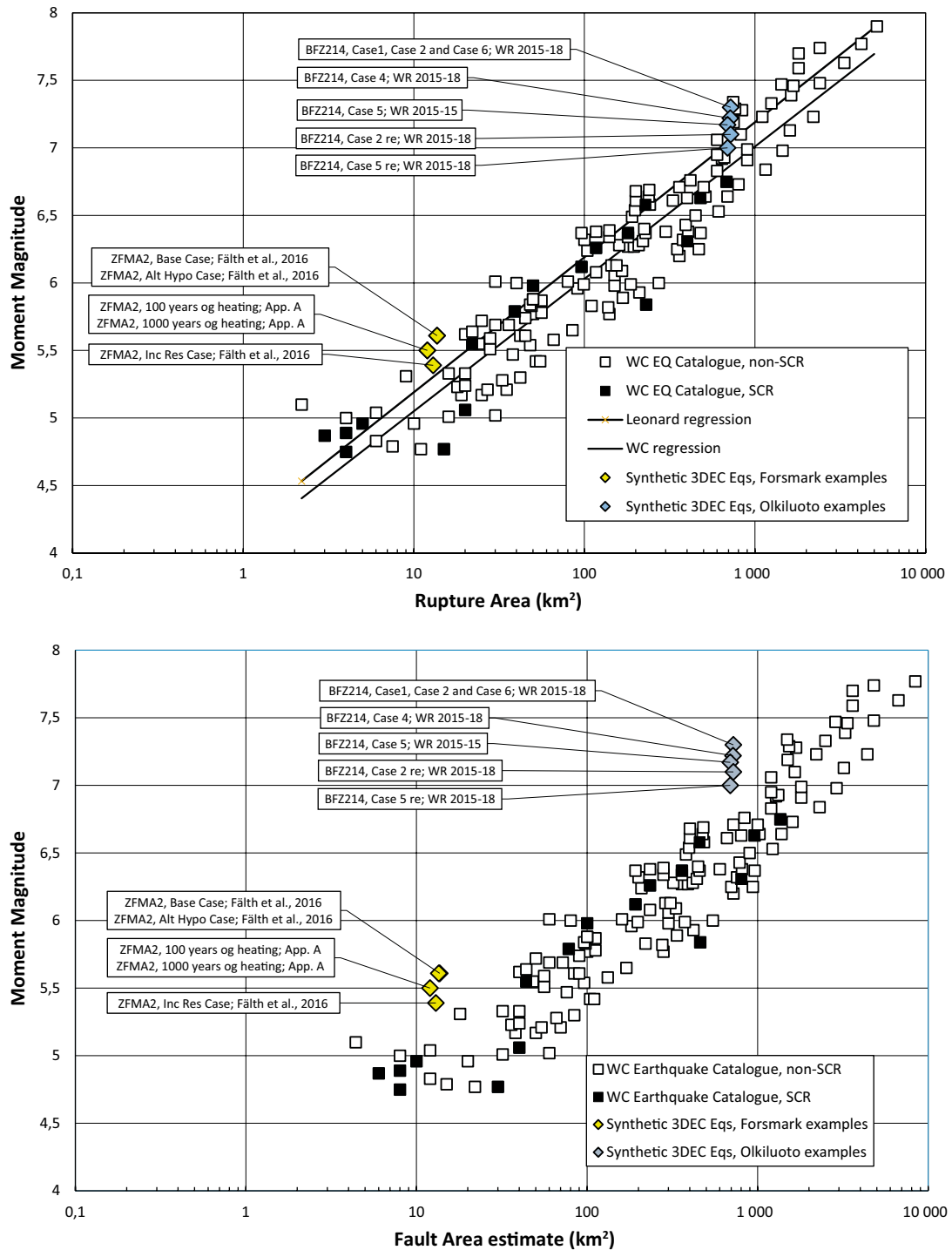


Figure 4-1. Upper: Moment magnitude vs rupture area. Some of the synthetic 3DEC earthquakes discussed herein are plotted along with the Wells-Coppersmith database earthquakes (Wells and Coppersmith 1994). Black plot symbols correspond to stable continental region earthquakes. Lower: same as upper but horizontal axis is fault area. Here it is arbitrarily assumed that the rupture area of typical database earthquakes would be 50 % of the full fault area (Data on this issue are sparse and difficult to evaluate. For major transform zones, Slemmons and Chung (1982) presented correlations between surface rupture and fault length indicating that surface rupture typically would make out around 30 % of the fault length.)

Although it is not within the scope of this overview to go into the details of any of the modelling cases, it should, for completeness, also be mentioned that the BFZ214 model with the fault inhomogeneity was analysed for two cases with different assumptions regarding the rupture parameters that control the seismic efficiency and, consequently, the stress drop and the resulting moment magnitude. Both magnitudes ($M_w = 7.17$ and 7.0 , respectively) are significantly higher than any magnitude reported for any SCR earthquake in the Wells and Coppersmith (1994) catalogue (Figure 4-1). In Figure 4-2, solid lines correspond to the M_w 7.0 version of the earthquake and dashed lines to the M_w 7.17 version.

The graphs in Figure 4-2 (which regard modelling cases 5 and 5re pictured in Table 4-1) do also show that it takes extreme assumptions (here a maximally sharp vertical fault inhomogeneity, for target fractures with a high initial stability (here steeply dipping fractures located in the Olkiluoto reverse faulting stress regime at repository depth) to slip by significant amounts. Out of the steeply dipping fractures included in the models (square plot symbols) only two (those at 300 m and 700 m distance from the sharp fault inhomogeneity) slip by more than insignificant amounts. In target fracture Region #2 (away from the sharp inhomogeneity) no steeply dipping fracture slip by more than 10 mm at any distance. In corresponding model versions with less sharp inhomogeneities or no inhomogeneities, no steeply dipping fractures slip by more than about 12 mm, see Fälth and Hökmark (2015) for details. See also discussion in Section 2.3 of this overview about the relevance of the distinction made between gently and steeply dipping fractures in the SR-Site background material.

The cumulative graphs, such as the ones in Figure 4-2, show the slip on all target fractures. In the following results overview, only the largest slip found at the different fault-fracture distances considered in the different models will be presented. The target fractures considered in Figure 4-2 are all 300 m in diameter, while target fractures in some analyses are 150 m in diameter. To allow for comparisons between all results, target fracture slip is normalized in the following (i.e. given as mm of slip per m of fracture diameter). For static loads this scaling is analytically verifiable if a homogeneous elastic medium and circular fractures are assumed (Segedin 1951, Eshelby 1957).

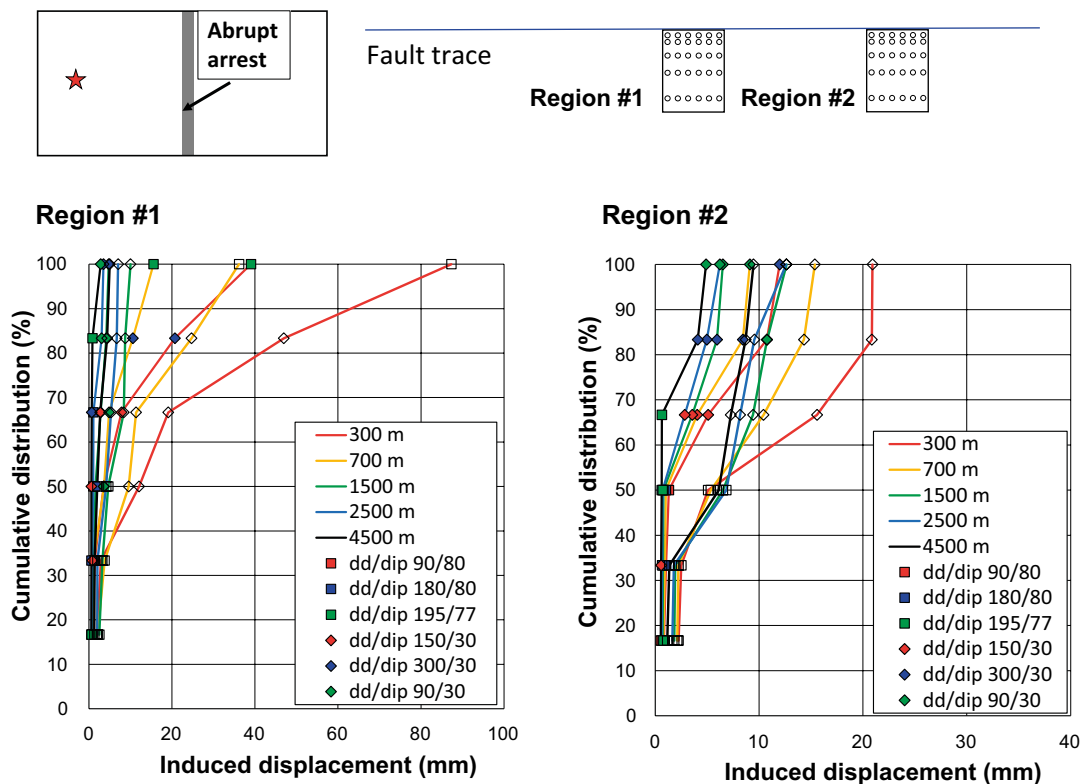


Figure 4-2. Example illustrating the way of presenting target fracture slip results in the studies covered in this overview (Figure 6-3 in Fälth and Hökmark 2015). Dashed and full lines correspond to different versions of a particular BFZ214 (Olkiluoto) earthquake, see corresponding text. Note that the horizontal scales differ between the two diagrams.

As mentioned earlier, Fälth et al. (2010) demonstrated that it is justified also for the type of dynamic loads generated by synthetic 3DEC earthquakes. To exemplify: For the BFZ214 models considered in Figure 4-2, the maximum induced displacements on 300 m diameter fracture at 300 m distance are 89 mm or 0.30 mm/m (M_w 7.17; dashed lines) and 40 mm or 0.13 mm/m (M_w 7.0; full lines). Both these results are found in Region #1. At the 4500 m distance corresponding results are 0.03 mm/m and 0.013 mm/m, respectively. Both these results are found in Region #2.

4.2.3 Fault-fracture distances

Fault-fracture distances are taken as the perpendicular distance from the centre of the fracture to the plane of the primary fault, even for cases where this is not the shortest fault-fracture distance. For gently dipping faults, say faults dipping by 20 degrees, the shortest fault-fracture distance for fractures located at the footwall side far away from the fault would be the distance to the fault surface trace.

Also, for faults not reaching the ground surface, or even the depth of the target fractures, there will be cases where the real fault-fracture distance will be underestimated. This will be commented where appropriate in the following (see e.g. Figure 4-9).

In some cases, target fractures are located between fault splays. In those cases, the distance is in general taken as the distance to the plane of the main fault or, where appropriate, to the splay with the largest slip and the largest impact on the surrounding rock at repository depth.

4.3 Overview structure

The synthetic 3DEC earthquakes are separated in two categories in this overview:

- Earthquakes occurring on local, small or medium-sized, mapped deformation zones with orientations and sizes approximately as given in the site description at hand at the time of the modelling.
- Earthquakes occurring on mapped deformation zones with areas hypothetically extended to allow for large, or very large, earthquakes.

For the local scale models the driving stresses are based on site model stress fields, extrapolated to a few kilometres depth. Glacial stresses obtained from large-scale crust analyses conducted assuming the reference glacial cycle constructed using the UMISM ice sheet model (see e.g. Hökmark and Fälth 2014) or thermal stresses obtained from repository-scale thermo-mechanical analyses (see Appendix A) are added as required. The local scale earthquakes are described in Section 4.4.

The large synthetic earthquakes occur on mapped deformation zones that are extended to investigate the consequences of earthquakes occurring on large, possibly not sufficiently well characterized (or identified) nearby or distant features. As opposed to the local models, the in-situ stresses in the large-scale models are set to give small stability margins at all depths and make large earthquakes involving the majority of the fault area under consideration, at least theoretically, a physically realistic possibility. At depths of a few km and below, these stress fields differ significantly between models of large earthquakes occurring on steeply dipping and gently dipping zones, i.e. the type of earthquakes considered here cannot be a theoretical possibility for both types of large zones. Glacial stresses are added as for the local scale models as required. The large-scale earthquakes are described in Section 4.5.

Results of simulations of earthquakes occurring on the system of connected, gently dipping Olkiluoto deformation zones BFZ020, BFZ021 and BFZ099 (Fälth et al. 2019) are presented in both sections (Section 4.4 and Section 4.5) depending on the different hypothetical assumptions made regarding the extension of these deformation zones.

All synthetic earthquakes described here, local and large scale, are plotted in Rupture Area – Moment Magnitude diagrams along with real, similarly sized, database earthquakes. Figure 4-3 shows the full database relation between rupture area and moment magnitude for all crustal earthquakes considered by Wells and Coppersmith (1994) along with regressions established by Wells and Coppersmith (1994) and Leonard (2010). Earthquakes occurring in stable continental regions (SCR), such as the Baltic shield, are plotted with black squares (no Baltic shield earthquakes are, however, included in the database). The two coloured rectangles indicate the plot windows used for the local scale (Figure 4-4) and the large scale (Figure 4-7) synthetic earthquakes, respectively, in the following.

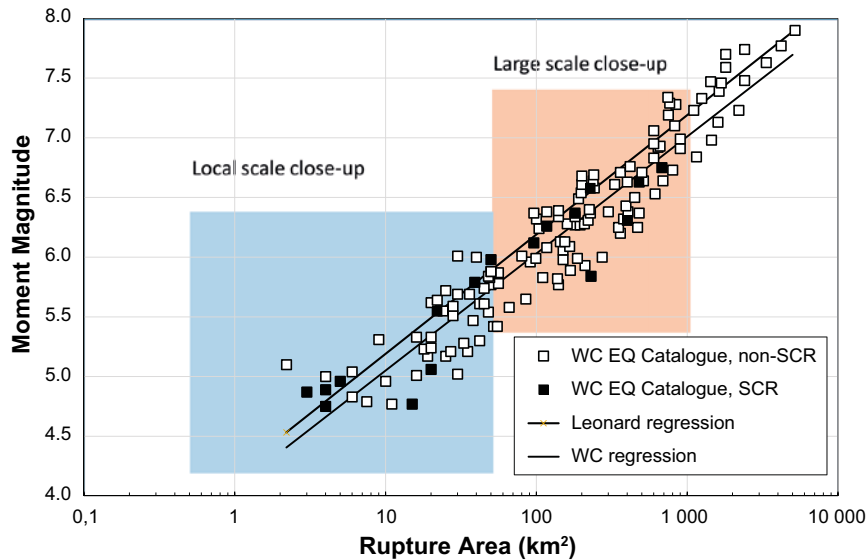


Figure 4-3. Moment magnitude vs rupture area for crustal earthquakes according to Wells and Coppersmith (1994). SCR means earthquakes in Stable Continental Regions. Regressions are according to Wells and Coppersmith (1994) and Leonard (2010). The coloured rectangles indicate plot windows used in the following for comparison between local scale (Figure 4-4) and large (Figure 4-7) synthetic earthquakes, respectively, with database earthquakes. Note that no SCR earthquakes have magnitudes exceeding those covered in the large-scale EQ close-up window.

4.4 Earthquakes occurring on small and medium-sized local DZ's

Figure 4-4 shows a close-up of the local scale database plot window in Figure 4-3. Synthetic earthquake results are plotted along with the Wells and Coppersmith (1994) database earthquakes and with regression between moment magnitude and rupture area given by Wells and Coppersmith (1994) and Leonard (2010). Recall that none of the results obtained in the first Olkiluoto study (Fälth and Hökmark 2011) are included. The results of the more complete expansion study (Fälth and Hökmark 2012) are sufficient to cover for the cases addressed in the first study. Data labels with information on moment magnitude, rupture area and the report or study containing the full model information are coloured white, orange and green for present-day earthquakes, thermally induced earthquakes and end-glacial earthquakes, respectively.

Figure 4-5 is a summary of the off-fault effects of the different synthetic earthquakes: the largest normalized induced fracture shear displacement (mm of slip per m of fracture diameter) found at the different distances considered in the analyses. As illustrated by the example shown in Figure 4-2, the majority of the fractures slip by significantly smaller amounts. In Figure 4-5, results obtained for earthquakes on gently dipping zones and steeply dipping zones are plotted in the upper and lower parts, respectively. Results from analyses of present-day earthquakes (PD), thermally induced earthquakes (Th), forebulge earthquakes (Fb) and end-glacial earthquakes (EG) are plotted in differently coloured plot segments. Up to the present day no simulation of earthquakes occurring on local scale deformation zones under forebulge stress conditions have been performed (see short discussion on forebulge seismicity in Section 3.2.4).

Fracture-fault distances are in most cases exactly those given in the legend. In some cases, however, where more than one fault is involved, distances may have had to be rounded to $n \cdot 100$ m; see also comments on fault-fracture distances in Section 4.2.3. In general, secondary displacements decrease with increasing distance from the fault plane. There are, however, exceptions: in the end-glacial Olkiluoto BFZ021 models reported by Fälth and Hökmark (2012), the maximum secondary slip at 500 m distance is about 4 mm larger than the maximum displacement at 100 m distance (150 m diameter fractures). The exact reasons for this counterintuitive result are not clear, but could be coupled to the almost complete stress relaxation in the tip of the wedge-shaped hanging wall or to surface reflections. It could also, as suggested by the sense of shear noted for the counterintuitively slipping fractures, be coupled to the low shear stiffness assumed for the fractures in this particular model, see Fälth and Hökmark (2012).

Figure 4-4 and Figure 4-5 together contain the essence of the results of all 3DEC simulations of earthquakes with magnitudes smaller than 6.0 performed up to the present day within the Posiva and SKB programs carried out to find safe bounds to seismically induced shear displacement along host rock fractures in Olkiluoto and Forsmark. With one exception, each labelled plot symbol in Figure 4-4 corresponds to a similarly labelled set of results in Figure 4-5. The exception is the magnitude 5.5 present-day earthquake on the ZFMA2 zone in Forsmark. This particular model did not include any explicitly modelled fractures, since it is obvious that any target fracture slip would be even smaller than the modest target fracture slip obtained in the corresponding thermal models (with identical hypocentre locations and rupture processes, but more instability among the target fractures optimally oriented for slip).

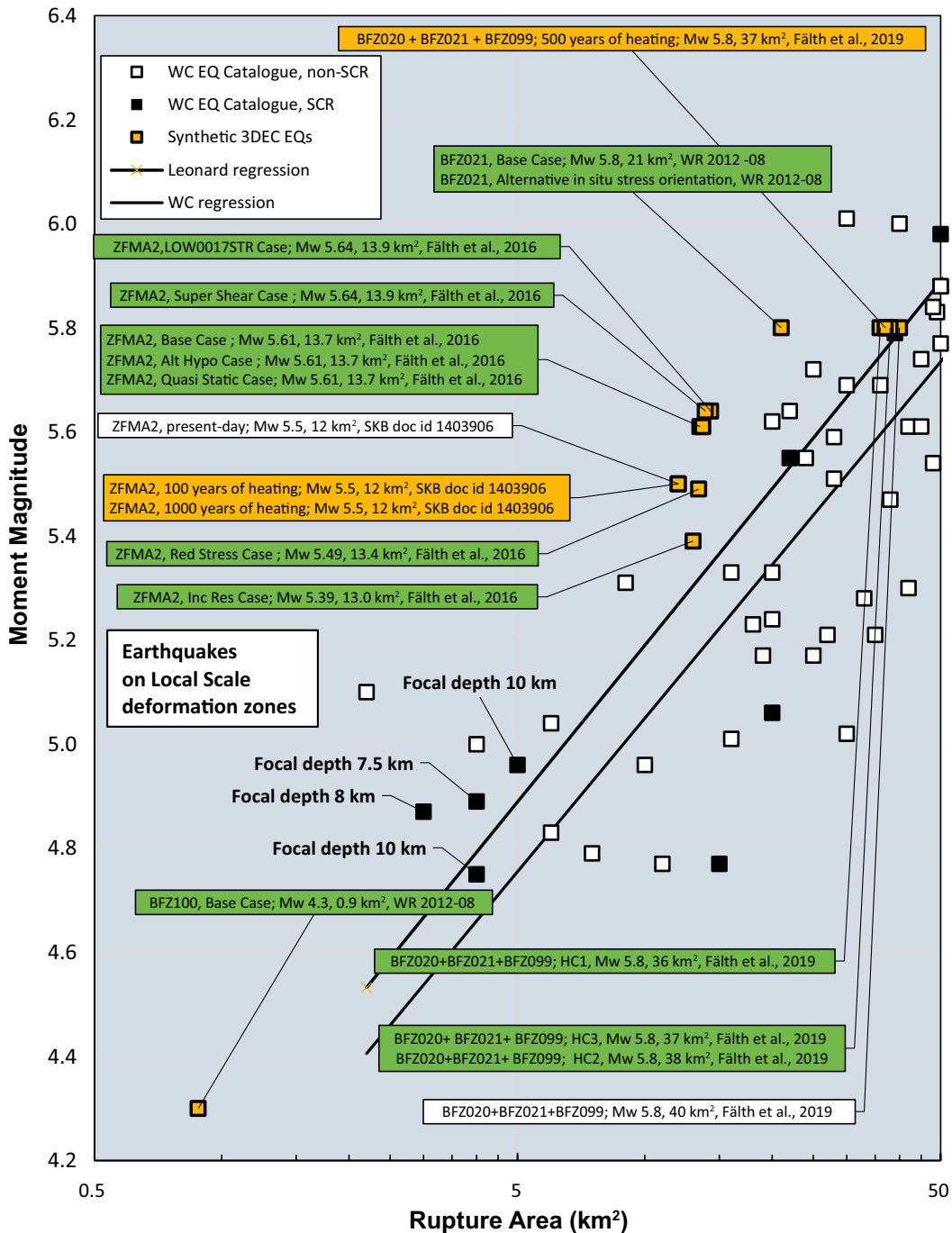


Figure 4-4. Synthetic local scale 3DEC EQs plotted along with Wells and Coppersmith (1994) data and regressions established by Wells and Coppersmith (1994) and Leonard (2010) (cf. local scale plot window in Figure 4-3). White data labels mean present-day EQs, orange labels mean thermally induced EQs and green labels mean end-glacial EQs.

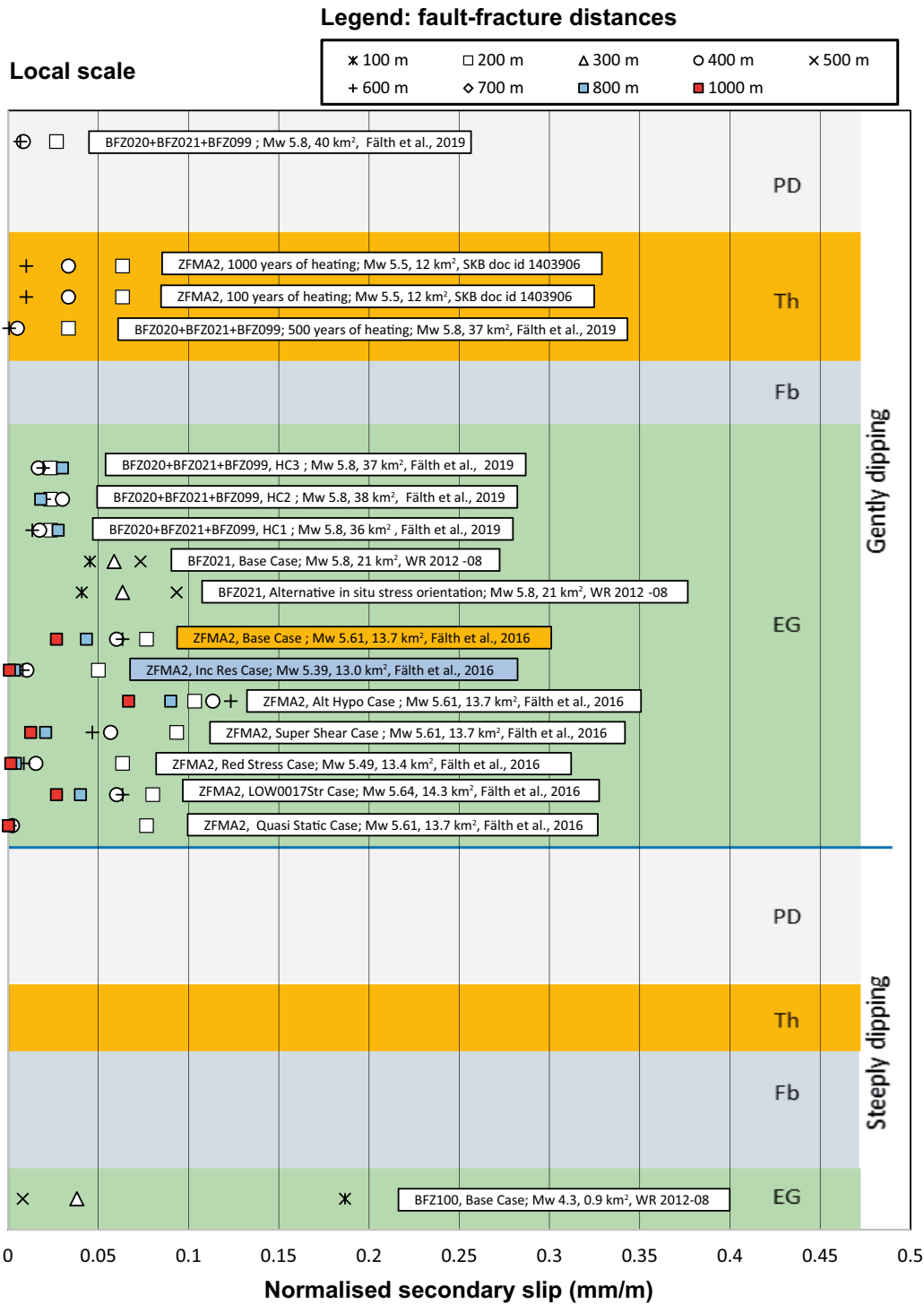


Figure 4-5. Maximum target fracture slip (normalized to mm of slip per m of fracture diameter) obtained in a number of different analyses of earthquakes occurring on local small and medium sized deformation zones. The two coloured labels correspond to models with identical rupture protocols and hypocentre locations, but with different stress drops. Note that all plot above the Leonard regression in Figure 4-4. The steeply dipping BFZ100 Olkiluoto zone is actually stabilised under end-glacial conditions. The BFZ100 results are included here for completeness only.

It should be mentioned here that for the ZFMA2 models, only results for target fractures located on the footwall side are plotted in Figure 4-5. No deposition areas are will be located on the hanging wall side.

One important observation is that the 3DEC earthquakes plot above, or well above, the regressions (Figure 4-4). Yet, there is, as pointed out earlier, an additional built-in magnitude overestimate: For the synthetic earthquakes the rupture areas coincide with the fault areas, which is not the case for the database earthquakes. A more adequate way of comparison would be to plot the database magnitudes vs fault

area instead of vs rupture area. This would push the database plot symbols to the right by different (but varying and uncertain) amounts (cf. Figure 4-1, lower) and indicate even stronger that the magnitudes of the synthetic earthquakes are indeed upper bounds to reasonably realistic magnitudes of real crustal earthquakes on fault zones with given areas.

Out of more than thousand target fractures considered in the different models very few slip by more than 0.1 mm/m. This corresponds to 20 mm of slip along a 200 m diameter fracture. For the largest slip (0.18 mm/m at 100 m distance from the Olkiluoto BFZ100 deformation zone, rupturing under end-glacial stress conditions), the following should be noted:

1. The BFZ100 event plots well above the (extrapolated) Leonard (2010) regression in Figure 4-4.
2. The BFZ100 fault area (as given in the site description at hand at the time of the simulation) is only 0.9 km². This means that all target fractures at the closest distance (100 m) are located within reach of stress concentrations around schematically represented, infinitely sharp, fault edges.
3. The maximum shear displacement on the BFZ100 model fault appears to be extremely large compared to corresponding data for real crustal earthquakes (Figure 4-6.)

The above facts are with good margins sufficient to allow for the BFZ100 results shown in Figure 4-5 to be disregarded. It should also be mentioned that the BFZ100 zone actually would be more stable under end-glacial conditions than under present-day conditions (Hökmark and Fälth 2014) for the reference ice model and should not count as a potential end-glacial fault zone. The BFZ100 results are shown here for the sake of completeness only.

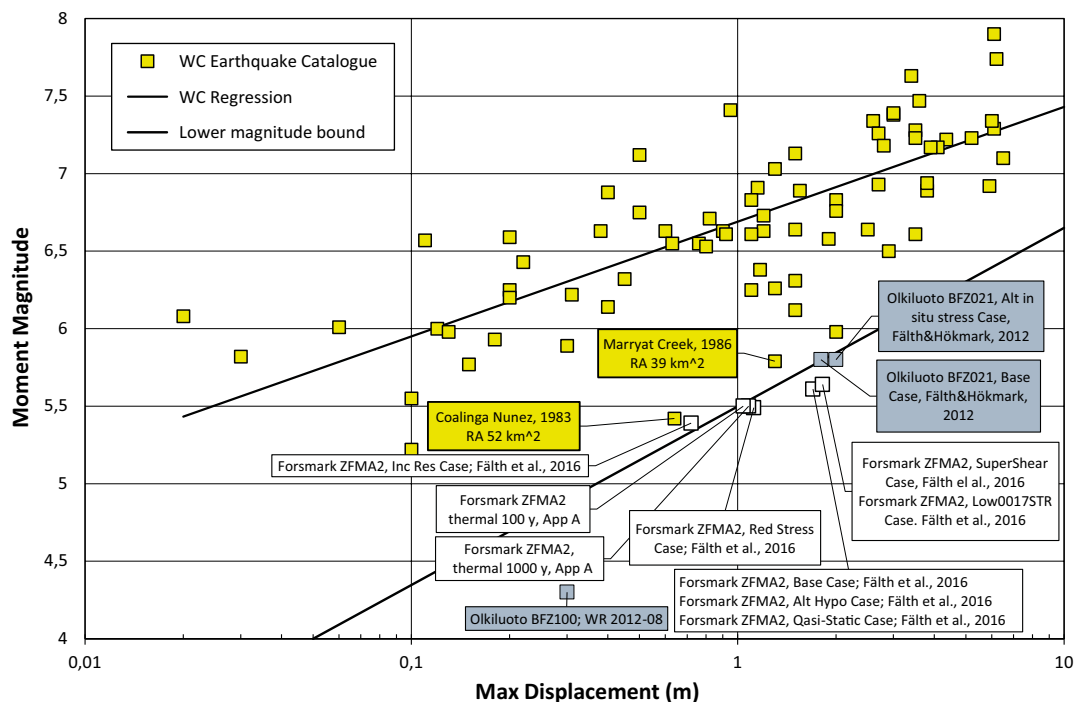


Figure 4-6. Maximum primary fault slip obtained in the ZFMA2 models plotted in Figure 4-4 and Figure 4-5 (white) along with corresponding catalogue data (Wells and Coppersmith (1994) and a few Olkiluoto results (also included in Figure 4-4 and Figure 4-5 (blue)). The moment magnitudes of the synthetic earthquakes are clearly at the lower bound of what would be required to produce the fault displacements obtained here. The ZFMA2 “Inc Res Case” plots marginally above the arbitrarily established “lower magnitude bound” but below all catalogue events with similar max displacements and would be a safe bounding case for the effects of an earthquake occurring on ZFMA2. Note also that the rupture area of the catalogue earthquakes plotting closest to the ZFMA2 events are significantly larger than that of the ZFMA2 fault area (around 14 km²). In comparison with empirical data, the primary slip on the Olkiluoto BFZ100 zone is at least one order of magnitude too large to count as even close to realistic.

It should also be pointed out that the three conditions above apply, at least to some extent, also to the ZFMA2 models. 1): all plot well above the regressions, 2): the ZFMA2 zone is small enough that some fractures are located close to sharp fault edges and 3): as shown in Figure 4-6, the maximum shear displacement on the fault plane is considerably larger than that of all database earthquakes of similar or smaller magnitudes.

Conditions 1 and 3 apply also to the BFZ021 models reported by Fälth and Hökmark (2012). No target fractures were, however, located close enough to the edges of the 21 km² deformation zone for edge effects to impact.

A conclusion of the above should be that induced slip results in excess of 0.1 mm/m are consequences of combinations of extreme input assumptions. For the ZFMA2 deformation zone in Forsmark, a modified version of the “Base Case” model was analysed to verify this (Fälth et al. 2016). In the modified version, the “Inc Res Case” model, the residual strength of the fault was increased in order to reduce the stress drop and bring the moment magnitude closer to, but still above, the Leonard regression (cf. Figure 4-5). The seismic moment was reduced by more than 50 %, corresponding to a moment magnitude reduction from 5.61 to 5.39. The maximum displacement in the modified version (0.72 m, cf. Fälth et al. 2016) is still much larger than the maximum fault displacement of all database earthquakes of similar magnitudes (see Figure 4-6.).

A conclusion of the above is that 0.1 mm/m normalized induced slip would be a safe upper bound estimate for seismically induced displacements occurring at 100–200 m distance from local, small or medium sized, deformation zones.

As a matter of fact, it appears in Figure 4-4 that all secondary displacements exceeding 0.05 mm/m in Figure 4-5 are based on models with moment magnitudes plotting 0.18–0.31 magnitude units above the Leonard regression. This corresponds to a seismic moment excess of between 85 % and 190 %. This means that there are margins to the 0.1 mm/m upper bound estimate. Yet the quantitatively very uncertain rupture area overestimate (cf. Figure 4-1, lower) has not been accounted for. Nor has the impact of target fracture undulations, steps or asperities been accounted for. Modest deviations from planarity, e.g. undulations or steps on an otherwise smooth fracture surface with mechanical properties (friction coefficient etc.) according to lab scale parameter values given in the site reports, could further reduce the largest target fracture displacements by tens of percent (Lönnqvist and Hökmark 2015b).

4.5 Earthquakes occurring on large DZ's

Figure 4-7 shows a close-up of the large-scale database plot window in Figure 4-3. Synthetic 3DEC earthquake results are plotted along with the Wells and Coppersmith (1994) database earthquakes and with regressions between moment magnitude and rupture area given by Wells and Coppersmith (1994) and by (Leonard 2010). Data labels with information on moment magnitude, rupture area and the report containing the full model information are coloured white, orange, grey and green for present-day earthquakes, thermally induced earthquakes, forebulge earthquakes and end-glacial earthquakes, respectively.


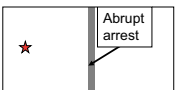
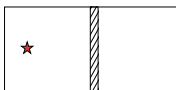
Figure 4-8 is a summary of the off-fault effects of the different synthetic earthquakes: the largest normalized induced fracture shear displacement found at the different distances considered in the analyses. As illustrated by the example shown in Figure 4-2, the majority of the fractures slip by significantly smaller amounts. In Figure 4-8 results obtained for earthquakes on gently dipping zones and steeply dipping zones are plotted in the upper and lower parts, respectively. Results from analyses of present-day earthquakes (PD), thermally induced earthquakes (Th), forebulge earthquakes (Fb) and end-glacial earthquakes (EG) are plotted in differently coloured plot segments. Fracture-fault distances are in most cases exactly those given in the legend. In some cases, however, where more than one fault is involved, distances may have had to be rounded to nearest hundreds of meters (see also comments on fault-fracture distances in Section 4.2.3).

Figure 4-7 and Figure 4-8 together contain the essence of the results of all 3DEC simulations of earthquakes with magnitudes larger than 6.0 performed up to the present day within the Posiva and SKB programs carried out to find safe bounds to seismically induced shear displacement along host rock fractures in Olkiluoto and Forsmark. Each labelled plot symbol in Figure 4-7 corresponds to a similarly labelled set of results in Figure 4-8.

The 25 modelling cases shown in Figure 4-8 include in total about 2800 differently oriented and located target fractures out of which about 260 are located at the smallest distance considered from the rupturing fault (200 or 300 m). Out of all these fractures, only one slips by more than 0.25 mm/m (which, for a 200 m diameter fracture would correspond to 50 mm of slip). Looking at Figure 4-8 from top to bottom it appears that only few slip by more than about 0.12 mm/m:

- The present-day earthquakes modelled on a system of gently dipping Olkiluoto deformation zones generate target fracture slip in excess of 0.12 mm/m for cases (“non-homogeneous model versions”) with stress concentrations around schematic high-stability patches located at repository depth (Fälth et al. 2019). For corresponding models without these patches, the maximum secondary slip is less than 0.12 mm/m. All these events (with and without stability patches) plot well above the Leonard regression (Figure 4-7). For details on these models, see Fälth et al. (2019).
- End-glacial earthquakes modelled on a system of gently dipping Olkiluoto deformation zones (all hypothetically extended in comparison to the fault size data given in the Olkiluoto site description) generate slip of about 0.12 mm/m (corresponding to 24 mm of slip on a 200 m diameter fracture) for one particular case with a sharp horizontal fault edge just beneath the repository (BFZ201, Case 4 (sharp edge), see Figure 4-9). In the other cases, all plotting above the Leonard regression (Figure 4-7), the maximum induced secondary slip is less than 0.1 mm/m. For details on these models, see Fälth et al. (2019).
- An additional example of the above (impact of sharp high-strength fault asperities) is the set of results of present-day earthquakes simulated on a large steeply dipping fault (hypothetically extended version of the Olkiluoto BFZ214 zone). The largest target fracture slip induced at the closest distance (300 m) are shown in the top row of Table 4-1 for three cases with identical conditions regarding rupture parameters and the location of the hypocentre. These are the Base Case (Case 2) with a homogeneous fault area, Case 5 with a 1.5 km wide strip of infinite strength and Case 4 with a strip of high but finite strength. The three earthquakes plot well above the regressions in Figure 4-7 (In fact also well above the maximum magnitudes of all SCR earthquakes in the Wells-Coppersmith catalogue). In the bottom row of the table, corresponding results obtained in model versions (Case 2 re and Case 5 re) with rupture parameters set to reduce the magnitudes are shown. The magnitude of both these events do still plot well above the maximum magnitude of all SCR earthquakes included in the Wells-Coppersmith catalogue (Figure 4-7). The model with a soft strip, Case 4, was not tried with a limited magnitude. For more detailed information on the different BFZ214 analyses, see Fälth and Hökmark (2015).
- Among the present-day earthquakes simulated on the hypothetically extended version of the BFZ214 Olkiluoto deformation zone there is one additional model version (Case 1) giving maximum target fracture slip larger than about 0.12 mm/m at the closest distance considered. This can be attributed to the rupture mechanism used for this case: the stress peak travelling ahead of the rupture front was allowed to increase without limit, generating exaggerated stress effects at large hypocentre distances (See also comments in Section 3.4 and discussion on Alt Hypo Case result in Section 5.2).

Table 4-1. Maximum target fracture slip found in a set of simulations of a present-day earthquake on a hypothetically extended version of the steeply dipping BFZ214 Olkiluoto deformation zone (cf. Figure 4-8).

	No strip	Sharp strip edges	Soft strip edges
			
Rupture parameters set to maximize moment magnitude (orange labels in Figure 4-8)	Case 2 0.1 mm/m	Case 5 0.29 mm/m (red circle in Figure 4-8)	Case 4 0.08 mm/m
Rupture parameters revised to limit magnitude (blue labels in Figure 4-8)	Case 2 re 0.05 mm/m	Case 5 re 0.13 mm/m (red circle in Figure 4-8)	

The forebulge BFZ214 models do all plot well above the regressions in Figure 4-7. However, no fault irregularities are considered and the shear stress peak moving ahead of the rupture front was not allowed to increase without limits. Consequently, the target fracture displacements are modest. For details, see Fälth et al. (2019).

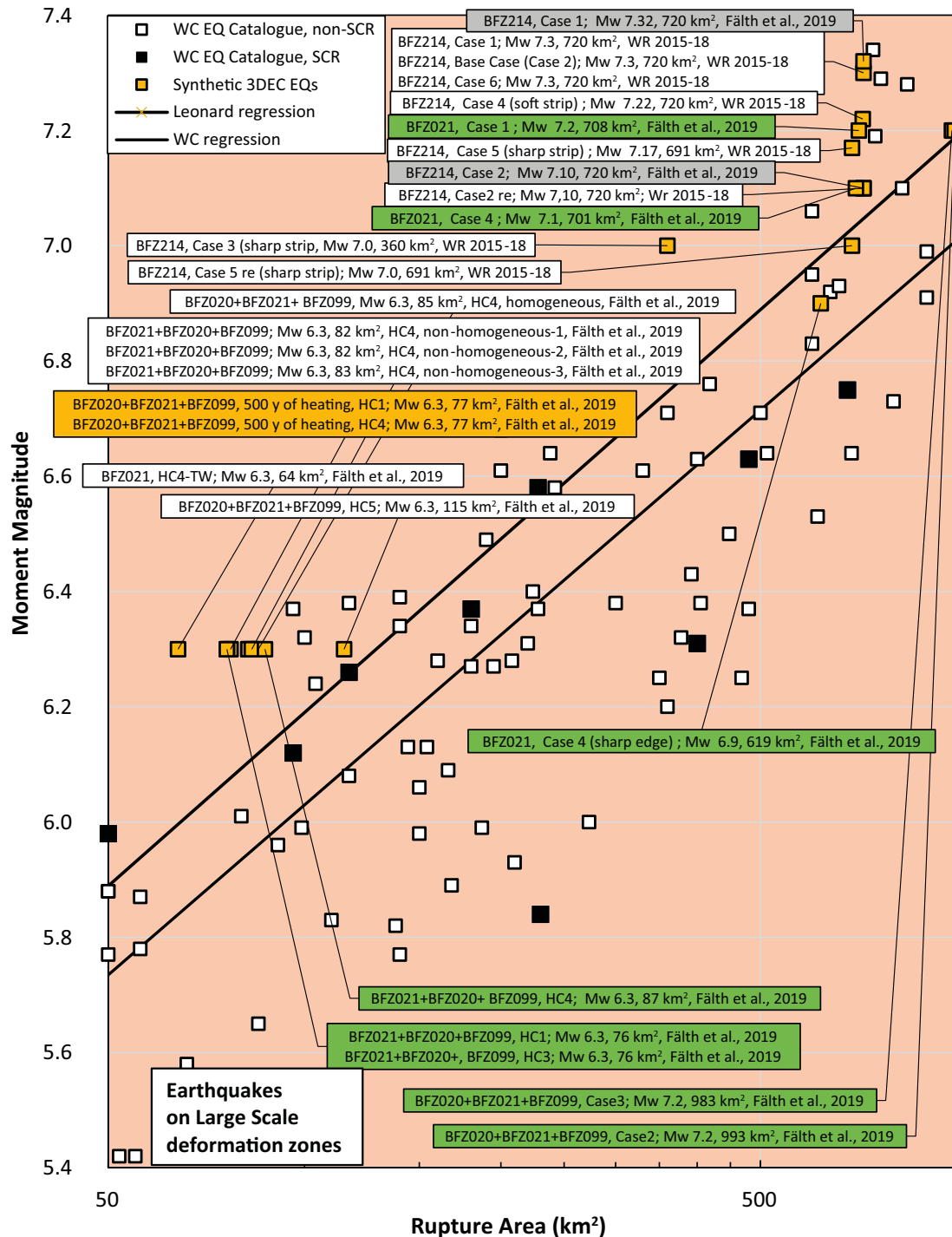


Figure 4-7. Synthetic large scale 3DEC earthquakes plotted along with Wells and Coppersmith (1994) data and regressions established by Wells and Coppersmith (1994) and Leonard (2010) (cf. large-scale plot window in Figure 4-3). White data labels: present-day earthquakes, orange labels: thermally induced earthquakes, grey labels: forebulge earthquakes, green labels: end-glacial earthquakes.

The discussion above and the results in Table 4-1, Figure 4-7 and Figure 4-8 together suggest that it takes either moment magnitudes that are too high to be credible or exaggeratedly sharp fault irregularities to produce secondary slip in excess of 0.12 mm/m at the distances considered in the simulations reported here (200–300 m). This corresponds to 36 mm of slip on 300 m diameter target fractures.

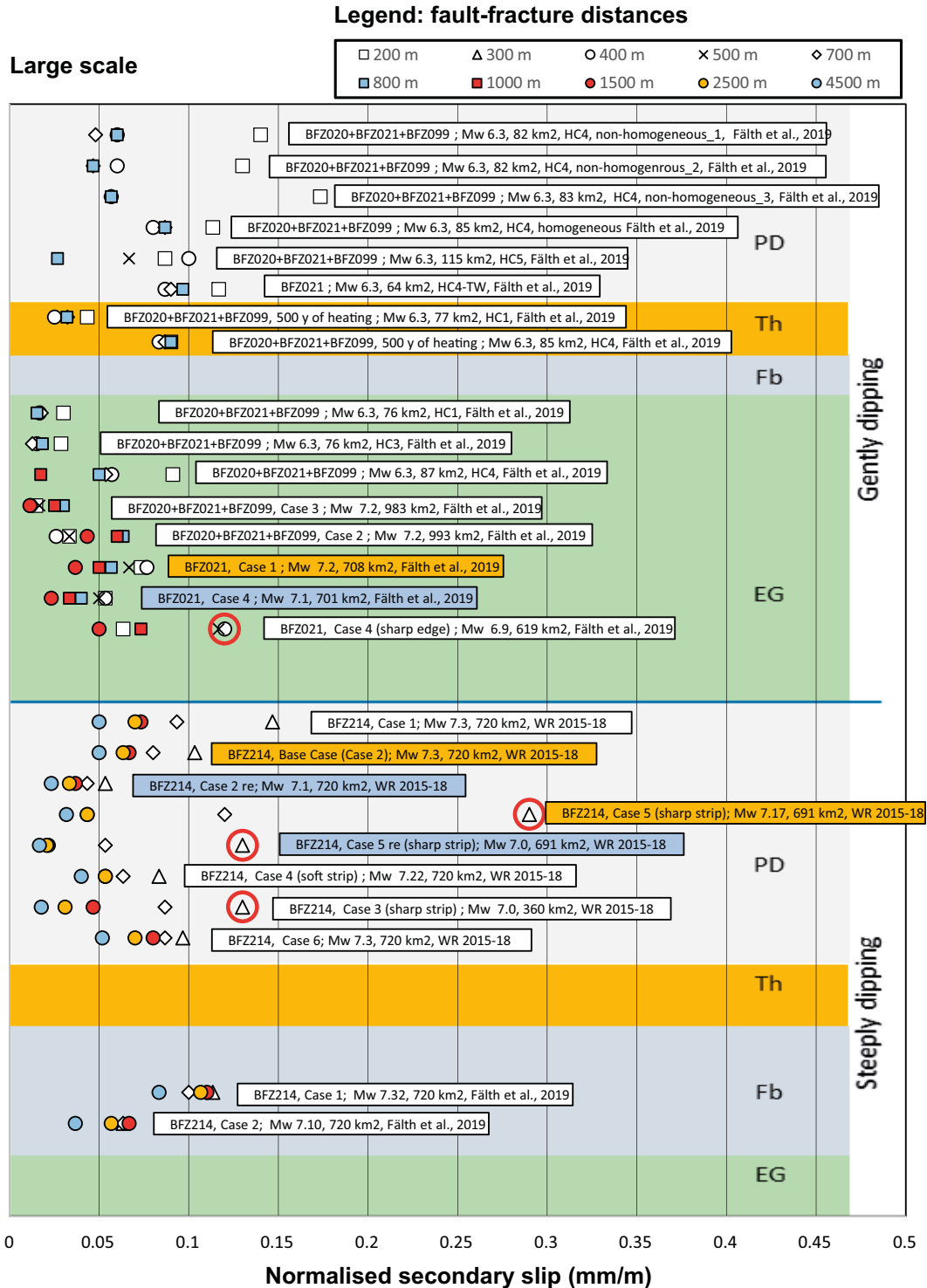


Figure 4-8. Maximum normalized target fracture slip at different distances obtained from analyses of earthquakes of magnitude 6 and larger. Red circles denote results shown to be dominated by stress concentration effects around sharp fault irregularities. For the case of PD earthquakes on the steeply dipping BFZ214 deformation zone, orange-coloured labels denote models with maximized magnitudes. Blue coloured labels denote corresponding model versions with slightly reduced magnitudes. Note that also the slightly reduced magnitudes are higher than that of all SCR events included in the Wells-Coppersmith catalogue (Figure 4-7).

It should be mentioned here that it is not, even theoretically, possible that the high magnitudes obtained here could be relevant for both steeply dipping and gently dipping deformation zones at the same time. For each of the different models, the stress field has been set to bring the fault surface close to instability at all depths, i.e. different stress fields have been assumed for models involving steeply dipping zones and models involving gently dipping zones. The hypothetical stress field approach taken to address the effects of earthquakes occurring on large, possibly poorly characterized deformation zones at some distance from the repository footprint, means that the results are equally relevant for the Forsmark and Olkiluoto sites.

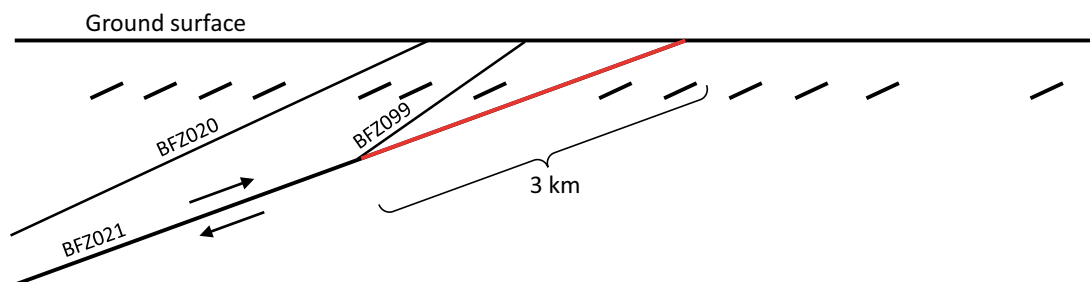


Figure 4-9. Schematics of two BFZ021 model versions, both with the fault extending about 9 km below ground surface, 27 km along strike and with hypocentres at 6 km depth (17 km downdip distance). In the “Case 4” version the BFZ021 deformation zone breaches the ground surface as described in the Olkiluoto site model. In the “Case4 sharp edge” version the rupture is completely and abruptly arrested at a sharp horizontal fault edge 600 m below the repository horizon (3 km downdip distance from the ground surface). “The Case 4 sharp edge” secondary slip results can be taken as the potential (however greatly exaggerated) effects of a large earthquake originating at depth under the repository horizon on an unknown fault that extends below the repository footprint to depths just sufficient to elude detection. Repository horizon is at the centre of target fractures (short black lines). From Fäth et al. (2019). Note that the fault-fracture distance regards the perpendicular distance to the fault plane also in cases when the rupture (as in the “Case4 sharp edge” model) does not reach the corresponding fault plane position, see Section 4.2.3 .

5 Critical radii at different fault-fracture distances

5.1 General

For the assessment of the seismic risk at Forsmark, it is essential to have a clear as possible picture of at what distances from differently sized deformation zones, and on which fractures, secondary displacements could exceed 50 mm. The following cases are relevant for this issue in Forsmark:

1. Earthquakes on the local, modestly sized, well described, gently dipping and potentially unstable ZFMA2 deformation zone. The repository is located at the footwall side of this zone. Among the deformation zones in the immediate vicinity of the repository footprint, the ZFMA2 zone is the only one that would be destabilized under end-glacial stress conditions, cf. Figure 3-2 and discussion in Section 3.2.3. It is also the deformation zone that, with very good margins, has the lowest stability under present-day stress conditions (cf. Figure 3-2 and discussion in Section 3.2.3).
2. Earthquakes on large, hypothetical, gently dipping deformation zones. These could represent distant, unidentified zones, zones or distant zones that are detected and identified but could appear to be of much larger extension in reality, or unidentified zones below the repository footprint.
3. Earthquakes on large, hypothetical, steeply dipping deformation zones. These could represent distant, unidentified zones or zones that are detected and identified but could appear to be of much larger extension in reality.

At large depths there are great uncertainties regarding the stress state, meaning that large earthquakes, at least theoretically, could occur on both gently dipping and steeply dipping zones, depending on the assumptions made regarding the stress field. Gently dipping zones would be further destabilized under end-glacial conditions while steeply dipping zones would be stabilized. For the following check on the impact of fault-fracture distance, the results from simulations of present-day and end-glacial earthquakes occurring on a system of gently dipping Olkiluoto zones (BFZ020, BFZ021 and BFZ099) are selected (Fälth et al. 2019). For corresponding check on the effects of earthquakes occurring on large steeply dipping zones, the results from simulations of present-day earthquakes and forebulge earthquakes occurring on a hypothetically extended version of the Olkiluoto BFZ214 zone are selected (Fälth and Hökmark 2015).

5.2 Earthquakes on ZFMA2

Figure 5-1 (upper) shows the maximum target fracture displacements plotted as function of distance from the ZFMA2 fault plane for a number of simulation cases as calculated by Fälth et al. (2016), cf. Figure 4-4 and Figure 4-5. Figure 5-1 (lower) shows corresponding results translated to critical radii. For comparison the critical radii applied in the SR-Site layout rules are included (black stepped line, see also Table 5-1 and Figure 2-3).

All these synthetic earthquakes, also those (Inc Res and Red stress cases) giving critical radii > 300 m at the closest distance tried in the simulations (200 m) plot above, or well above, the Leonard regression (cf. Figure 4-4). All, also those representing careful steps towards less exaggerated input assumptions (Inc Res and Red Stress cases), plot below the outliers in Figure 4-6. It should also be noted that all low magnitude Stable Continental Region (SCR) earthquakes plotting above the Leonard regression have focal depths of between 7 and 10 km (Figure 1-3b). It should also be noted that the Wells-Coppersmith outliers plotting closest to the ZFMA2 results in Figure 4-6 have rupture areas approximately between three and four times larger than the ZFMA2 rupture area. All this together may suggest that the Inc Res case would be an upper bound case when it comes to deciding on respect distances for the ZFMA2 zone.

Accepting the Inc Res or Red Stress case results as upper bound estimates of the secondary displacements that would be induced by earthquakes on ZFMA2 would obviously change the critical radii model very drastically. The results of the other models (Base Case, Alt Hypo, Super Shear etc.) are judged to be based on too exaggerated input assumptions to be relevant for the handling of the seismic risk.

One of the high magnitude model results (i.e. the Alt Hypo Case) indicate that there could be mechanisms that tend to generate displacements a few hundred meters away from the fault plane that are larger than those generated at 200 m distance. In the Alt Hypo Case the hypocentre is located in one of the lower corners of the fault plane some 1 900 meters down dip distance from the repository horizon while the hypocentre is located at the repository horizon in all other models. The counterintuitive Alt Hypo results with larger displacements at 600 m distance than at 200 m distance may be an effect of the unlimited growth of the stress peak generated in front of the moving rupture front which will tend to increase the dynamic stress disturbances at long hypocentre distances. As demonstrated by Fälth et al. (2016), stress disturbances at repository depth are dominated by dynamic effects in the Alt Hypo case on the footwall side, while quasi-static edge effects dominate in all other cases, cf. Figure 5-2 for a comparison of stress disturbances generated at repository horizon in the Base Case and the Alt Hypo Case (see Figure 8 in Fälth et al. (2016) and the associated discussion on fracture stability evolution).

It is beyond the scope of the compilation described herein to explore the details and establish the relative importance of the different mechanisms (exaggerated growth of stress peak ahead of the rupture front, surface wave reflections, style of interference between waves generated at different depths during rupture propagation, fault edge effects, etc.) that potentially could have contributed to the Alt Hypo Case results shown in Figure 5-1: 20 % larger max secondary displacement at 600 distance than at the 200 m distance (corresponding to 6 mm of additional shear displacement on a 300 m diameter fracture, i.e. on a fracture the size of about ten soccer fields).

It should, finally, be noted that the Alt Hypo model was analysed by Fälth et al. (2016) to explore if the effects on the 3DEC modelling results would be qualitatively logical and consistent with the input assumptions rather than to generate usable target fracture slip results.

Table 5-1 Critical radii at different distances from potential earthquakes zones with trace lengths between 3 and 5 km as applied in SR-Site.

Distance (m)	Critical radii, horizontal and gently dipping fractures (m)	Critical radii, steeply dipping fractures (m)
100–200	75	100
200–400	150	200
400–600	225	> 300
> 600	225	> 300

The target fracture slip pictured in Figure 5-1 do all regard slip on horizontal and gently dipping fractures which, due to the reverse stress regime at repository depth in Forsmark, systematically slip by significantly larger amount than steeply dipping fractures in all models analysed by Fälth et al. (2016). This means that the left column in Table 5-1 (cf. Also black stepped line in Figure 5-1 (lower) is the relevant one for comparison.

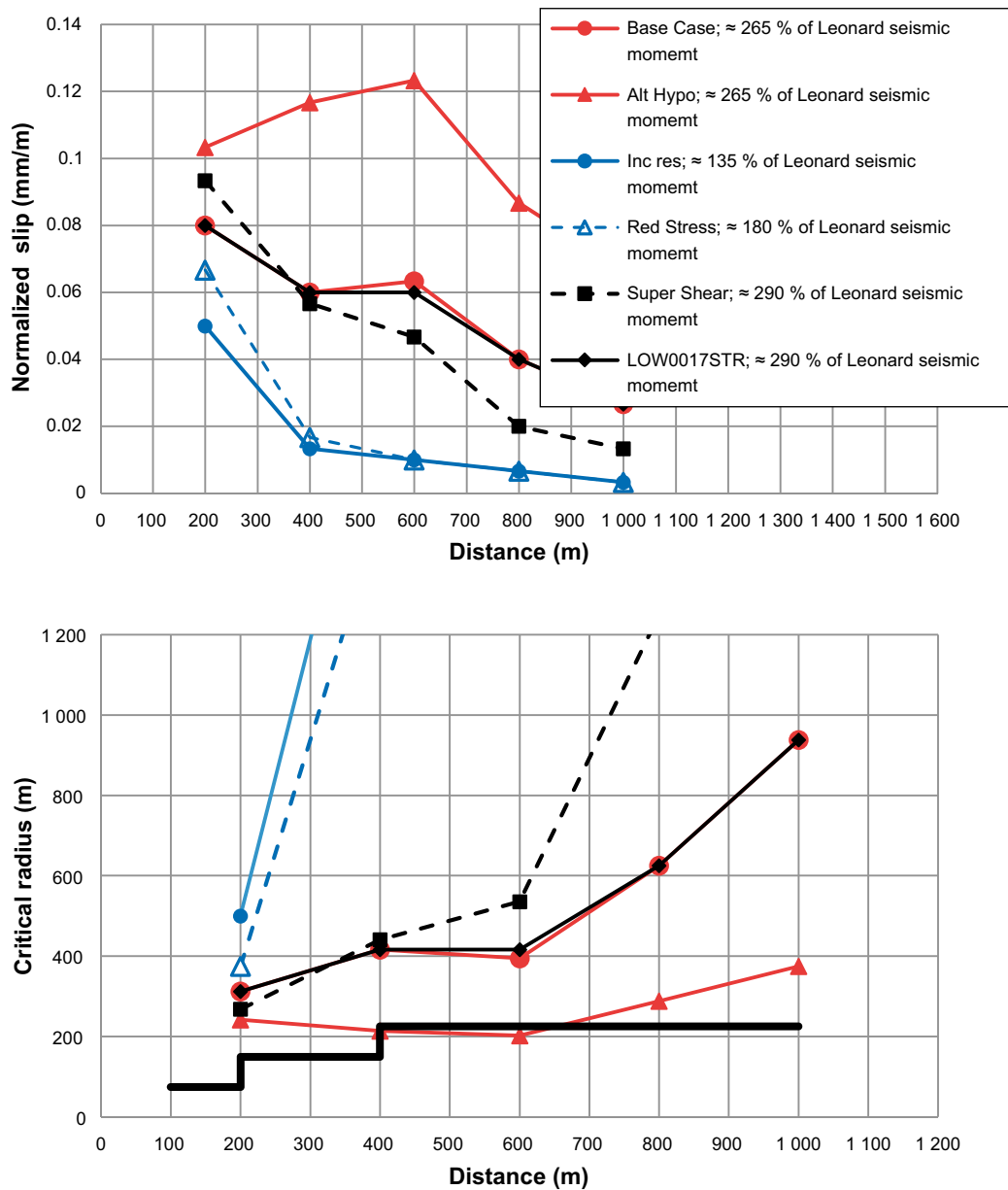


Figure 5-1. Upper: Maximum normalized slip at different distances from deformation zone ZFMA2. Lower: Smallest critical radii for fractures at different distances from ZFMA2. The black bold, stepped, line corresponds to the critical radii suggested in the SR-Site background material (cf. Table 5-1). For one case with an extremely exaggerated magnitude and with a rupture model allowing for unlimited growth of the stress peak travelling ahead of the rupture front from a large depth (Alt Hypo) the critical radii are marginally smaller than the SR-Site radii at about 600 m distance. For all other models, including models plotting well outside the outliers in the Wells-Coppersmith catalogue (Figure 4-6) the critical radii are much larger than the SR-Site radii. For models representing careful steps towards less exaggerated input assumptions, critical radii are approximately 400 m and more.

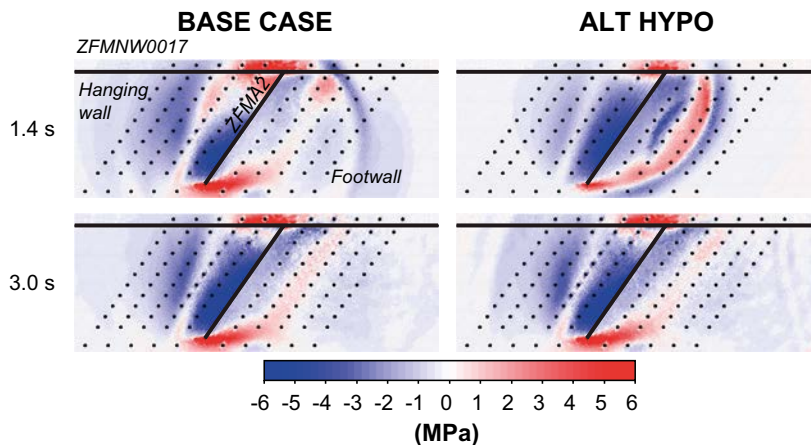


Figure 5-2. Upper: stability change in terms of CFS 1.4 seconds after rupture initiation in a horizontal section at repository depth in the Base Case (left) and in the Alt Hypo Case (right). Lower: Same after completed rupture 3.0 seconds after initiation when only permanent stress changes remain. Blue: increased stability. Red: reduced stability. After completed rupture the stability picture is essentially the same for the two cases with destabilized regions primarily around the fault edges. During rupture the stress waves contribute differently to the stability picture. In the Alt Hypo case a region of significantly reduced stability appears some distance away from the central parts of the fault. In the Base Case the quasi-static effects around the sharp fault edges dominate, giving maximum target fracture slip at the shortest distances. In the Alt Hypo Case, the dynamic effects are larger, which possibly contributes to the high maximum target fracture slip in the red-coloured region away from the central parts of the fault. CFS snapshots selected from Figure 8 in Fälth et al. (2016).

5.3 Earthquakes on large, gently dipping deformation zones

No simulations have been performed particularly for the Forsmark site to explore the effects of earthquakes on large, undetected deformation zones located under the repository footprint. In simulations of earthquakes on large gently dipping faults performed for the Olkiluoto site (Fälth et al. 2019), however, a reverse faulting stress regime was assumed at all depths in order to make a large earthquake a realistic possibility. Considering the hypothetical nature of an earthquake originating at depth in an uncertain stress environment, the results obtained in these simulations are judged to be as relevant for the Forsmark site as for the Olkiluoto site.

Figure 5-3 (upper) shows maximum normalized slip as function of distance for two of the end-glacial earthquakes and three of the present-day earthquakes on large gently dipping deformation zones plotted in Figure 4-7 and Figure 4-8. In Figure 5-3 (lower) the normalised slip results are translated to critical radii. For each of the scenarios (present-day and end-glacial conditions) the model giving the largest secondary slip have been selected (cf. Figure 4-8). For each of the scenarios the additional model results are included for comparison.

For the end-glacial scenario, the model giving the largest secondary slip is a BFZ021 model where the rupture is abruptly arrested at a sharp horizontal edge 600 m below the repository horizon (blue plot symbols). In the comparison case the rupture reaches the ground surface (red symbols). See Figure 4-1 for details on the geometry and comments in 4.2.3 on fault-fracture distances. Here the actual distance to the fault rupturing below the repository horizon is smaller for fractures located at 600 m than at 200 m perpendicular distance to the extension of the fault plane.

For the present-day scenario, the model giving the largest slip is a case involving also splays BFZ020 and BFZ099 and with high strength asperities located at repository depth on the otherwise perfectly plane BFZ020 surface (black squares). In the comparison cases the fault surfaces are homogeneous. See Figure 4-1 for details on the geometry.

It is beyond the scope of this overview to go into the complex interaction between main fault rupture, effects of splays and effects of asperities. Details on these issues are found in Fälvh et al. (2019). It is however clear that it takes both seismic moments significantly larger than those of similarly sized earthquakes in Wells-Coppersmith catalogue and effects of different kinds of sharp edges to obtain secondary displacements corresponding to critical radii smaller than about 200 m at the distances considered here. Yet, there are additional margins: The rupture area coincides with the area of the deformation zone on which the earthquake originates, and all target fractures are assumed to be perfectly planar.

The results could be compared with the critical radii suggested at different distances for deformation zones with trace lengths > 5 km in SR-Site (black, stepped line in Figure 5-3, lower). See also Table 5-2 and Figure 2-3.

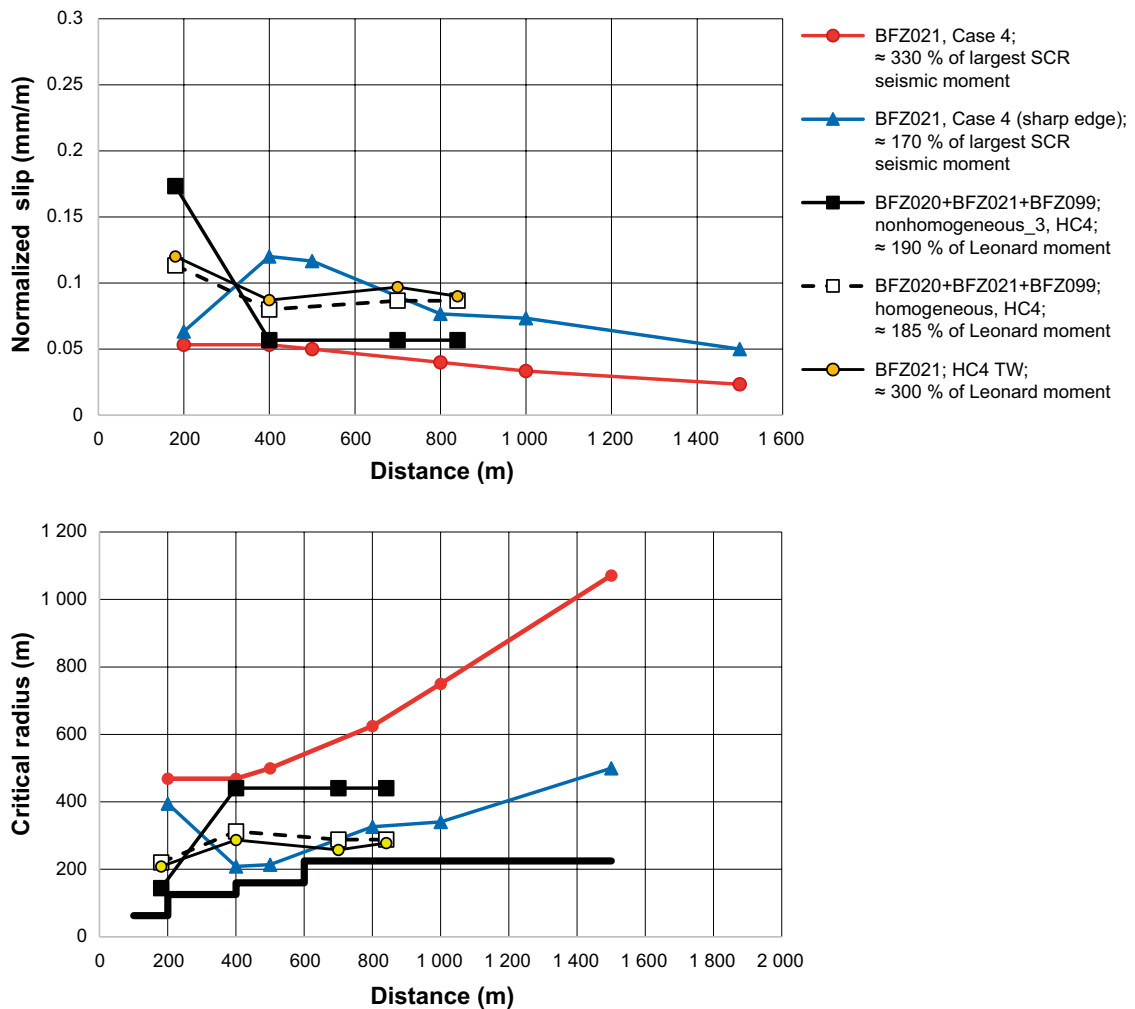


Figure 5-3. Upper: Maximum normalized slip at different distances from large gently dipping deformation zones rupturing under present-day (BFZ200+BFZ201+BFZ099) and end-glacial (BFZ201) stress conditions. The diagram includes the model versions giving the largest secondary displacements under end-glacial conditions (blue triangles) and under present-day conditions (black squares), see Figure 4-8. The results of both these models are influenced by different types of sharp fault edges or sharp fault asperities close to the target fractures. The other model results are included for comparison (see Fälvh et al. (2019) for details on sharp edges and asperities and their impact on secondary slip). Lower: Slip results translated to critical radii. The black bold, stepped, line corresponds to the critical radii suggested in the SR-Site background material (cf. Table 5-2).

Table 5-2 Critical radii at different distances from potential earthquakes zones with trace lengths larger than 5 km as applied in SR-Site.

Distance (m)	Critical radii, horizontal and gently dipping fractures (m)	Critical radii, steeply dipping fractures (m)
100–200	62.5	85
200–400	125	170
400–600	160	215
> 600	225	300

In all these models the largest displacements systematically occur on fractures with the lowest initial stability i.e. gently dipping ones, meaning that the column in Table 5-2 relevant for comparison is the left one. The simulation results suggest that the critical radii could be larger at all distances. This holds true for all cases, also those with secondary displacements influenced by stress concentrations around sharp fault edges or asperities.

5.4 Earthquakes on large, steeply dipping deformation zones

Figure 5-4 (upper) shows maximum normalized slip as function of distance obtained by Fälth and Hökmark (2015) in six different model versions of a present-day earthquake occurring on a steeply dipping deformation zone at Olkiluoto (see Table 4-1) and in two different model versions of a forebulge earthquake occurring on the same zone (BFZ214). All results are found among the results in Figure 4-7.

The strike and dip of the deformation zone are those of the BFZ214 deformation zone in Olkiluoto. The fault area, however, has been extended to cover for hypothetical cases with large undetected faults some distance away from the repository footprint. As for the models of earthquakes occurring on gently dipping zones discussed in the previous section, the in-situ stresses have been defined to make large earthquakes involving the entire fault area a realistic possibility (which in this case means a synthetic strike-slip stress regime at depth). The results are therefore judged to be as relevant for the Forsmark site as for the Olkiluoto site.

The moment magnitudes plot well above the magnitude of the largest SCR earthquake in the Wells-Coppersmith catalogue (Figure 4-7) with seismic moments being between 2.4 and 7.0 times larger than the largest SCR event.

In Figure 5-4 (lower) the results in Figure 5-4 (upper) have been translated to critical radii. The smallest critical radius in Figure 5-4 (lower) 86 m, is related to extreme stress concentrations around an infinitely sharp fault edge (or strip) in a present-day model version (Case 5) with a seismic moment more than four times larger than the maximum Wells-Coppersmith SCR moment. This case should be taken as an extreme test case, analysed to check that the 3DEC results are qualitatively logical and consistent with input assumptions rather than to generate usable results. All other present-day models plot above the SR-Site critical radii lines at all distances.

Careful steps towards a more realistic representation of the strip (Case 4) or towards a less exaggerated magnitude (Case 5re) increase the smallest critical radius to around 200 m. For more details see Fälth and Hökmark (2015). Here it is obvious that even the 200 m critical radius result would be a consequence of significant magnitude overestimates. For models where careful steps towards less exaggerated input assumptions are made (Case 2re, Case 4, Case 5re), the critical radii at the 300 m distance varies between 200 m and 450 m, and between 400 m and 600 m at the 700 m distance. Yet the seismic moments of these 3DEC earthquakes are 3, 5 and 2.5 times larger, respectively, than the seismic moment of the largest SCR earthquake included in the Wells-Coppersmiths catalogue. This is judged to be a sufficient reason to disregard potential effects of earthquakes occurring on any of the large steeply dipping deformation zones such as the Eckarfjärden-, Singö- and Forsmark zones, all located further away than roughly 700 m from the repository footprint (Figure 5-5).

For the forebulge models, all critical radii plot above (or, for the model with a 700 % moment excess, just on) the SR-Site critical radii lines at all distances.

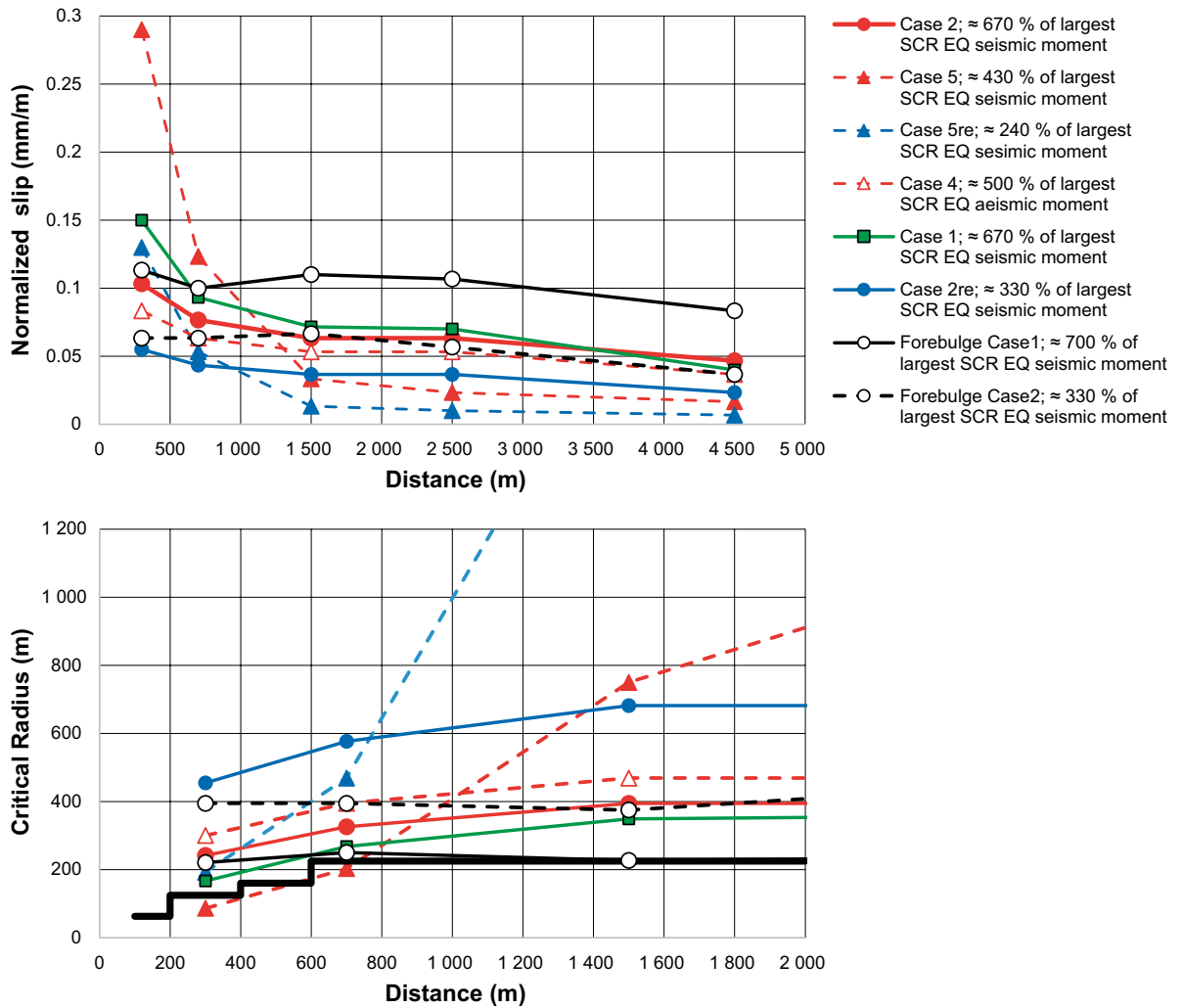


Figure 5-4. Upper: Maximum normalized slip at different distances from large steeply dipping deformation zones rupturing under present-day and forebulge stress conditions. The largest displacement here is obtained in a model with an infinitely sharp stability strip close to the target fractures, cf. Table 4-1. See Fälth and Hökmark (2015) for details on these modelling results. Lower: Normalised slip translated to critical radii. The black bold, stepped, line corresponds to the critical radii suggested in the SR-Site background material (cf. Table 5-2).

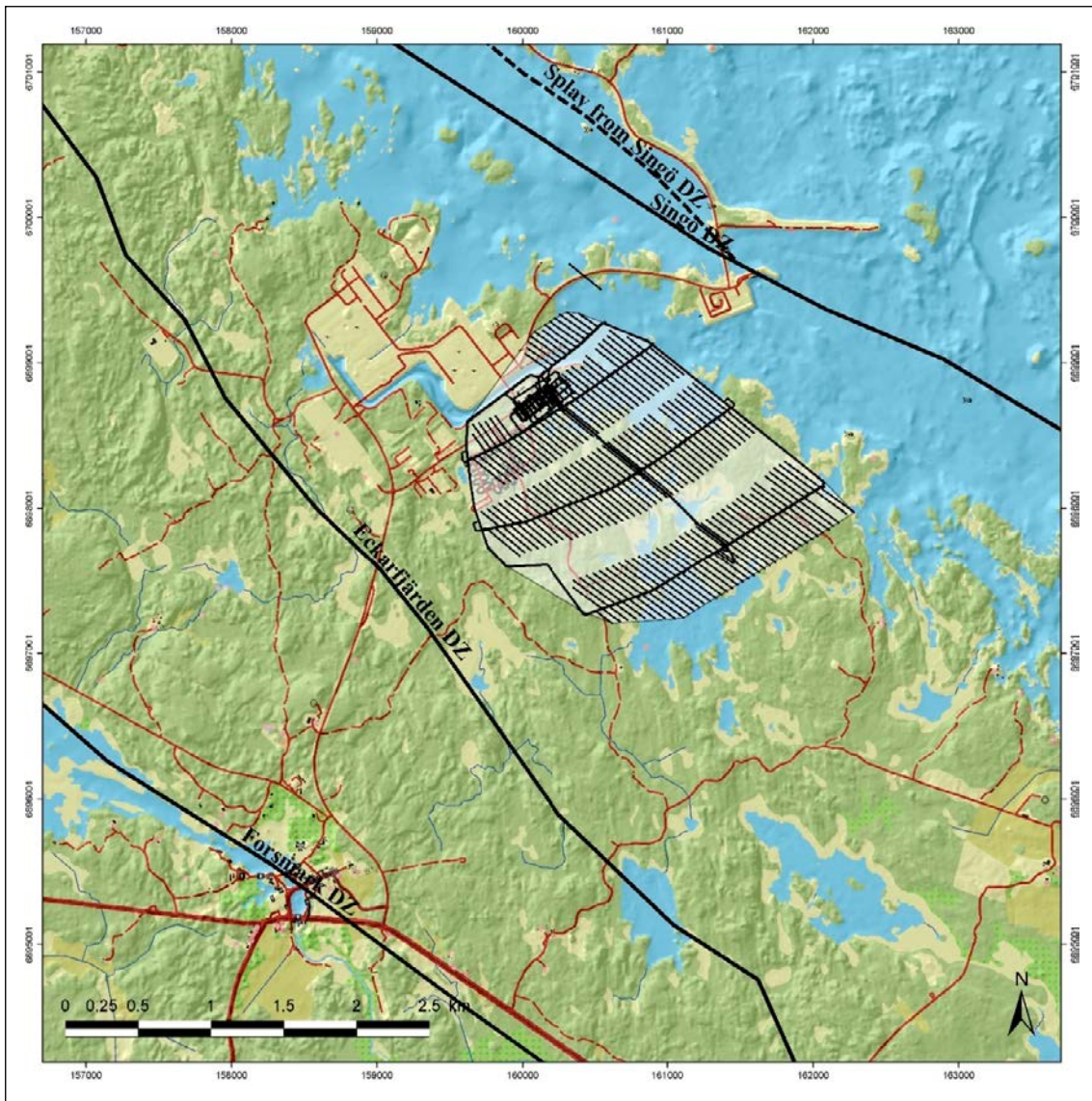


Figure 5-5. The map shows the location of the regional deformation zones in relation to the preliminary repository layout. None of the zones are located closer than about 700 m from any part of the repository.

5.5 Critical radii – steeply dipping fractures

In the reverse faulting stress regime at repository depth and about 1 km below in Forsmark, steeply dipping fractures are effectively clamped by high horizontal stresses and consequently more stable than correspondingly located gently dipping fractures. This is even more pronounced under end-glacial conditions (cf. Figure 3-2, right). This holds, in principle, also for the Olkiluoto site.

As a logical consequence, steeply dipping fracture slip by considerably smaller amounts in all reasonably realistic present-day and end-glacial models included in this overview (i.e. with exception of models with unnatural, infinitely sharp and large asperities, such as the BFZ214 model versions pictured in Figure 4-2. As seen in Figure 4-2, slip on steeply dipping fractures located away from the asperity, is typically less than half the slip on correspondingly located gently dipping fractures).

In the Olkiluoto large scale models of forebulge earthquakes, steeply dipping target fractures slipped more than gently dipping ones (Fälth et al. 2019). This is due to the less pronounced reverse faulting stress regime at repository depth assumed in the Olkiluoto calculations (Fälth and Hökmark 2015). For the Forsmark site, the reverse faulting stress regime at repository depth is sufficiently pronounced that steeply dipping fracture are significantly more stable than gently dipping ones also under forebulge stress conditions, i.e. the reverse faulting stress regime at repository depth will prevail under all load scenarios, see Figure 3-2 (top, right).

In all Forsmark models analysed up to the present day, the maximum slip on steeply dipping fractures was less than 50 % of the slip on gently dipping fractures (Fälth et al. 2016). The relation between critical radii for steeply and gently dipping fractures shown in Figure 2-3 is based in on the conservative assumption that steeply dipping fracture could slip by 75 % of the slip on gently dipping fractures.

As a conclusion, not only the bold stepped critical SR-Site radii lines shown in Figure 5-2, Figure 5-3 and Figure 5-4, relevant for gently dipping fractures, have been shown to hold with good margins for the present-day and end-glacial scenario, but also the SR-Site ratio between critical radii for gently and steeply dipping fractures. Since the reverse faulting stress regime will prevail at repository depth also under forebulge stress conditions that ratio is likely to hold generally. This needs however to be verified (see suggestions under “remaining work” in Chapter 9).

6 Thermally induced earthquakes

In the results overview (cf. Section 4.5) results of simulations of earthquakes assumed to have been triggered by thermally induced stresses 100 years (ZFMA2 in Forsmark), 500 years (BF021 in Olkiluoto) and 1 000 years (ZFMA2 in Forsmark) after deposition are included. The Olkiluoto model is described in Fälth et al. (2019). The Forsmark models are described in an SKB PM in Swedish (Fälth and Hökmark 2013), the essence of which is presented in Appendix A of this report. The main conclusion is that the thermal load on the Forsmark deformation zones will be modest in comparison to the end-glacial load considered in the many ZFMA2 models analysed by Fälth et al. (2016). Figure 6-1 shows critical radii at different distances from the ZFMA2 fault plane.

For Olkiluoto no direct comparisons have been made between end-glacial and thermally induced earthquakes. All secondary slip results of models of Olkiluoto earthquakes occurring during the thermal period are modest, i.e. less than 0.1 mm/m (Fälth et al. 2019).

One interesting comparison is that between an earthquake that is actually triggered by the thermal stresses (i.e. with the hypocentre, HC1, located close to the repository horizon (i.e. within the heated region) and an earthquake that just happens to occur during the heated period (with the hypocentre, HC4, located far below the heated region). The thermally induced earthquake (hypocentre HC1) generates vanishingly small secondary displacements (Figure 4-8), i.e. the effects of the hypocentre location overshadow the effects of the thermal stress disturbance.

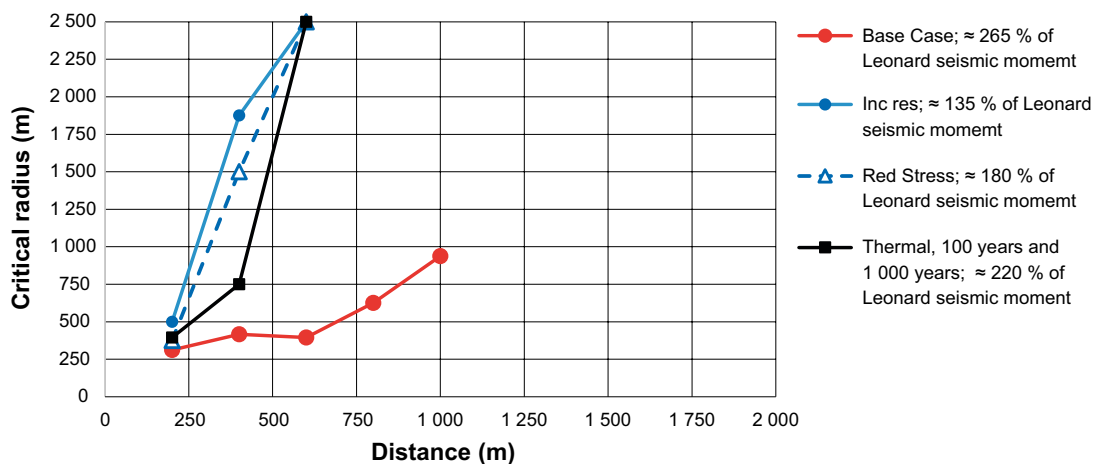


Figure 6-1. Critical radii at different distances from the ZFMA2 fault plane rupturing under thermal load. Some of the corresponding end-glacial results are included for comparison. All results are based on the normalized slip results shown in Figure 4-5. Note that the thermal model results are based on input assumptions (residual strength etc.) that are more in line with those used in the Base Case model than the less exaggerated input assumptions used in the Inc Res model. The relative effects of thermally induced earthquakes would consequently (as described in Appendix A) be smaller than those of a correspondingly modelled end-glacial earthquake. No thermally induced earthquakes with input parameters such as those used in the end-glacial Inc Res case have been modelled.

7 Additional comments on conservatism and margins

7.1 Magnitude exaggeration and edge effects

As pointed out in previous sections, all numerical models producing secondary normalised slip that would correspond to critical radii smaller than about 200 m are based on significantly exaggerated moment magnitude assumptions. From Figure 5-1, Figure 5-3 and Figure 5-3 it appears that it suffices to disregard model results based on the worst combinations of significant magnitude exaggerations, effects of unrealistic hypocentre locations or extremely sharp asperity edges to arrive at critical larger than those applied in the SR-Site layout protocols. This is judged to verify, with good margins, the relevance of the SR-Site critical radii.

Corresponding models with less exaggerated magnitudes, but still plotting among the outliers well above the Stable Continental Region events in the Wells-Coppersmith rupture area – magnitude graphs, give significantly larger critical radii, see Figure 7-1.

The representation of edges and asperities is a complex issue and none of the models including edges and asperities were intended to mimic reality, but rather to check that the model output was logical and consistent with the input assumptions. It is evident, however that it takes different degrees and kinds of input exaggerations to produce secondary displacements corresponding to critical radii smaller than about 200 m at any distance.

In Figure 7-1 different versions of Figure 5-4 (lower) are shown. This particular example regards simulations relevant for large steeply dipping zones with uncertain stress conditions at large depths, i.e. deformation zones like the Singö zone, the Forsmark zone or the Eckarfjärden zone.

In conclusion, there are no model results based on input assumptions realistic enough to justify critical radii smaller than 200 at distances larger than 200 m from any deformation zone. Yet there are additional built-in, but difficult to quantify, magnitude overestimates in all earthquake simulations considered in this document: the assumption that the entire fault area ruptures, cf. Figure 4-1.

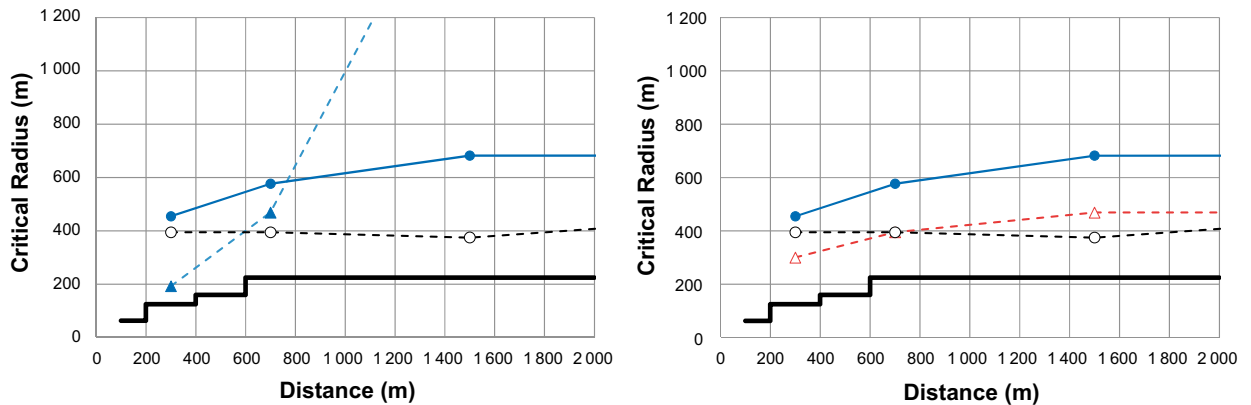


Figure 7-1. Versions of Figure 5-4 (lower). Left: Here results obtained from models with seismic moments larger than 400 % of the largest SCR events in the Wells-Coppersmith catalogue have been excluded. Right: Here results from models with long, optimally oriented and infinitely sharp stability strip edges and models with moment magnitudes larger than 650 % of the largest SCR events in the Wells-Coppersmith catalogue have been excluded.

7.2 Impact of fracture non-planarity

All target fractures modelled within the many studies referred to in this document have been assumed to be perfectly planar and to have mechanical properties based on results of lab scale experiments. It is, however, well known that fracture surfaces are rough or undulating on a wide range of scales (e.g. Candela et al. 2012) and that such deviations from planarity influence the mechanical behaviour of the fractures (e.g. Dieterich and Smith 2009, Marshall and Morris 2012, Ritz and Pollard 2012). Below two examples:

- In a numerical study, Lönnqvist and Hökmark (2015b) found, using the 3DEC code, that waves on optimally oriented fractures in crystalline rock, sized approximately as the target fractures discussed in this document and subjected to similar load changes, would reduce the slip by tens of percent. For schematic represented waves oriented perpendicularly to the shear direction, the slip reduction would be considerable (about 50 %) also for cases with modest angular deviations (11°) from the main orientation of the fracture plane.
- Fälth (2018) found that the average slip on an earthquake fault having self-similar undulations with an amplitude-to-wavelength ratio of 0.005, in accordance with observations, would be about 65 % of the slip on a corresponding planar fault with identical strength properties, and subjected to the same stresses and protocols for rupture initiation and propagation. The simulations performed by Fälth (2018) did not include any target fractures or any site data and are not included in the list of studies in Section 4.1, but the overall results, i.e. the effects of a credible and generally accepted fault surface representation, should be applicable and relevant also for large target fractures.

The typical degree and style of non-planarity among the Forsmark fractures with radii of around 200 m is uncertain. Even slip reductions more modest than those above (35–50 %) would, however, increase the margins significantly.

7.3 Target fracture propagation

No attempts have been made in any of the numerical analyses discussed in this document to include the possible effects of different kinds of inelastic behaviour of the intact rock surrounding the target fractures. Fracture propagation has been suggested as a process that would limit secondary slip (La Pointe et al. 2000). Taking a very schematic and simplistic approach to quantify the impact of propagation, La Pointe et al. (2000) demonstrated the consequences of assuming that slip would only continue as long as propagation at the fracture tips has not been initiated. When and if propagation is initiated no further strain energy would be expended on friction work, i.e. on slip. Taking this schematic model at face value, the maximum slip would be a direct function of the fracture diameter and indicate that fractures with radii less than about 100 m would never slip by more than about 30 mm, cf. Fig. 3-4 in La Pointe et al. (2000).

Even if the above results are based on schematic and simplistic assumptions which tend to overestimate the effects of strain energy being expended on propagation, propagation effects may give some, possibly non-negligible reductions, of the largest fracture shear displacements. Given, however, that the compilation and review made in this document of the many secondary slip results produced for the Forsmark and Olkiluoto sites indicate that even large, potentially critical, fractures slip by modest amounts, for reasonably realistic input assumptions, the propagation effects are not necessarily important.

7.4 Impact of fracture network

In all simulations described here, the individual target fractures have responded to seismic stress disturbances without any influence of other target fractures included in the models. The distance to nearest neighbours, all located with their centres in the same horizontal plane, has systematically been sufficient to allow only for insignificant fracture-fracture mechanical interaction (cf. Fälth and Hökmark 2011). The potential effects of strain energy being expended on slip along surrounding fractures have consequently not been accounted for.

The possibility that slip along nearby differently sized and oriented fractures surrounding the individual target fractures would reduce the slip along the target fractures is addressed in Appendix B of this report. Two cases are considered:

- Target fracture within a DFN based on the Forsmark site model.
- Target fracture within a DFN with uniformly distributed fracture orientations and sizes.

As described in Appendix B, slip along surrounding fractures has the theoretical potential to reduce target fracture slip. This is demonstrated by the results from the uniform DFN case. In the Forsmark DFN case, however, surrounding fractures typically have stability margins sufficient to make this effect insignificant, meaning that the elastic intact rock representation of the rock between the explicitly modelled target fractures should not count as a built-in slip overestimate factor. (In addition, the fractures belonging to 3DEC DFN's are all perfectly planar, meaning that their potential to slip and expend energy on friction work is maximized, which is not conservative).

7.5 Impact of buffer-canister system

All earthquake analyses considered here were performed without accounting for the local effects of the buffer-canister system, i.e. the buffer-canister system was not explicitly included in any of the models.

In the numerical calculations carried out to establish the 50 mm damage criterion, see for instance Børgesson and Hernelind (2010) and Hernelind (2010), a predefined shear displacement along the fracture intersecting the deposition hole has been enforced to the buffer-canister system at a constant speed regardless of the forces that in reality would contribute to control the slip. Looking at results of the type of modelling performed to establish the 50 mm damage criterion it appears that the reaction force mobilized by the buffer-canister system after about 10 mm of slip is larger than the corresponding 3DEC friction force on the fracture segment intersected by the deposition hole (Figure 7-2). This may mean that the reaction forces could give a non-negligible local stabilization of the target fracture and contribute to reduce the calculated secondary slip locally at canister positions in cases with critically large secondary displacements. It should be noted that the friction force in Figure 7-2 and, consequently, the relation between reaction force and friction is approximate and chosen only for illustrative purposes.

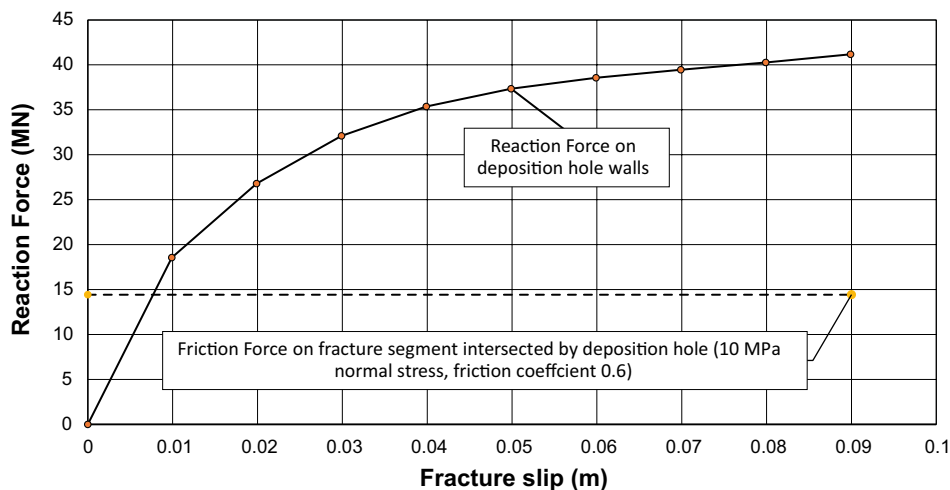


Figure 7-2. Comparison between the reaction force mobilized by the buffer-canister system and the 3DEC fracture friction force on the fracture segment intersected by the deposition hole. The reaction force example shown here is extracted, for the purpose of this memo from modelling work where this type of result is not explicitly reported (Hernelind J 2018, personal communication).

It is difficult to estimate, without access to calculation results from models that explicitly include the increasing reaction force, how large the local slip reduction would be for a fracture that would slip by 50 mm without that reaction force. Obviously, this would depend on a number of factors (normal stress on the target fracture, assumptions made regarding friction etc.). This is an issue that would warrant further studies. (See remaining work).

For the modest induced secondary slip obtained in cases that are not based on exaggerated input assumptions, the reaction force is too small to be of any importance. For the example shown in (Figure 7-2) it takes secondary displacements larger than about 7 or 8 mm for the reaction forces to be larger than the 3DEC friction force on the fracture segment intersected by the deposition hole. For displacements of 30–50 mm, the reaction force, which is not present in the 3DEC models, could potentially be important. It would, however, take some work to find out if this could be used systematically to revise the damage criterion when applying it to 3DEC modelling results. For instance, if a 50 mm modelling result should correspond to, say, 49 mm, 45 mm or 40 mm of shear displacement at positions intersected by canisters.

7.6 Model discretization

The computational burden of the simulations discussed herein constrains the resolution of the discretisation. Results in Fälth et al. (2019) indicate that a finer discretisation might yield slightly less conservative modelling results. The assessment shows that, in specific model setups, the secondary slip using coarse discretisation might be underestimated by up to 25 %. Though the implication Fälth et al. (2019) do not jeopardise the conclusions presented herein, we nevertheless find it necessary to explore this issue further. The advance of powerful cloud computing infrastructures, though still in their infancy, enables a manifold increase in resolution with reasonable computation times. We intend, therefore, to initiate a dedicated study to systematically explore the effect of discretisation upon our modelling results (see chapter 9).

7.7 Elastic properties of the repository host rock

All models covered in this overview have been analysed assuming the host rock to be homogeneous without any spatial variability of the elastic properties. It remains to check how reasonably realistic spatial variability assumptions would impact on the secondary slip results.

7.8 Target fracture pre-slip

All model results presented here regard co-seismic slip. Shear displacements, seismic or aseismic, that would occur during the time period of slow load change leading up to the stress conditions prevailing at the time of fault rupture are not included. This is a question related to the validity of the canister damage criterion, i.e. if the criterion, as implicitly assumed here, regards just one pulse of fast deformation, and not also a potential sequence of preceding minor and slow deformations of the buffer/canister system.

8 Discussion and conclusions

8.1 General

In this study, the main issue has been to compile and evaluate the results of the numerous simulations of earthquakes generating distributed faulting, “induced secondary displacements”, around the rupturing main fault performed after the publication of the SR-Site safety assessment. As in the SR-Site modelling work described in Fälth et al. (2010), the continued modelling has been accomplished using the dynamic logic of the 3DEC code. The compilation of the results, i.e. the largest induced secondary shear displacements found at the different distances from the rupturing fault considered in the different simulations, is found in Chapter 4.

In the continued 3DEC modelling it has been possible to take advantage of the gradually increasing computational capacity, allowing for larger and more detailed models to be analysed, for instance models with arbitrarily oriented deformation zones, e.g. deformation zones oriented according to site models. One important step has been to increase the overall confidence in the modelling method by verifying the capacity of the 3DEC dynamic logic to generate and transmit stress waves properly. This has been accomplished using analytical solutions and established seismological tools as benchmarks (Fälth et al. 2015). The benchmark model was also used to clarify the minimum frequency, and the associated requirements on model discretization, necessary for capturing dynamically induced slip along large host rock fractures correctly (Fälth and Hökmark 2015). Note, however, the comments on the discretization issue in Section 7.6.

One issue addressed herein is the stability of the deterministic, modestly sized, almost vertical deformation zones located in the near vicinity of the Forsmark repository footprint (Section 3.2.3). In the SR-Site safety assessment some of those were, based on estimates made by Fälth et al. (2010), characterized as potentially unstable. This potential instability would however be a concern at depths far below the repository horizon. At repository depth and about 2 km below, the stability (in terms of *CFS*) is judged to be high enough (Figure 3-2, right) to suppress propagation of a rupture initiated at depth, in the unlikely case that these zones should extend deep enough for large, sufficiently unstable fault segments to exist. Up to the present day no simulations of earthquakes on any of the deterministic, vertical and modestly sized zones in the near vicinity of the Forsmark repository footprint have been performed, i.e. only ZFMA2 models have been considered. Possibly one or two simulations could be performed to verify or demonstrate that none of the local vertical zones in Forsmark would slip sufficiently for secondary effects to be of any importance for the seismic risk and the repository layout. This should be done for forebulge stress conditions, i.e. during the period of minimum stability for these zones. See comments in Section 3.2.4. This issue is addressed under “remaining work” below.

The overview material presented in the “Results overview” section (Chapter 4) is based on 43 different modelling cases. About 8 600 of the differently oriented and located target fractures included in these models are represented here (however, only those slipping most at the different distances considered in the different models are explicitly presented, see Figure 4-5 and Figure 4-8). Fractures located in the hanging wall of ZFMA2 and fractures at distances where the calculated secondary displacements were found to be vanishingly small for all orientations and all positions are not represented. The results are separated into two categories: one for earthquakes occurring on deterministic, modestly sized deformation zones located within or in the near vicinity of the Olkiluoto and Forsmark footprints (for Forsmark, according to the above, only earthquakes on the gently dipping ZFMA2 are included) and one for earthquakes occurring on large deformation zones of hypothetical extension. For the large earthquakes, the stress-fields below repository depth are schematically defined to make large earthquakes a realistic possibility, i.e. synthetic reverse stress regimes for models including gently dipping faults and synthetic strike-slip stress regimes for models including steeply dipping faults. This means that the results of the large earthquake simulations are, in principle, as relevant for the Forsmark site as for the Olkiluoto site. For earthquakes on modestly sized deterministic deformation zones (where the importance of local stress conditions is, relatively seen, larger) only the results based on the Forsmark site model are judged to be fully relevant for Forsmark (even if the results of the Olkiluoto site models, with very modest secondary displacements at all distances, are in general support of the evaluation of the Forsmark model results).

8.2 Critical radii at different distances from deformation zones with trace lengths between 3 000 m and 5 000 m.

Out of the in total around 5 600 fractures modelled on the footwall side of the ZFMA2 zone (including all distances, positions and orientations considered in the different models), eleven slipped more than 0.10 mm/m (cf. Fälth et al. 2016) and none more than 0.12 mm/m (cf. Figure 4-5).

All target fracture slip results exceeding 0.1 mm/m are found in a model (Alt Hypo Case) with a seismic moment about 2.5 times larger than typical seismic moments of earthquakes of similar rupture areas and with a maximum fault slip at least twice as large as that of any of the earthquakes of similar magnitude included in the Wells Coppersmith catalogue (Figure 4-6.). In addition, in this particular model, the hypocentre was located in one of the lower fault corners which, combined with a rupture model that allowed for unlimited growth of the stress peak travelling ahead of the rupture front (Fälth et al. 2016), has contributed to exaggerate the secondary slip sufficiently for the Alt Hypo results to be disregarded. Disregarding these particular results would practically eliminate the respect distance problem (cf. Figure 5-1, lower).

Out of 120 footwall side fractures included in one model (Inc Res Case) that would represent a careful step towards slightly less exaggerated input assumptions (but still with margins to outliers in the Wells-Coppersmith catalogue, see Figure 4-6.) none slipped by more than 0.05 mm/m. This corresponds to 15 mm of slip on 300 m diameter target fractures and critical radii of 500 m at the closest distance considered (200 m). At larger distances the calculated slip is vanishingly small.

Given that the ZFMA2 zone is the one among the modestly sized deformation zones within or in the near vicinity of the repository footprint that, with good margins, has the lowest stability and the one with the highest potential for large stress drops at relevant depths, the ZFMA2 model results should count as bounding estimates of the secondary slip that could be induced as result of earthquakes occurring on any of these deformation zones, including the steeply dipping zones. It is a matter of judgement which of the ZFMA2 models (if any) that is based on input assumptions sufficiently exaggerated for the results to qualify as safe upper bound estimates of secondary host rock fracture displacements.

The main conclusion of the above is that the critical radii at different distances from zones of trace lengths between 3 000 m and 5 000 m established in SR-Site (Figure 2-3) are, with good margins, verified as safe lower bounds (Figure 5-1, lower).

The next conclusion is that all simulations that are not based on obviously unrealistically exaggerated input assumptions give very modest secondary displacements at all distances, corresponding to much larger critical radii than the SR-Site radii. This opens for a general reconsideration of the respect distance issue. Some work remains, however, to explore and clarify this.

8.3 Critical radii at different distances from deformation zones with trace lengths larger than 5 000 m

8.3.1 Steeply dipping deformation zones

For earthquakes occurring on large steeply dipping zones located some distance away from the repository footprint (such as, for instance, the Forsmark zone, the Eckarfjärden zone and the Singö zone), the results obtained from different versions of the Olkiluoto BFZ214 model analysed by Fälth and Hökmark (2015) are relevant enough for bounding estimates of secondary displacements within the Forsmark repository footprint to be made. Note that the stress field at depth, where the actual stresses are uncertain in Olkiluoto as well as in Forsmark, was defined to maximize the instability in order to make large earthquakes a reasonably realistic possibility in these models.

The seismic moments of all earthquakes modelled on the BFZ214 deformation zone at Olkiluoto are between 240 and 700 % larger than the seismic moment of all Stable Continental Region (SCR) earthquakes included in the Wells-Coppersmith catalogue (cf. Figure 5-4). The largest secondary displacement is found in a model that does not only have an unrealistically high large seismic moment but also an extremely sharp fault asperity positioned optimally to generate stress concentrations

close to the target fractures (cf. Table 4-1). Considering all model results, regardless of magnitude exaggerations and far-fetched edge effects, the critical radii at distances larger than 700 m would be 200 m and more (Figure 5-4, lower). Disregarding the most unrealistic scenarios, for instance those with seismic moments > 400 % of the largest SCR moment in the Wells-Coppersmith catalogue, would eliminate the risk related to earthquakes (present-day and forebulge events) occurring on, for instance, the Singö, the Eckarfjärden or the Forsmark zones, see Figure 5-5 and Figure 7-1 (left).

The main conclusion of the above is that the critical radii at different distances from zones with lengths larger than 5 000 m established in SR-Site (Figure 2-3) are, with good margins, verified as safe lower bounds.

8.3.2 Gently dipping deformation zones

There is no documentation of large, gently dipping deformation zones in the vicinity of the Forsmark repository footprint. There is, however, still the possibility that large, gently dipping zones, in the worst case localized below the repository footprint, have remained undetected. The results obtained for simulations of earthquakes occurring on large gently dipping deformation zones (powered by synthetic reverse faulting stress fields), in studies related to the Olkiluoto site (cf. Figure 4-9), are judged to be relevant also for the Forsmark site. The results in Figure 5-3 show that the SR-Site critical radii are, with good margins, relevant and that it takes extreme input assumptions (magnitude exaggerations and optimally located unrealistically sharp fault inhomogeneities) to produce secondary displacements that are even close to those corresponding to the SR-Site radii.

8.4 Concluding remarks

The general conclusion of the observations and comments made here regarding the target fracture results obtained in the many earthquake simulations performed after SR-site is that the SR-Site critical radii shown in Figure 2-3 are, with very good margins indeed, still relevant.

In cases where careful steps towards less exaggerated input assumptions were taken, the resulting secondary slips are significantly reduced. No such model (local or large scale) resulted in critical radii smaller than 200 m at any distance.

The largest displacements and the smallest radii are systematically related to the fractures with the lowest initial stability, i.e. to gently dipping fractures. Figure 3-2 (right) shows that this is the case for present-day, end-glacial and forebulge conditions at repository depth in Forsmark. (For the Olkiluoto site, however, the reverse stress regime at repository depth is less pronounced, meaning that steeply dipping fractures could be close to instability during the forebulge period).

Table 8-1 shows, again, the SR-Site critical radii for gently dipping fractures (which have, as stated above, been shown here to hold with good margins). The table does also show corresponding updated critical radii, based on results obtained in this overview from models in which careful steps towards reasonably realistic input assumptions were taken (for instance models without unrealistically sharp asperities and models without extreme magnitude exaggerations)

Table 8-1. Critical radii.

Fault- fracture distance (m)	Zones with lengths 3 000 m – 5 000 m		Zones with lengths > 5 000 m	
	SR-Site critical radii (m)	Critical radii suggested based on new results	SR-Site critical radii (m)	Critical radii suggested based on new results
100–200	75	115	62.5	75
200–400	150	230	125	150
400–600	225	350	160	225
> 600	225	350	225	250

Figure 8-1 shows different ways of evaluating seismic moment exaggerations. Even moments corresponding to 150 % of the Leonard (2010) regression moment appear to be reasonable upper bounds for all SCR earthquake seismic moments (with the exception of small deep-seated, high stress drop, events, see Figure 1-3b and associated text).

Figure 8-2 shows the suggested updated critical radii along with SR-Site critical radii and with the calculation results relevant for establishing these radii. As in Table 8-1, the critical radii regard gently dipping fractures. All Forsmark modelling results (cf. Fälvh et al. 2016) verify, with good margins, the SR-Site difference between slip on steeply dipping and gently dipping fractures (Figure 2-3), cf. discussion in Section 5.5.

The yellow labels in Figure 8-2 point to the few modelling results that need to be disregarded to defend the updated critical radii suggested here. It is, however, a matter of judgement to decide on the degree of exaggerations (e.g. seismic moment exaggerations) that actually would be required to defend increased critical radii.

On the local scale, for instance, it would be sufficient to disregard models with seismic moments exceeding 250 % of the Leonard seismic moment and models with unrealistic growth of stress peaks during rupture propagation to practically eliminate the problem of secondary slip (Figure 8-2a). Note that even the two blue lines in Figure 8-2(a) correspond to synthetic earthquakes that plot among the outliers in Figure 4-6. To make more general statements on the local scale issue it would, however, be necessary to analyse also effects on earthquakes on steeply dipping local zones under forebulge stress conditions (see Section 3.2.4).

For large scale earthquakes, there are no reasonably realistic calculation results that would point to critical radii smaller than 250 at distances larger than 600 m (Figure 8-2(b) and (c)).

All of the above suggest that the problem of seismically induced secondary displacements in the repository host rock may have been considerably overestimated in SR-Site and that there are good possibilities to improve the degree of tunnel capacity utilization in general and to reconsider whether or not the steeply dipping local zones require any respect distances in particular.

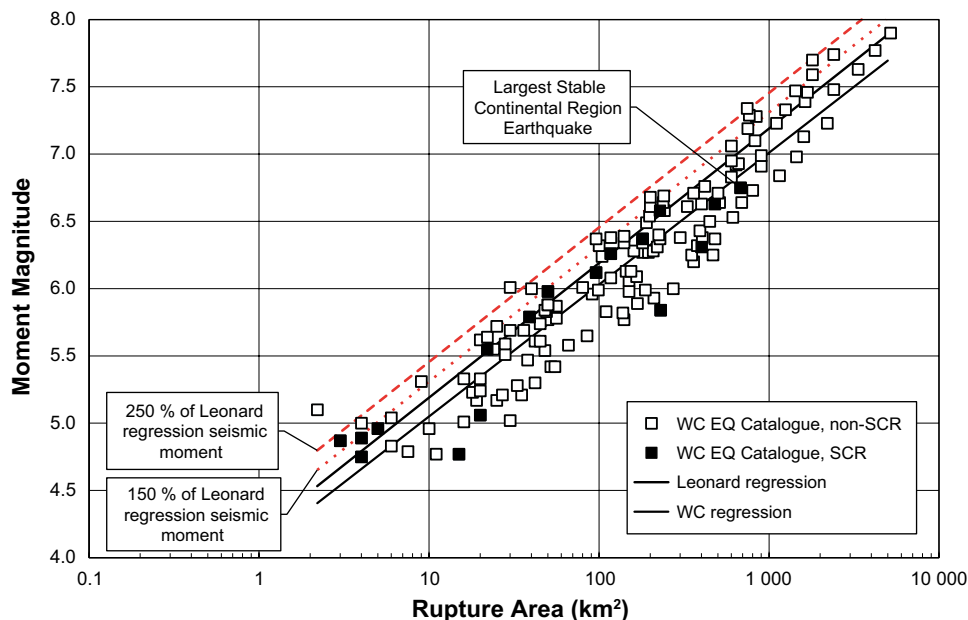


Figure 8-1. Ways of evaluating magnitude exaggeration. For synthetic earthquakes with the largest rupture areas (around 700 km², cf. Figure 4-7) the seismic moments can be compared with the moment of the largest SCR (Stable Continental Region) earthquake included in the Wells and Coppersmith (1994) database. For all other synthetic earthquakes, the seismic moment is compared with the Leonard (2010) regression moment of earthquakes with similarly sized rupture areas. The dashed red example lines correspond to seismic moments that are 150 % and 250 %, respectively of the Leonard regression moment.

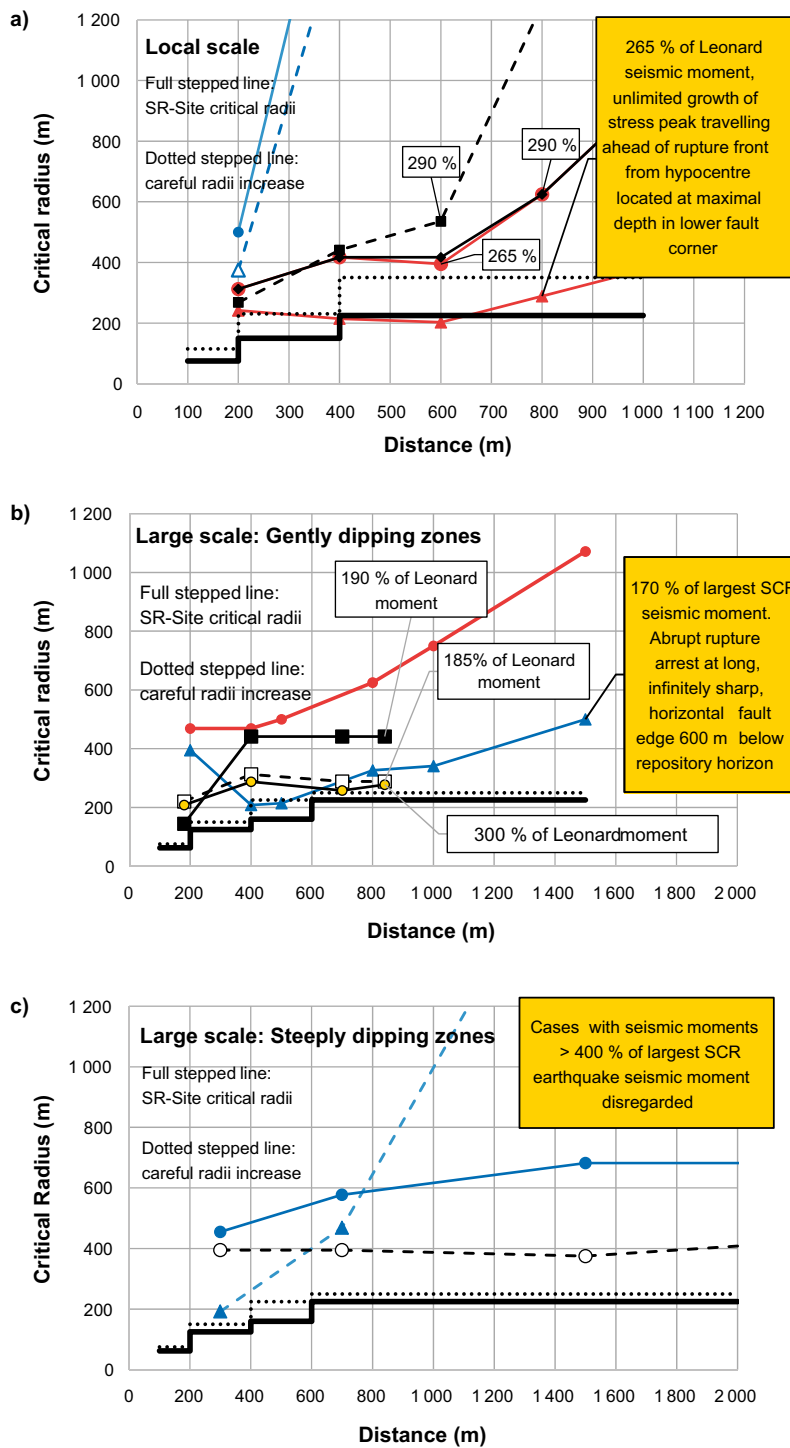


Figure 8-2. SR-Site critical radii (full stepped lines) and potentially possible radii updates (dotted stepped lines). a: local scale (ZFMA2) earthquakes. b and c: large scale earthquakes. See Figure 5-1, Figure 5-3 and Figure 5-4, for identification and details of the modelling cases used for comparison here.

One should note that, regardless of the input assumptions discussed above, there are additional slip overestimates related to the uncertain rupture area overestimate, see Figure 4-1 and associated text.

However, to establish what the possibilities are to finally devise defensible, updated layout rules, more work is needed, as outlined in the following section.

9 Remaining work

Table 9-1 and Table 9-2 below are brief summaries of work that has already been performed and of work planned to be performed in the future. Some of the planned future work is essentially modelling work of the same type as the modelling work described in previous sections of this overview (Table 9-1). Other efforts of potential importance for the evaluation of the seismic risk for the Forsmark repository are listed in Table 9-2.

One important issue is to check the sensitivity of the results to reasonable local variations in elastic moduli, local stress variations, fracture properties etc. (Table 9-1).

Another important issue would be to rerun the ZFMA2 Inc Res model with additional fracture sets in order to ensure that the largest possible secondary displacements are indeed captured (Table 9-1).

Once the general confidence in the validity of the results presented in this overview has been strengthened, earthquake simulations on one of the stable, steeply dipping local zones, should be performed, using the rupture model applied in a reference case, e.g. the ZFMA2 Inc Res case. The powering stresses should conservatively be those of the forebulge period, i.e. when the stability of these zones should be at minimum (Table 9-1).

Some of the aspects that are needed to address have little connection with the dynamic numerical modelling. The presence of the buffer/canister system (see Section 7.5), for instance, is an issue that could be addressed in static models (Table 9-2). The result of that modelling would not impact on the relevance of any of the results presented here, but possibly indicate that the effective damage criterion could be a little more than 50 mm, strengthening further the safety margins.

Table 9-1. Performed and planned modelling of seismically induced secondary slip on repository host rock fractures.

Aspect	Reference/plans	Comment
Bechmarks	Fälth et al. (2015)	The suitability of the 3DEC code for the type of problems relevant for KBS-3 verified.
The effect of model resolution (discretisation) on model results	Fälth et al. (2019) Additional work planned	Systematically evaluate the effect of resolution of fracture and zone undulation upon the induced slip magnitudes.
Variability of stress field and rock mass properties (i.e., elastic moduli) in repository host rock	Planned	Check whether or not local stress, rock property and fracture property variations would impact the amount of slip in a non-negligible way.
Coverage of target fracture orientations	Planned	A possible reference case, i.e., the Inc Res version of an end-glacial EQ on ZFMA2, should be rerun with additional target fracture sets. In particular it should be ensured that optimally oriented fractures are included, i.e., also hypothetical sets with maximized initial instability.
Stability of local steeply dipping faults	Planned	Check/verify that the stability of the local steeply dipping faults (Figure 3-2, right) is sufficient to justify disregarding these zones as potential risks of relevance to safety assessment and layout decisions (see following point).
Forebulge issue	Planned	Modell forebulge EQ on steeply dipping zones, e.g. on ZFMWNNW0017 and ZFMWNNW123 (See Section 3.2.4). For a fair evaluation and comparison, the input parameters should be those used for an end-glacial reference case, e.g., the Inc Res version of the ZFMA2 model.
Large EQs on large faults at some distance outside the repository footprint, i.e., Singö, Eckarö etc., and possibly on large undetected subhorizontal zones below the repository footprint	Fälth and Hökmark (2015); Fälth et al. (2019) No plans specific for this issue.	Because of the generic and conservativ stress field assumptions, the secondary slip results from these Olkiuoto models are equally relevant for Forsmark.

Aspect	Reference/plans	Comment
Branching faults	Fälth et al. (2019) No plans specific for this issue	See previous point and Figure 4-9 with associated text.
Undulating target fractures	Lönnqvist and Hökmark (2015); Fälth (2018) Additional work is planned	To further address conservativeness and potentially further relax performance requirements.
Undulating faults and representation of fault edges	Fälth et al. (2017); Fälth (2018) Additional work planned.	Apply to case relevant for the Forsmak site (e.g. reasonably realistic end-glacial EQ on ZFMA2).
Ice variations	Planned	It may be needed to check/verify that the general conclusions presented herein also hold for new/alternative ice and earth models.
Thermal load	Appendix A, this report No plans specific for this issue	See comments in Chapter 6.
Present-day earthquakes (induced by, for instance, tunnel excavation)	Appendix A, this report No plans specific for this issue.	Present-day earthquakes would be powered by significantly lower stresses than those powering end-glacial EQs (and thermally induced EQs, see Appendix A) and, consequently, produce even smaller secondary slip movements than those obtained in the Inc Res ZFMA2 model.
Target fractures located closer to rupturing fault	Planned	Target fractures 100-200 m from ZFMA2 damaged zone (e.g. Inc Res version) and, possibly, fractures intersecting the zone.
DFN surrounding target fractures	Appendix B, this report No plans specific for this issue	Potential additional margins are small and uncertain.

Table 9-2. Additional issues.

Aspect	Reference/plans	Comment
Repository as plane of weakness	Lönnqvist et al. (2010) No plans specific for this issue	Has been concluded not to be an issue.
Probabilistic handling of modelling results	Planned	To provide PSHA with information for front-end analyses. The task consists of extracting relevant modelling results so that they may be expressed as distributions.
Modelling the end-glacial Burträsk earthquakes	Planned	Possibly increase confidence in conjecture that end-glacial faulting effectively is an issue relevant only for northern Fennoscandia.
Alternative conceptualisation	Planned and ongoing	To increase confidence in the results presented herein, a representative modelling case (e.g. ZFMA2, Inc Res version) will be modelled using a conceptually different modelling tool.
Device more relevant handling of the question of multiple earthquakes occurring over long periods of time	Planned	The handling of repeated seismic events in the SR-Site process report was schematic, simplistic and overly conservative in terms of cumulative slip on target fractures.
Bentonite/canister/rock interaction	Planned	To evaluate how much larger than 50 mm the maximum calculated target fracture slip must be in order to enforce 50 mm of slip in correspondingly located canister positions.
Fracture propagation	La Pointe et al. (2000) No plans specific for this issue	Fracture propagation would reduce the amount of strain energy that could be expended on fracture slip. An uncertain margin exists, but no plans to quantify.
Investigate possibility to apply conventional earthquake engineering modelling approaches	Planned if required by PSHA	Models without explicit representation of seismic source.

References

SKB's (Svensk Kärnbränslehantering AB) publications can be found at www.skb.com/publications. SKBdoc documents will be submitted upon request to document@skb.se.

Andrews D J, 2004. Rupture models with dynamically determined breakdown displacement. *Bulletin of the Seismological Society of America* 94, 769–775.

Aydan Ö, Ohta Y, Geniş M, Tokashiki N, Ohkubo K, 2010. Response and stability of underground structures in rock mass during earthquakes. *Rock Mechanics and Rock Engineering* 43, 857–875.

Baker C, Hildyard M, Christianson, M, 2004a. Shear displacement on fractures due to seismic movements, Phase II. In Munier R, Hökmark H. *Respect distances. Rationale and means of computation.* SKB R-04-17, Svensk Kärnbränslehantering AB, Appendix 2a.

Baker C, Hildyard M, Pettitt, W, 2004b. Velocity-time histories resulting from a magnitude 6 earthquake in the vicinity of a sub-surface repository. In Munier R, Hökmark H. *Respect distances. Rationale and means of computation.* SKB R-04-17, Svensk Kärnbränslehantering AB, Appendix 1b.

Barton N, Chrystanthakis P, 1989. Distinct element modelling of the influence of glaciation and deglaciation on the behaviour of a faulted rock mass. SKB AR 89-19, Svensk Kärnbränslehantering AB.

Bizzarri A, 2010. How to promote earthquake ruptures: different nucleation strategies in a dynamic model with slip-weakening friction. *Bulletin of the Seismological Society of America* 100, 923–940.

Brady B H G, Brown E T, 1995. *Rock mechanics for underground mining.* 2nd ed. London: Chapman & Hall.

Byerlee J D, 1978. Friction of rocks. In Byerlee J D, Wyss M (eds). *Rock friction and earthquake prediction.* Basel: Birkhäuser, 615–626.

Bäckblom G, Munier R, 2002. Effects of earthquakes on the deep repository for spent fuel in Sweden based on case studies and preliminary model results. SKB TR-02-24, Svensk Kärnbränslehantering AB.

Bäckblom G, Stanfors R (eds), 1989. *Interdisciplinary study of post-glacial faulting in the Lansjärv area, Northern Sweden, 1986–1988.* SKB TR 89-31, Svensk Kärnbränslehantering AB.

Bäckblom G, Munier R, Hökmark H, 2004. Earthquake data and modelling to study the effects of future earthquakes on a final repository of spent nuclear fuel in Sweden. *Proceedings of the 13th World Conference on Earthquake Engineering, Vancouver, Canada, 1–6 August 2004, Paper 3238.*

Börgesson L, Hernelind J, 2006. Earthquake induced rock shear through a deposition hole. Influence of shear plane inclination and location as well as buffer properties on the damage caused to the canister. SKB TR-06-43, Svensk Kärnbränslehantering AB.

Börgesson L, Hernelind J, 2010. Earthquake induced rock shear through a deposition hole. Modelling of three model tests scaled 1:10. Verification of the bentonite material model and the calculation technique. SKB TR-10-33, Svensk Kärnbränslehantering AB.

Candela T, Renard F, Klinger Y, Mair K, Schmittbuhl J, Brodsky E E, 2012. Roughness of fault surfaces over nine decades of length scales. *Journal of Geophysical Research: Solid Earth* 117. doi:10.1029/2011jb009041

Christianson, M, 2004. Shear displacement on fractures due to seismic movements. In Munier R, Hökmark H. *Respect distances. Rationale and means of computation.* SKB R-04-17, Svensk Kärnbränslehantering AB, Appendix 1a.

Coppersmith K J, Youngs R R, 2000. Data needs for probabilistic fault displacement hazard analysis. *Journal of Geodynamics* 29, 329–343.

Coppersmith K J, Jenni K E, Perman R C, Youngs R R, 2009. Formal expert assessment in probabilistic seismic and volcanic hazard analysis. In Connor C B, Chapman N A, Connor L J (eds). *Volcanic and tectonic hazard assessment for nuclear facilities.* Cambridge: Cambridge University Press, 593–611.

- Cruz-Atienza V M, Husker A, Legrand D, Caballero E, Kostoglodov V, 2015.** Nonvolcanic tremor locations and mechanisms in Guerrero, Mexico, from energy-based and particle motion polarization analysis. *Journal of Geophysical Research: Solid Earth* 120, 275–289.
- Cundall P A, 1971.** A computer model for simulating progressive, large scale movement in blocky rock systems. In *Proceedings of the International Symposium on Rock Mechanics, Nancy, France, 4–6 October 1971*. International Society for Rock Mechanics.
- Dieterich J H, Smith D E, 2009.** Nonplanar faults: Mechanics of slip and off-fault damage. In Ben-Zion Y, Sammis C (eds). *Mechanics, structure and evolution of fault zones*. Basel: Birkhäuser, 1799–1815.
- Dowding C H, Rozen A, 1978.** Damage to rock tunnels from earthquake shaking. *Journal of the Geotechnical Engineering Division* 104, 175–191.
- Du Rietz T, 1937.** Recenta förkastningar eller sprickbildningar i Västerbottensfjällen. *Geologiska Föreningens i Stockholm Förhandlingar* 59, 112–114. (In Swedish.)
- Ericsson L O, Stanfors R, 1993.** Supplementary investigations of postglacial faulting in the Lansjärv area, northern Sweden, 1990–1992. SKB AR 93-18, Svensk Kärnbränslehantering AB.
- Eshelby J D, 1957.** The determination of the elastic field of an ellipsoidal inclusion, and related problems. *Proceedings of the Royal Society A* 241. doi: 10.1098/rspa.1957.0133
- Fox A, La Pointe P, Hermanson J, Öhman J, 2007.** Statistical geological discrete fracture network model. Forsmark modelling stage 2.2, SKB R-07-46, Svensk Kärnbränslehantering AB.
- Fälth B, 2018.** Simulating earthquake rupture and near-fault fracture response. PhD thesis. Uppsala University.
- Fälth B, Hökmark H, 2006a.** Seismically induced slip on rock fractures. Results from dynamic discrete fracture modeling. SKB R-06-48, Svensk Kärnbränslehantering AB.
- Fälth B, Hökmark H, 2006b.** Mechanical and thermo-mechanical discrete fracture near-field analyses based on preliminary data from the Forsmark, Simpevarp and Laxemar sites, SKB R-06-89, Svensk Kärnbränslehantering AB.
- Fälth B, Hökmark H, 2011.** Modelling end-glacial earthquakes at Olkiluoto. Posiva Working Report 2011-13, Posiva Oy, Finland.
- Fälth B, Hökmark H, 2012.** Modelling end-glacial earthquakes at Olkiluoto. Expansion of the 2010 study. Posiva Working Report 2012-08, Posiva Oy, Finland.
- Fälth B, Hökmark H, 2013.** Termiskt inducerade skalv. SKBdoc 1403906 ver 1.0, Svensk Kärnbränslehantering AB. (In Swedish.)
- Fälth B, Hökmark H, 2015.** Effects of hypothetical large earthquakes on repository host rock fractures. Posiva Working Report, 2015-18, Posiva Oy, Finland.
- Fälth B, Hökmark H, Munier R, 2010.** Effects of large earthquakes on a KBS-3 repository. Evaluation of modelling results and their implications for layout and design. SKB TR-08-11, Svensk Kärnbränslehantering AB.
- Fälth B, Hökmark H, Lund B, Mai P M, Roberts R, Munier R, 2015.** Simulating earthquake rupture and off-fault fracture response: application to the safety assessment of the Swedish nuclear waste repository. *Bulletin of the Seismological Society of America* 105, 134–151.
- Fälth B, Hökmark H, Lund B, 2016.** Simulation of co-seismic secondary fracture displacements for different earthquake rupture scenarios at the proposed nuclear waste repository site in Forsmark. *International Journal of Rock Mechanics and Mining Sciences* 84, 142–158.
- Fälth B, Lund B, Hökmark H, 2017.** Simulation of co-seismic off-fault stress effects: influence of fault roughness and pore pressure coupling. In *Proceedings of American Geophysical Union Fall Meeting 2017, New Orleans, 11–15 December 2017*, abstract #S43B-0872.
- Fälth B, Lönnqvist M, Hökmark H, 2019.** Co-seismic secondary fracture displacements under different stress conditions. Posiva Working Report 2019-10, Posiva Oy, Finland.

- Gephart J W, Forsyth D W, 1984.** An improved method for determining the regional stress tensor using earthquake focal mechanism data: application to the San Fernando earthquake sequence. *Journal of Geophysical Research: Solid Earth* 89, 9305–9320.
- Glamheden R, Fredriksson A, Röshoff K, Karlsson J, Hakami H, Christiansson R, 2007.** Rock Mechanics Forsmark. Site descriptive modelling Forsmark stage 2.2. SKB R-07-31, Svensk Kärnbränslehantering AB.
- Hanks T C, Kanamori H, 1979.** A moment magnitude scale. *Journal of Geophysical Research: Solid Earth* 84, 2348–2350.
- Harris R A, 1998.** Introduction to special section; stress triggers, stress shadows, and implications for seismic hazard. *Journal of Geophysical Research: Solid Earth* 103, 24347–24358.
- Henkel L, Hult K, Eriksson L, Johansson L, 1983.** Neotectonics in northern Sweden – geophysical investigations. SKBF/KBS TR 83-57, Svensk Kärnbränslehantering AB.
- Hernelind J, 2010.** Modelling and analysis of canister and buffer for earthquake induced rock shear and glacial load. SKB TR-10-34, Svensk Kärnbränslehantering AB.
- Hildyard M W, Daehnke A, Cundall P A, 1995.** WAVE: a computer program for investigating elastodynamic issues in mining. In Daemen J J K, Schultz R A (eds). *Proceedings of 35th U.S. Symposium on Rock Mechanics*, University of Nevada, Reno, 5–7 June 1995. A. A. Balkema.
- Hökmark H, Fälth B, 2014.** Approach to assessing the stability of Olkiluoto deformation zones during a glacial cycle. Posiva Working Report 2013-37, Posiva Oy, Finland.
- Hökmark H, Lönnqvist M, Fälth B, 2010.** THM-issues in repository rock. Thermal, mechanical, thermo-mechanical and hydro-mechanical evolution of the rock at the Forsmark and Laxemar sites. SKB TR-10-23, Svensk Kärnbränslehantering AB.
- Ida Y, 1972.** Cohesive force across the tip of a longitudinal-shear crack and Griffith's specific surface energy. *Journal of Geophysical Research* 77, 3796–3805.
- Itasca, 1997.** Flac3D, Fast Lagrangian Analysis of Continua in 3 Dimensions. Version 2.0. Minneapolis, MN: Itasca Consulting Group, Inc.
- Itasca, 2013.** 3DEC, 3 Dimensional Distinct Element Code, Users manual. Version: 4.1. Minneapolis, MN: Itasca Consulting Group, Inc.
- Jaeger J C, Cook N G W, 1979.** *Fundamentals of rock mechanics*. 3rd ed. London: Chapman and Hall.
- Johnston A C, 1987.** Suppression of earthquakes by large continental ice sheets. *Nature* 303, 467–469.
- Krinitzky E L, Gould J P, Edinger P H, 1993.** *Fundamentals of earthquake-resistant construction*. New York: Wiley.
- Kujansuu R, 1964.** Nuorista siirroksista Lapissa. (Recent faulting in Lapland). *Geologi* 16, 30–36. (In Finnish.)
- Langer C J, Bollinger G A, 1991.** The southeastern Illinois earthquake of 10 June 1987: the later aftershocks. *Bulletin of the Seismological Society of America* 81, 423–445.
- La Pointe P, Wallmann P, Thomas A, Follin S, 1997.** A methodology to estimate earthquake effects on fractures intersecting canister holes. SKB TR 97-07, Svensk Kärnbränslehantering AB.
- La Pointe P R, Cladouhos T, Follin S, 1999.** Calculation of displacement on fractures intersecting canisters induced by earthquakes: Aberg, Beberg and Ceberg examples. SKB TR-99-03, Svensk Kärnbränslehantering AB.
- La Pointe P R, Cladouhos T T, Outters N, Follin S, 2000.** Evaluation of the conservativeness of the methodology for estimating earthquake-induced movements of fractures intersecting canisters. SKB TR-00-08, Svensk Kärnbränslehantering AB.
- La Pointe P R, Cladouhos T, Follin S, 2002.** Development, application, and evaluation of a methodology to estimate distributed slip on fractures due to future earthquakes for nuclear waste repository performance assessment. *Bulletin of the Seismological Society of America* 92, 923–944.
- Lemos J V, 2008.** Block modelling of rock masses: concepts and application to dam foundations. *European Journal of Environmental and Civil Engineering* 12, 915–949.

- Leonard M, 2010.** Earthquake fault scaling: self-consistent relating of rupture length, width, average displacement, and moment release. *Bulletin of the Seismological Society of America* 100, 1971–1988.
- Lund B, Schmidt P, 2011.** Stress evolution and fault stability at Olkiluoto during the Weichselian glaciation. Posiva Working Report 2011-14, Posiva Oy, Finland.
- Lund B, Zoback M D, 1999.** Orientation and magnitude of *in situ* stress to 6.5 km depth in the Baltic Shield. *International Journal of Rock Mechanics and Mining Sciences* 36, 169–190.
- Lund B, Schmidt P, Hieronymus C, 2009.** Stress evolution and fault stability during the Weichselian glacial cycle. SKB TR-09-15, Svensk Kärnbränslehantering AB.
- Lundqvist J, Lagerbäck R, 1976.** The Pärve Fault: A late-glacial fault in the Precambrian of Swedish Lapland. *GFF* 98, 45–51.
- Lönnqvist M, Hökmark H, 2015a.** Thermal and thermo-mechanical evolution of the Äspö Prototype Repository rock mass. Modelling and assessment of sensors data undertaken in connection with the dismantling of the outer section. SKB R-13-10, Svensk Kärnbränslehantering AB.
- Lönnqvist M, Hökmark H, 2015b.** Assessment of method to model slip of isolated, non-planar fractures using 3DEC. In Proceedings of 13th International Symposium on Rock Mechanics (ISRM Congress 2015), Montreal, Canada, 10–13 May 2015. International Society for Rock Mechanics and Rock Engineering.
- Lönnqvist M, Kristensson O, Fälth B, 2010.** Assessment of a KBS-3 nuclear waste repository as a plane of weakness. SKB R-10-36, Svensk Kärnbränslehantering AB.
- Ma K-F, Brodsky E E, Mori J, Ji C, Song T-R A, Kanamori H, 2003.** Evidence for fault lubrication during the 1999 Chi-Chi, Taiwan, earthquake (M_w 7.6). *Geophysical Research Letters* 30. doi:10.1029/2002gl015380
- Marshall S T, Morris A C, 2012.** Mechanics, slip behavior, and seismic potential of corrugated dip-slip faults. *Journal of Geophysical Research: Solid Earth* 117. doi:10.1029/2011jb008642
- Martin C D, 2007.** Quantifying in situ stress magnitudes and orientations for Forsmark. Forsmark stage 2.2. SKB R-07-26, Svensk Kärnbränslehantering AB.
- Muir-Wood R, King G C P, 1993.** Hydrological signatures of earthquake strain. *Journal of Geophysical Research: Solid Earth* 98, 22035–22068.
- Munier R, Hökmark H, 2004.** Respect distances. Rationale and means of computation. SKB R-04-17, Svensk Kärnbränslehantering AB.
- Munier R, Hökmark H, Fälth B, 2008.** Respect distances; rationale and means of computation. In Proceedings of the 33rd International Geological Congress, Oslo, 6–14 August 2008.
- Mörner N-A, 1978.** Faulting, fracturing, and seismicity as functions of glacio-isostasy in Fennoscandia. *Geology* 6, 41–45.
- Nábelek J, Suárez G, 1983.** The Goodnow earthquake in the central Adirondacks, New York: rupture of a simple circular crack. *Bulletin of the Seismological Society of America* 79, 1762–1777.
- Ohio Geological Survey, 1986.** Northeastern Ohio Quake, January 1986. Available at: <http://geosurvey.ohiodnr.gov/quakes-1950-to-1999-pgs/northeastern-ohio-january-1986>
- Olesen O, 1985.** Postglacial faulting at Masi, Finnmark, Northern Norway. In Proceedings of the 15th Meeting of the Nordic Association for Applied Geophysics, Espoo, Finland, 15–17 January 1985.
- Ritz E, Pollard D D, 2012.** Stick, slip, and opening of wavy frictional faults: a numerical approach in two dimensions. *Journal of Geophysical Research: Solid Earth*. 117. doi:10.1029/2011jb008624
- Scholz C H, 2002.** The mechanics of earthquakes and faulting. 2nd ed. Cambridge: Cambridge University Press.
- Segedin C, 1951.** Note on a penny-shaped crack under shear. *Mathematical Proceedings of the Cambridge Philosophical Society* 47, 396–400.
- SKB, 1992.** SKB 91 – Final disposal of spent nuclear fuel. Importance of the bedrock for safety. SKB TR 92-20, Svensk Kärnbränslehantering AB.

- SKB, 1999.** Deep repository for spent nuclear fuel. SR 97 – Post-closure safety. Main report – Vol. I, Vol. II and Summary. SKB TR-99-06, Svensk Kärnbränslehantering AB.
- SKB, 2001.** RD&D-Programme 2001. Programme for research, development and demonstration of methods for the management and disposal of nuclear waste. SKB TR-01-30, Svensk Kärnbränslehantering AB.
- SKB, 2004.** RD&D-Programme 2004. Programme for research, development and demonstration of methods for the management and disposal of nuclear waste, including social science research. SKB TR-04-21, Svensk Kärnbränslehantering AB.
- SKB, 2008.** Site description of Forsmark at completion of the site investigation phase. SDM-Site Forsmark. SKB TR-08-05, Svensk Kärnbränslehantering AB.
- SKB, 2009a.** Design premises for a KBS-3V repository based on results from the safety assessment SR-Can and some subsequent analyses. SKB TR-09-22, Svensk Kärnbränslehantering AB.
- SKB, 2009b.** Underground design Forsmark. Layout D2. SKB R-08-116, Svensk Kärnbränslehantering AB.
- SKB, 2010.** Data report for the safety assessment SR-Site. SKB TR-10-52, Svensk Kärnbränslehantering AB.
- SKB, 2011.** Long-term safety for the final repository for spent nuclear fuel at Forsmark. Main report of the SR-Site project. SKB TR-11-01, Svensk Kärnbränslehantering AB.
- SKBF/KBS, 1977.** KBS 1 – Kärnbränslecykelns slutsteg. Förglasat avfall från upparbetning, II Geologi. Svensk Kärnbränsleförsörjning AB.
- SKBF/KBS, 1983.** KBS 3 – Final storage of spent nuclear fuel – KBS-3, II Geology. Svensk Kärnbränsleförsörjning AB.
- Slemmons D B, Chung D, 1982.** Maximum credible earthquake magnitudes for the Calaveras and Hayward fault zones, California. In Proceedings of the Conference on Earthquake Hazards in the Eastern San Francisco Bay Area. Sacramento, CA: California Division of Mines and Geology. (Special publication 62)
- Slunga R, 1990.** The earthquakes of the Baltic shield. SKB TR 90-30, Svensk Kärnbränslehantering AB.
- Slunga R S, 1991.** The Baltic Shield earthquakes. *Tectonophysics* 189, 323–331.
- Stanfors R, Ericsson L O (eds), 1993.** Post-glacial faulting in the Lansjärv area, Northern Sweden. Comments from the expert group on a field visit at the Molberget post-glacial fault area, 1991. SKB TR 93-11, Svensk Kärnbränslehantering AB.
- Stephansson O, Savilahti T, Bjarnason B, 1989.** Rock mechanics of the deep borehole at Gravberg, Sweden. In Fourmaintraux D, Maury V (eds). *Rock at great depth, Vol. 2: proceedings of ISRM International Symposium, Pau, France, 30 August – 2 September 1989*. Rotterdam: Balkema, 863–870.
- Stephansson O, Ljunggren C, Jing L, 1991.** Stress measurements and tectonic implications for Fennoscandia. *Tectonophysics* 189, 317–322.
- Suikkanen J, Lönnqvist M, Hökmark H, 2016.** Analyses of the stability of a KBS-3H deposition drift at the Olkiluoto site during excavation, thermal loading and glacial loading. Posiva 2016-15, Posiva Oy, Finland.
- Thomas A L, 1993.** POLY3D: A three-dimensional, polygonal element, displacement discontinuity boundary element computer program with applications to fractures, faults, and cavities in the earth's crust. Master's thesis. Department of Geology, Stanford University.
- Wald D J, Heaton T H, 1994.** Spatial and temporal distribution of slip for the 1992 Landers, California, earthquake. *Bulletin of the Seismological Society of America* 84, 668–691.
- Wells D L, Coppersmith K J, 1994.** New empirical relationships among magnitude, rupture length, rupture width, rupture area, and surface displacement. *Bulletin of the Seismological Society of America* 84, 974–1002.
- Zoback M D, Townend J, 2001.** Implications of hydrostatic pore pressures and high crustal strength for the deformation of intraplate lithosphere. *Tectonophysics* 336, 19–30.

Thermally induced earthquakes in Forsmark

A1 Background

The Swedish Radiation Safety Authority (SSM) has requested SKB to complete its SR-Site assessment of the seismic risk by addressing also the possibility of thermally induced seismicity in the repository host rock, i.e. earthquakes triggered by the thermomechanical effects of the heat generated by the decaying spent fuel (SSM2011-2426-90). A PM (Fälth and Hökmark 2013), on this issue was prepared and delivered to SSM on September 2013. In this appendix, the essence of that PM is presented. In particular, we describe and report on the modelling performed to arrive at the result examples labelled “ZFMA2, 100 years of heating” and “ZFMA2, 1000 years of heating” in the results overview (Figures 4-4 and 4-5 in the main text).

A2 Preliminary assessment

Given the initial reverse faulting stress regime from ground surface down to a depth of about two km in the Forsmark bedrock, the only deformation zones with potentially unstable surface segments large enough to host reasonably large earthquakes are the gently dipping ones (Fälth et al. 2016). Figure A-1 illustrates how the thermal stress addition affects the gently dipping Forsmark deformation zone ZFMA2. The shear stress addition is about 3 MPa, at most, and is differently oriented at different depths. This stays in contrast to the glacially induced stress addition during the end-glacial phase, which adds to the present-day shear load at all depths (Figure A-2). Thus, one could expect a thermally induced earthquake to generate less slip and seismic moment than a corresponding end-glacial earthquake. However, since the modelling approach taken here implies that the zone strength is almost completely lost during the rupture, and a significant amount of tectonically accumulated strain energy is released in both cases, the difference is not necessarily large.

The effects on the repository in terms of induced target fracture displacements, are determined not only by the magnitude of the earthquake, but also by the stability of the fractures within the repository. Figure A-3 shows, for three cases, the stability at repository depth for fractures dipping along the direction of the major principal stress:

- Fractures within the deposition areas during the thermal phase.
- Fractures between the deposition areas during the thermal phase.
- Arbitrarily located fractures during a glaciation cycle.

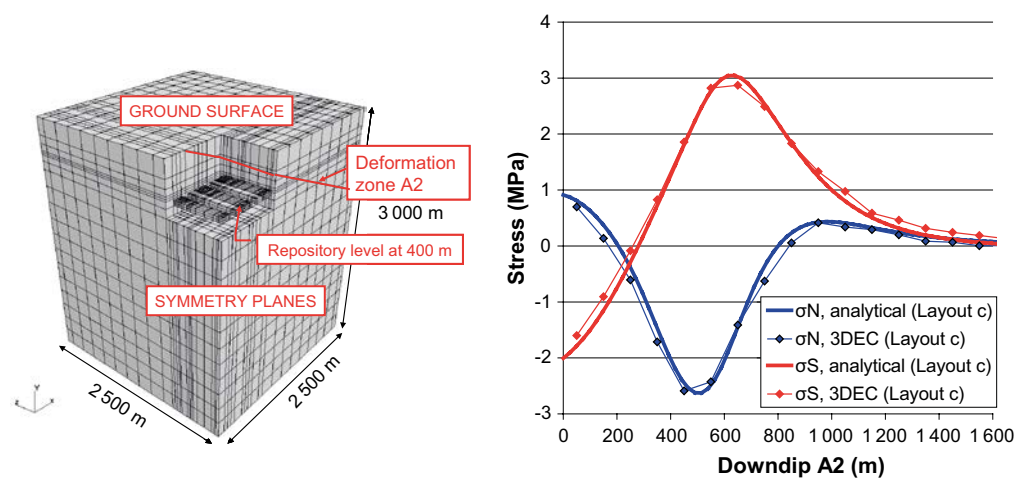


Figure A-1. Left: Schematic thermomechanical 3DEC model of the repository. Approximate location and orientation of deformation zone ZFMA2 are indicated. Right: Thermally induced normal and shear stress on the ZFMA2 plane after 500 years. Positive normal stress additions mean increased compression. Results from the 3DEC model are presented along with corresponding analytically calculated results (from Hökmark et al. 2010, App. A).

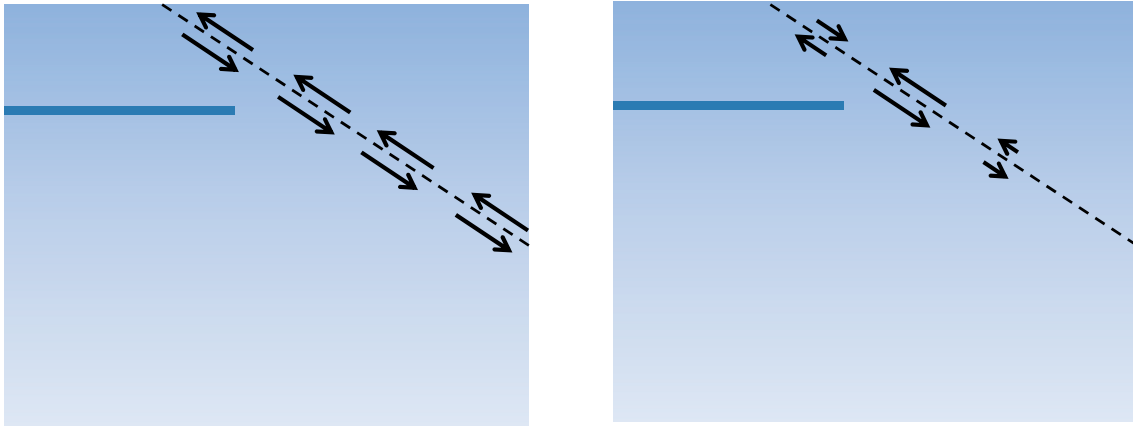


Figure A-2. Principal difference between end-glacial shear load (left) and thermally generated shear load (right) on fracture zone with position and orientation as ZFMA2. Horizontal line indicates the position of the Forsmark repository.

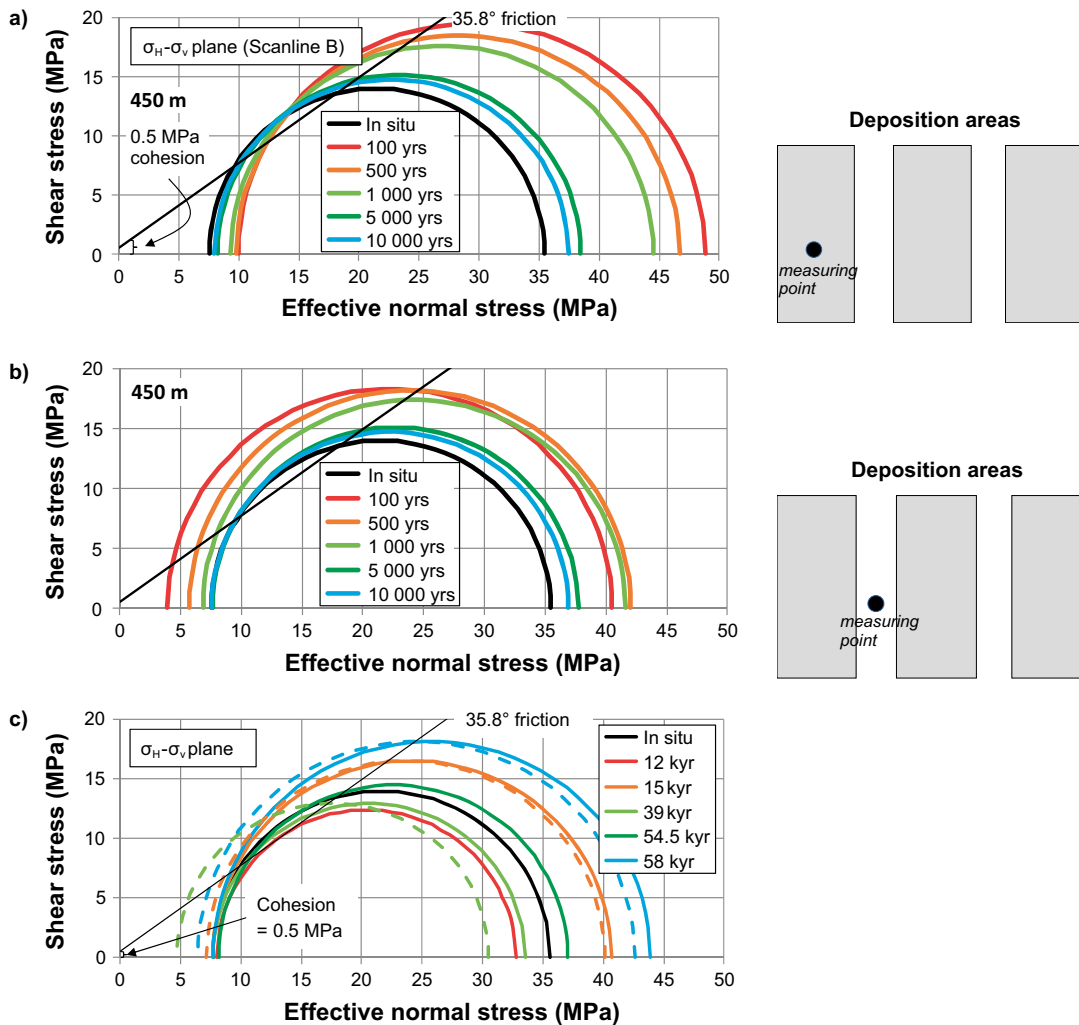


Figure A-3. Mohr circle representation of fracture stability at repository depth during different phases and at different positions (Hökmark et al. 2010). The schematic sketches to the right show typical stress monitoring positions. a) Inside a deposition area during the thermal phase, b) between and around deposition areas during the thermal phase, and c) at an arbitrary location during a glaciation cycle. The end-glacial phase corresponds to 58 kyr in c). The dashed circles correspond to the assumption of 1 MPa pore pressure increase. This assumption is made in the simulations of end-glacial earthquakes. The values of friction angle and cohesion are based on Forsmark site data (cf. SKB 2010).

During the end-glacial phase (58 kyr), the stability margins are significantly lower than they are within the deposition areas during the thermal phase, particularly if the pore pressure at repository depth is assumed to be increased by 1 MPa during the end-glacial phase, as in the present simulations of end-glacial earthquakes. Note that 58 kyr is counted from the time instance when the stresses at Forsmark first are affected by the advancing ice cover.

Due to the expected smaller fault slip and higher fracture stability inside the deposition areas during the thermal phase, one should expect the induced fracture displacements to be smaller during the thermal phase than under end-glacial conditions. However, the difference is difficult to quantify based on these general observations.

A3 Problem statement

The purpose, or main objective, of this investigation is not to attempt any prediction of the rupture mechanism or the magnitude of any thermally induced earthquake in Forsmark. The purpose is to investigate, using the same modelling approach as for the end-glacial earthquake scenario, whether or not a thermally induced earthquake, or an earthquake occurring during the thermal phase, could have any consequences that would require any specific attention. One way to do this is to compare results from numerical models of end-glacial earthquakes and thermally induced earthquakes that are based on identical model geometries, identical background stresses, identical target fracture mechanical properties and identical rupture mechanisms. This is the approach applied here. Hence, it is assumed that the rupture mechanism is the same irrespectively of the stress situation.

The basic assumption made here in the description of the possible risk of a thermally induced earthquake is the same as that made by Fälvh et al. (2010); shear displacements on fractures intersecting canister positions is the only effect of earthquakes that could impact on the repository safety. Thermally induced spalling in the deposition hole walls could possibly be regarded as an exception. However, to study the implications of spalling is not within the scope of this study.

We point out that the focus here is on indirect, or secondary, effects on fractures induced by nearby large earthquakes. Shear displacements on host rock fractures that take place in direct response to the thermal load could possibly take place through rapid pulses, i.e. seismically, rather than through time-continuous displacements that follow the slowly increasing thermal load on planar fractures governed by ideal elasto-plastic constitutive relations (cf. Hökmark et al. 2010). The displacements generated by such small earthquakes would, however, differ only marginally from the time-continuous displacements calculated by Hökmark et al. (2010). According to that study, the maximum displacement induced by the thermal load on optimally oriented fractures inside the deposition areas will, with margin, be smaller than the canister failure criterion (Figure A-4). The thermal stress additions depicted in Figure A-4a were obtained from a large-scale model while the corresponding fracture shear displacements in Figure A-4b were generated using a closed-form solution where it is assumed that the fracture is uniformly loaded.

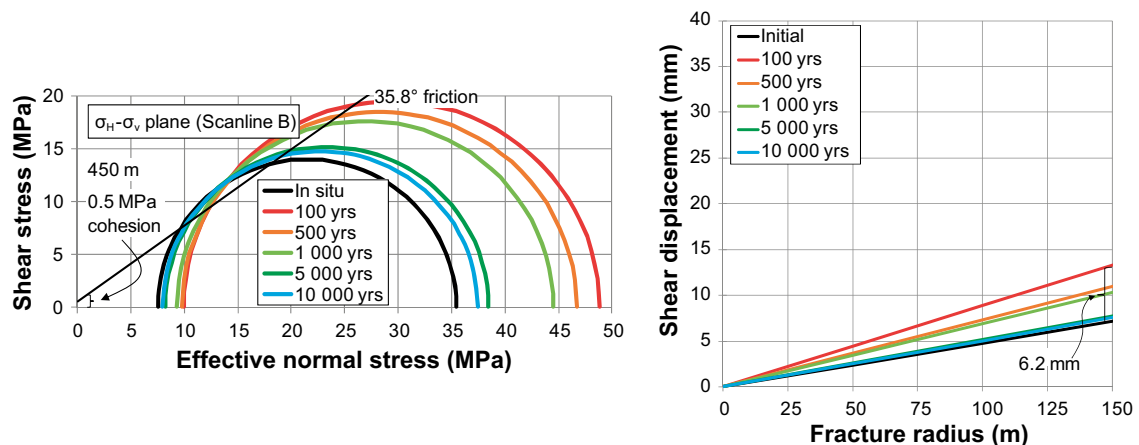


Figure A-4. Left: Mohr circle representations in the σ_H - σ_v -plane of the stress states inside a deposition area (cf. Figure A-3a). Right: Corresponding estimates of the maximum slip at the centre of a fracture dipping 27.1° from the horizontal plane (Figure 6-28 in Hökmark et al. 2010).

A4 Model set up

The point of departure is a version of the end-glacial ZFMA2 models analysed by Fälth et al. (2016). Figure A-5 shows the outline of the model. The gently dipping earthquake zone ZFMA2 has an area of 12 km², breaches the ground surface and terminates at the steeply dipping deformation zone ZFMNW0017 in the west. The ZFMNW0017 zone is not included in this model version but is included in the figure to help clarify the geometry. Numerous 300 m diameter target fractures are modelled at 500 m depth at three different distances from the fault plane.

A4.1 Stresses and initial conditions

Figure A-6a and c show the assumed present-day stresses. Down to 2 km depth these are of reverse faulting type and in accord with the "most likely" stress model suggested for the Forsmark site (SKB 2008). At repository depth the site model stresses are exactly reproduced. At larger depths (below 2 km) the stress situation is more uncertain. For these depths, empirical data and the literature suggest a strike-slip stress regime (Stephansson et al. 1989, Lund and Zoback 1999). The potentially important deformation zones in Forsmark do not reach depths larger than a few kilometres, meaning that the stress uncertainties at very large depths are not necessarily important.

For the end-glacial earthquake model, the stresses prevailing at the time of rupture initiation (Figure A-6b, d) are the sum of the present-day stresses and glacial stresses obtained from GIA (Glacial Isostatic Rebound) modelling performed by Lund et al. (2009). This approach is identical to that used by, for instance, Fälth et al. (2016).

For the modelling of thermally induced earthquakes, the heat generation and the associated evolution of thermal stresses were explicitly calculated using the same 3DEC model geometry (Figure A-5) but with heat sources, i.e. the fuel canisters, positioned according to Layout D2, however at 500 m depth (Figure A-7). The initial canister heat power and the power decay, as well as the thermal and the thermomechanical properties of the repository host rock, were set as in the SR-site analyses of the thermomechanical evolution at the Forsmark site (Hökmark et al. 2010). Two in situ stress cases were selected for dynamic analyses: the stresses after 100 years and 1000 years of heat generation.

For the end-glacial analyses the pore pressure was set at the hydrostatic pore pressure plus 1 MPa at repository depth and at the hydrostatic pressure for the thermal analyses.

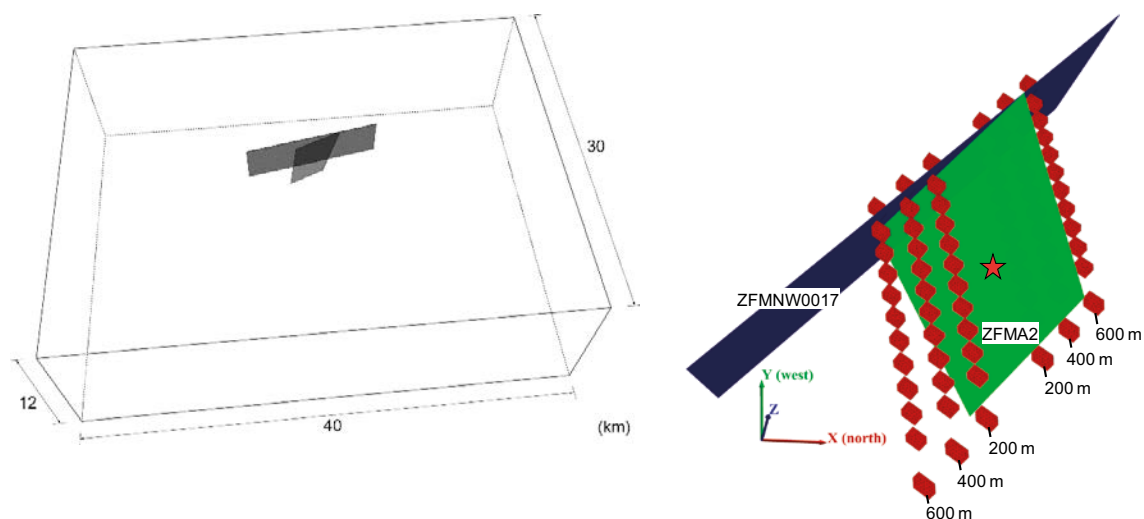


Figure A-5. Model geometry. The red star on the ZFMA2 plane indicates the location of the hypocentre (same for all cases presented here)

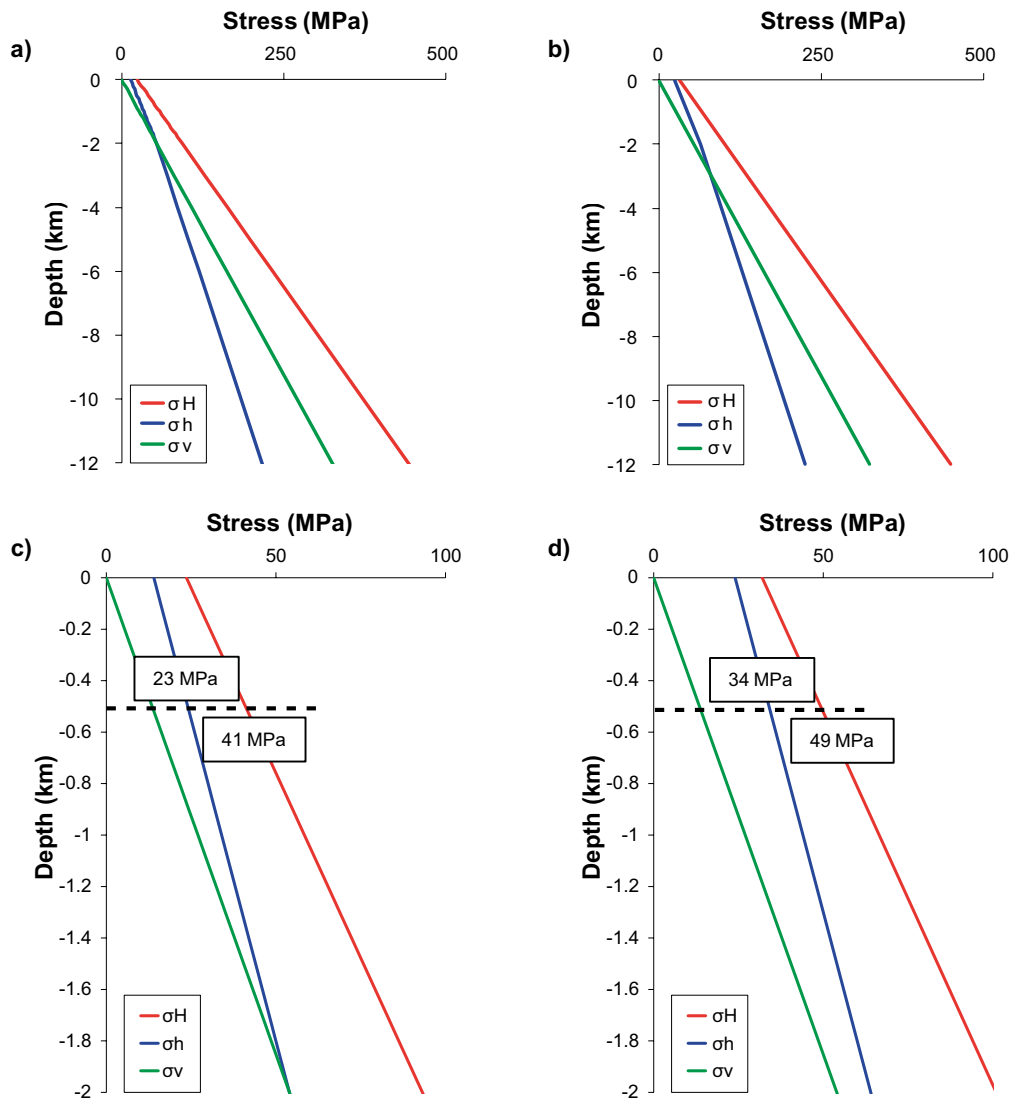


Figure A-6. a) Present-day Forsmark background stresses. b) Forsmark stresses under end-glacial conditions. c) and d) are close-ups of a) and b), respectively, showing the horizontal stresses at 500 m depth. The two horizontal stress additions are about 11 MPa and 8 MPa at all depths relevant for this study (glacial stress additions from Lund et al. (2009)).

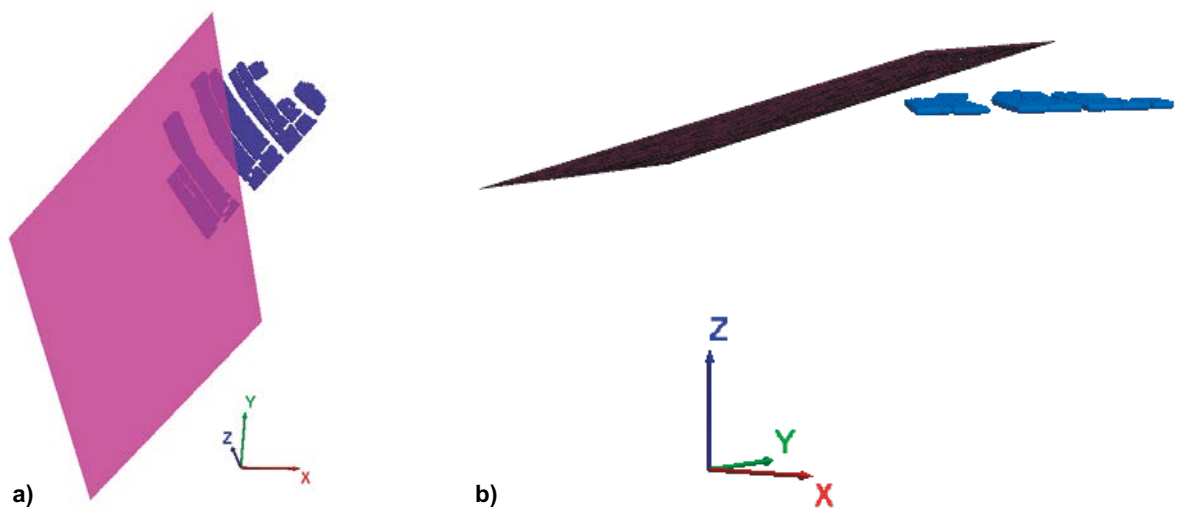


Figure A-7. Positions of the heat sources (blue) according to layout D2 on the footwall side of ZFMA2. a) viewed from above and b) viewed from NE.

A4.2 Rupture mechanism

The rupture mechanism is implemented by use of the 3DEC built-in programming language *FISH*. Rupture propagation is simulated using a constant rupture velocity time-weakening model. The rupture is initiated at a predefined point, the hypocentre, and programmed to propagate outwardly along the fault plane at a velocity corresponding to 70 % of the shear wave velocity of the surrounding elastic medium. As soon as the rupture front arrives at a point on the fault, the shear strength at that point is set to correspond to the acting local shear load and then ramped down to a residual shear strength over a predefined time interval. The residual strength is determined by a low friction coefficient $\mu_{res} = 0.09 = \tan(5^\circ)$ and zero cohesion. The time interval used to ramp down the strength is set at 1.5 sec. A similar method to propagate the rupture was applied by Cruz-Atienza et al. (2015) to model seismic tremor sources on hundreds of small penny-shaped faults. A simulation using the time-weakening model was also performed by Andrews (2004). However, in that study a spontaneous rupture was simulated.

A5 Modelling

The point of departure for the dynamic analyses is a state of mechanical equilibrium under the initial conditions, i.e. the present-day stresses shown in Figure A-6a, c, the end-glacial stresses shown in Figure A-6b, d or the thermal stresses 100 and 1000 years after deposition calculated as described in Hökmark et al. (2010), assuming the geometry outlined in Figure A-7.

During the quasi-static calculation steps performed to arrive at the different states of initial equilibrium, the shear strength of the ZFMA2 deformation zone was kept high enough to suppress any aseismic fault slip and release of strain energy. This was done in order to maximize the moment magnitude in the subsequent dynamic calculation step.

For the end-glacial case, 22 model versions were analysed, each with a different orientation of the 72 target fractures. Figure A-8 shows the 22 target fracture orientations. 15 of these are orientations of fracture sets given in the Forsmark site model in Fracture domains FFM01 and FFM06. The remaining seven sets are generic. For each of the two thermal cases, two target fracture orientations were considered. These are specifically indicated in Figure A-8. As opposed to the earthquake fault, the target fractures were allowed to slip aseismically during the quasi-static calculation step. The fracture displacement results presented in the following do, however, include only co-seismic displacements, i.e. displacements generated during earthquake rupture.

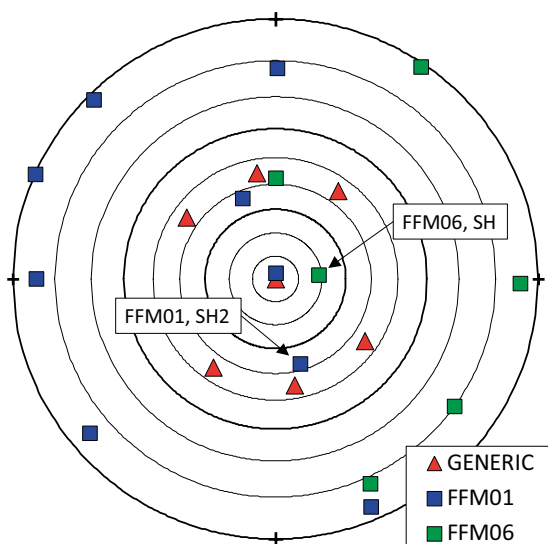


Figure A-8. Target fracture orientations. The target fractures considered in the thermal case are indicated with arrows.

A6 Results

A6.1 Fault slip

Figure A-9, upper left, shows 6 positions on the ZFMA2 plane, selected for illustration of the temporal slip evolution during rupture. The slip evolution during the end-glacial rupture is shown in the upper right and the corresponding results for thermally induced ruptures occurring 100 and 1 000 years after deposition are shown to the left and to the right, respectively, in the bottom row.

The seismic moment, which by definition scales with the average slip (\bar{U}) for identical assumptions regarding the rupture area (RA) and the mechanical properties of the surrounding continuum, is more than 50 % larger for the end-glacial earthquake than for the thermally induced earthquakes. Considering the principal difference between the shear loads under end-glacial and thermal conditions (Figure A-2) this should, qualitatively, be an expected result: The entire fault area is under uniform end-glacial shear load, whereas the thermally induced shear load addition varies in magnitude and orientation.

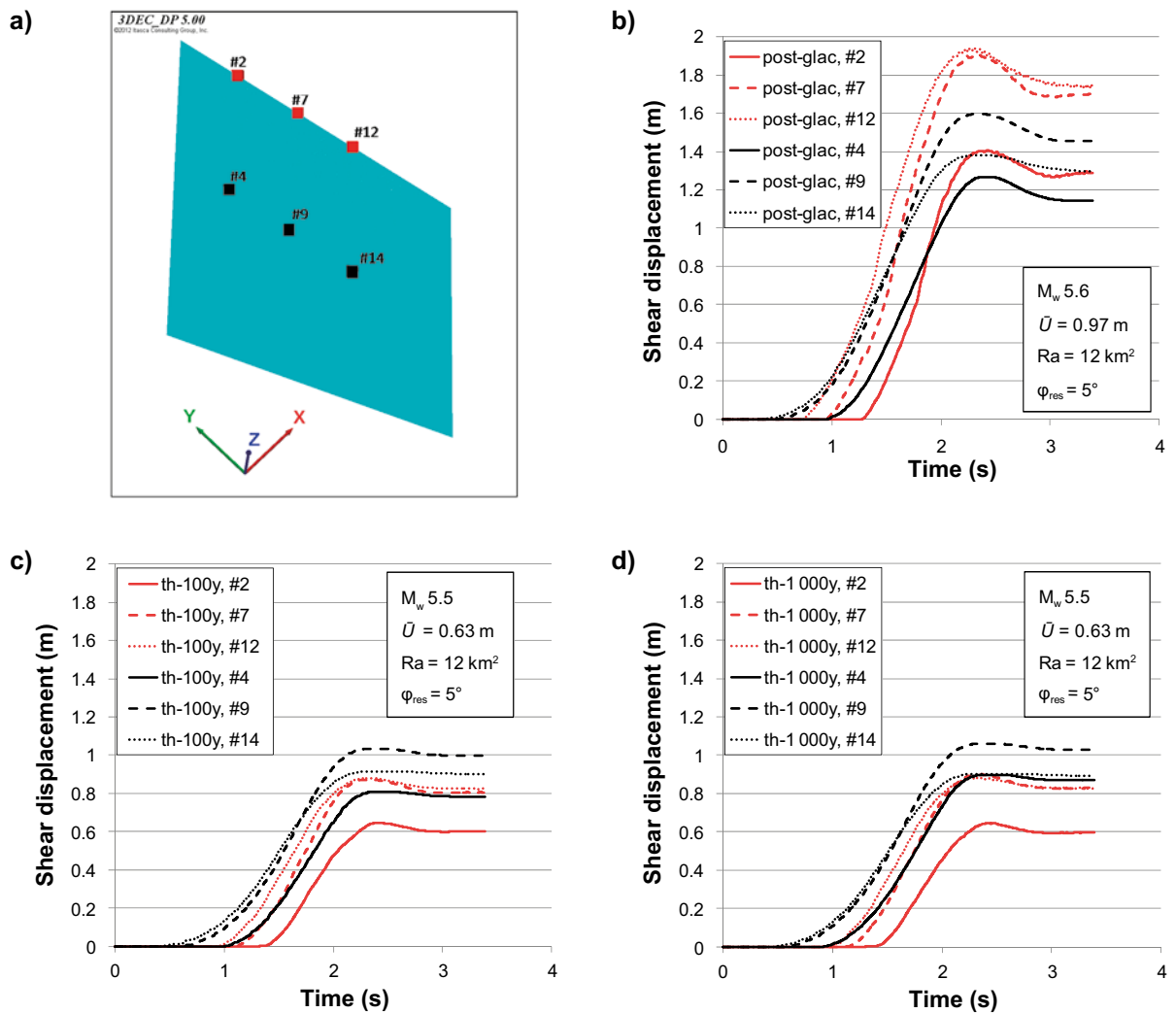


Figure A-9. Fault slip evolution at six positions (a) on ZFMA2 fault plane for end-glacial case (b) and for 100 y (c) and 1 000 y (d) thermal cases. The hypocentre is located approximately between points #9 and #14.

As modelled here, the slip evolution for an earthquake occurring 1000 years after deposition is only marginally different from that of an earthquake occurring 100 years after deposition (Figure A-9, bottom row). Yet the thermal stresses at some distance from the deposition areas are significantly higher after 1000 years than after 100 years (cf. Figure A-10). The insignificant difference between the 100y results and the 1000y results is explained by the modest and unsystematic contribution of the thermal stresses (even at the time of maximum thermal stresses) to the overall shear load on ZFMA2. As pointed out in Section A.2, the low residual fault strength leads to release of a considerable amount of tectonically accumulated strain energy during fault slip. This means that the modest and unsystematic stress contribution from the heating has an insignificant impact on the fault slip. This is illustrated in Figure A-11, where results from a test model with an earthquake powered by the present-day stresses only, i.e. with zero thermal load, are compared with corresponding results from the 1000y model.

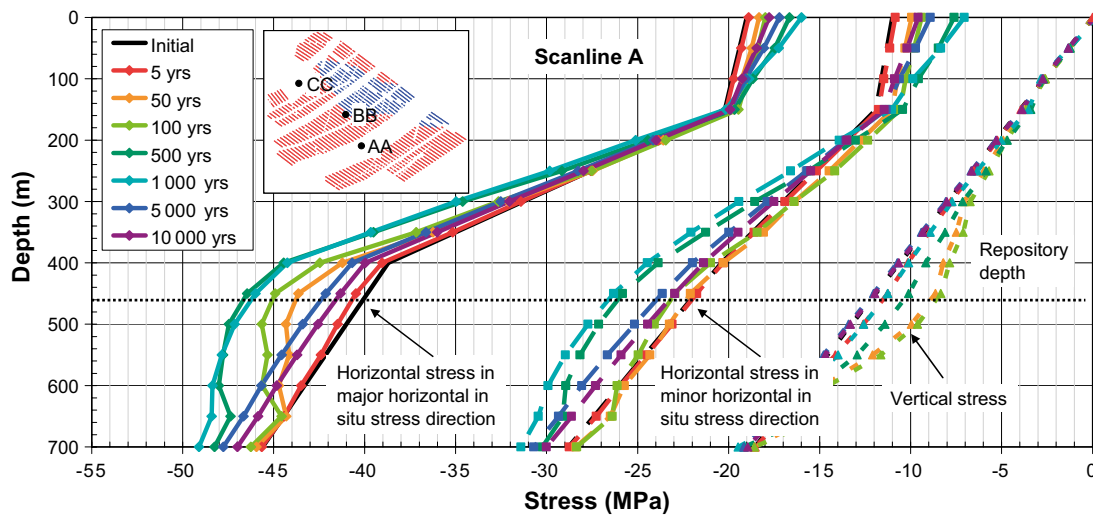


Figure A-10. Stresses a short distance away from the deposition areas during the thermal period (compressive stresses are negative). From Hökmark et al. (2010). Here (vertical scanline A, see inset) the thermal stresses are at maximum about 1000 years after deposition. The horizontal thermal stresses range between 5 and 7 MPa at the repository horizon and are significantly lower above and below. At the location of ZFMA2, outside the repository footprint, the thermal stresses are even smaller:

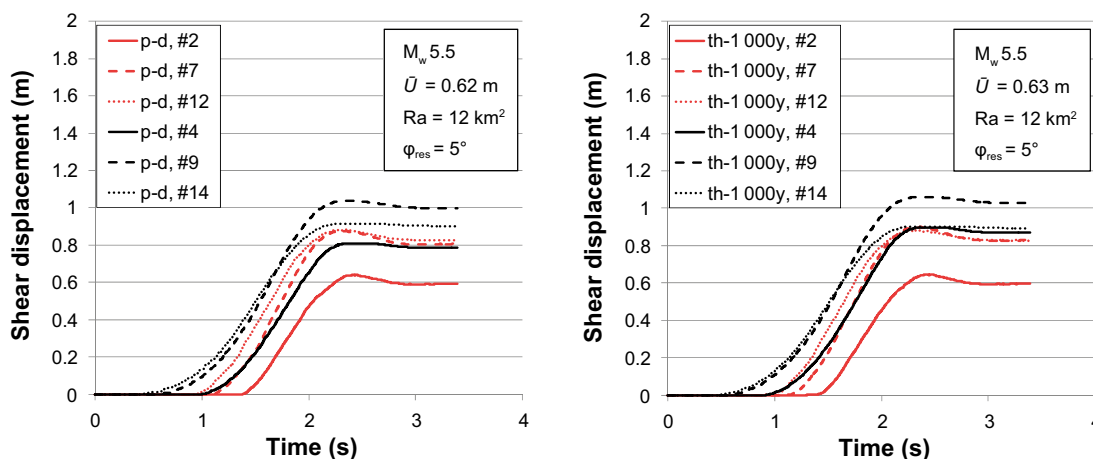


Figure A-11. Fault slip evolution at six positions (see Figure A-9a) in test model with zero thermal load (present-day) (left) compared with corresponding results from 1000y thermal case (right).

A6.2 Target fracture slip

Figure A-12 shows target fracture peak slip on the footwall side and on the hanging wall side obtained for the end-glacial earthquake. Each plot includes $12 \times 22 = 264$ slip results for each of the distances considered, i.e. all target fracture orientations shown in Figure A-8 are included. At a few positions in the hanging wall, unfortunately oriented fractures slip by very significant amounts. As discussed and illustrated by Fälth et al. (2016), these large hanging wall slip results are confined to a small region around one of the fault edges. Since the Forsmark repository will be located on the footwall side of ZFMA2, no systematic attempts have been made, as of yet, to devise and apply a credible fault edge representation, i.e. one that produces a less abrupt arrest of the rupture and a more realistic stress concentration in the fault edge regions. The results presented and discussed in the following in this assessment of thermally induced earthquakes in Forsmark regard only target fracture slip on the footwall side of ZFMA2, i.e. where the deposition areas are located.

Figure A-13, left: target fracture displacements obtained in the thermal 100y case are compared with corresponding end-glacial results. Only the two fracture sets (out of 22) with the largest displacements in the end-glacial model case were included in the 100y thermal case (cf. Figure A-8). As expected, given the significantly larger seismic moment in the end-glacial case (cf. Figure A-9 and associated text), the end-glacial case gives systematically larger target fracture displacements. The maximum end-glacial slip is about 15 % larger than the maximum 100y thermal slip.

Figure A-13, right: Target fracture displacement obtained in the 1000y thermal case are compared with corresponding results obtained in the 100y thermal case. As expected, given the almost identical seismic moments and the almost identical styles of fault slip evolution (cf. Figure A-9 and associated text) the differences in target fracture response between the 100y thermal case and the 1000y thermal case are insignificant.

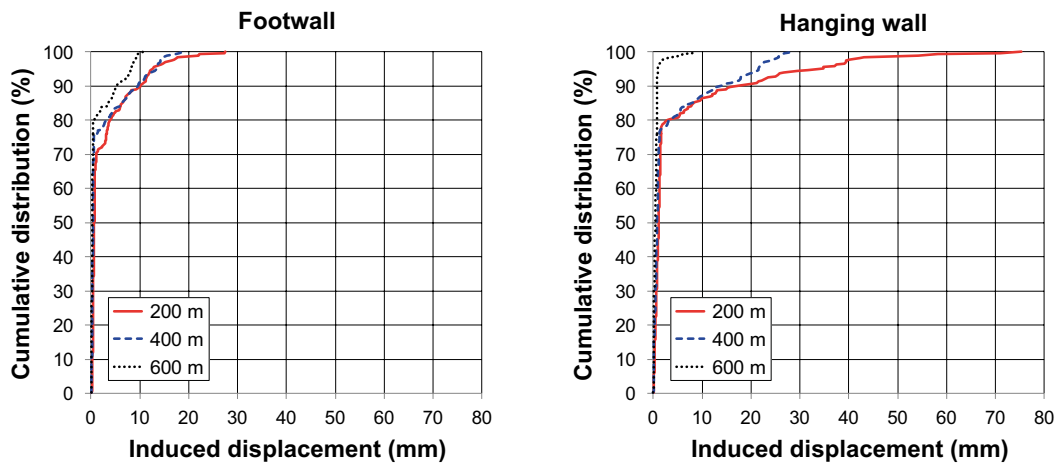


Figure A-12. Target fracture slip, end-glacial model case. The figure includes results from 22 model versions, each corresponding to one of the target fracture orientations shown in Figure A-8, i.e. altogether 1584 results (both sides, cf. Figure A-5 for positions). No attempts have been made to account for the probability distribution of the different orientations, i.e. all orientations are represented with the same weight.

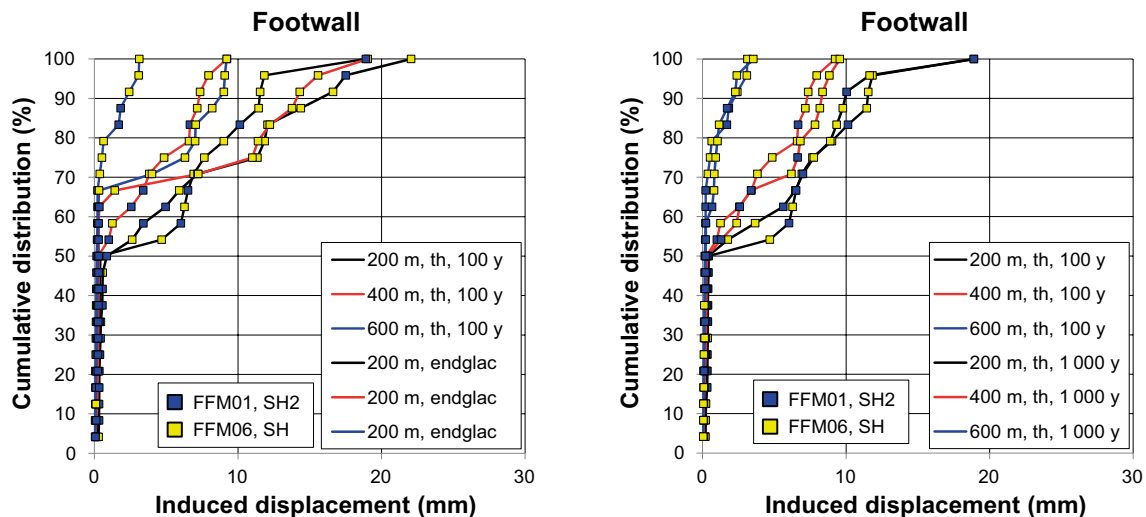


Figure A-13. Left: 100y thermal mode case target fracture slip for the two fracture orientations (both gently dipping) giving the largest footwall side slip in the end-glacial case. Corresponding end-glacial results are included for comparison. Right: 1000y thermal model case target fracture slip compared with corresponding 100y target fracture slip. Only footwall results are shown in this figure.

A7 Summary and conclusions

In this investigation it is shown that the effects, in terms of secondary fracture displacements, of an earthquake occurring at the Forsmark site during the thermal phase are sufficiently smaller than the corresponding effects of a corresponding end-glacial earthquake, that the potential risk posed by thermally induced earthquakes can be regarded to be handled by the end-glacial analyses.

Here, results from site-specific models including thermal load are compared with corresponding models where end-glacial loads are applied. Given the present understanding of the present-day stress field and of the end-glacial stress additions, the only deformation zone at Forsmark that can be regarded a potential end-glacial earthquake zone is the gently dipping ZFMA2. This zone has the lowest stability during present-day conditions and is the only zone at the site that will become further destabilized in the end-glacial phase. The other zones, all steeply dipping, will instead gain stability. Even though the thermal load is less extensive and not as uniform over large volumes as the glacial load, the stability effects are similar as for the end-glacial case; steeply dipping zones are stabilized due to increased compression. Hence, the comparison of the effects of thermally induced earthquakes and end-glacial earthquakes is made with ZFMA2 as an example. The following can be concluded.

- The average fault slip in the thermally induced earthquake on ZFMA2 is approximately 60 % of the average fault slip in the corresponding end-glacial case.
- The influence on the ZFMA2 stability of the thermal load is practically negligible. The results that are presented here regard the 100–1 000-year time frame, but since the temperatures are reduced for subsequent times, this conclusion can be regarded to be generally valid. Due to the negligible impact on the fault stability, the strain energy released by a thermally induced (or triggered) earthquake would correspond mainly to the already existing slowly accumulated tectonically strain energy.
- Due to the schematic and conservative modelling approach, with almost total loss of fault strength and release of large amounts of strain energy, the moment magnitude of the thermally induced earthquake becomes considerable: The magnitude is M_w 5.5, which should be compared with M_w 5.6 for the end-glacial event.
- The difference in secondary displacements generated by the 100y and 1 000y models amounts to a couple of mm. In addition, the difference is not systematic; some fractures move more during the 100y case while other fractures move more in the 1 000y case.

- The maximum secondary displacement in the footwall of ZFMA2, where the deposition areas are located, is for the thermally induced earthquake about 85 % of the corresponding displacement in the end-glacial case. The maximum displacement in the thermal case is 19 mm on a 150 m radius fracture at 200 m distance from the rupturing fault. This corresponds to about 40 % of the 50 mm canister failure criterion (SKB 2011) and to a critical radius of 395 m. Given the approach for extrapolation applied by Fälth et al. (2010), the critical radius at 100–200 m distance would be 197.5 m. With a less dramatic, and possibly more realistic loss of strength on ZFMA2, the critical radii would be even larger.

The general conclusion that can be drawn based on the present results is that the risk of canister damage at Forsmark during the thermal phase can be regarded as extremely low. Due to the modest and non-systematic shear load addition generated by the thermal load on ZFMA2, the increased probability of a thermally induced earthquake should be low. In addition, the largest earthquake that is theoretically possible, given the stresses and the geometry, would correspond to critical radii that are at least twice those suggested in the SR-Site work (cf. Fälth et al. 2010).

Influence of a Discrete Fracture Network on Seismically Induced Fracture Shear Displacements

Margareta Lönnqvist, Clay Technology AB
 Billy Fälth, Clay Technology AB
 Harald Hökmark, Clay Technology AB

April 2019

B1 Introduction and background

B1.1 General

A concern for the long-term safety performance of the repository is that fractures intersecting the repository openings could be remotely reactivated by the effects of a nearby earthquake and that the resulting shear displacements would be sufficiently large to damage the canisters (e.g. SKB 2011). Such secondary effects have been extensively studied with the purpose to establish safe upper bound estimates of earthquake-induced shear displacements along differently sized and oriented off-fault (target) fractures (Fälth et al. 2010, 2015, 2016). In all these studies, it has been assumed that the rock surrounding the earthquake fault and the target fractures is a homogenous, isotropic and linear elastic material. The distances between the target fractures have been chosen large enough for each individual fracture to respond to the seismic load independently of the response of its neighbour fractures (Fälth and Hökmark 2012) to reduce the impact of irrelevant modelling aspects upon the problem at hand. The modelling approach with target fractures being effectively isolated in an elastic continuum maximises the static stress redistribution effects around the fault and allows the seismic waves to propagate through the rock mass to the target fractures practically without loss of energy. In reality, some strain energy would be expended on inelastic deformations of the rock mass.

The impact of such inelastic deformations on the slip of potential target fractures has not been thoroughly investigated. It has previously been argued that attenuation effects would be small in the rock volume considered for the Forsmark repository due to a combination of short distances between faults and target fractures and good quality rock at the site (Fälth et al. 2010). However, scoping and preliminary test calculations have indicated that the maximum shear displacement along a fracture embedded in a local network of differently oriented smaller fractures could be around 20 % smaller than along a corresponding isolated fracture embedded in a linear elastic material, cf. Figure B-1. To investigate if the test results would be valid for the Forsmark repository, we model a generic earthquake with relevance for the Forsmark site and study the response of a target fracture embedded in discrete fracture networks (DFN) with different characteristics.

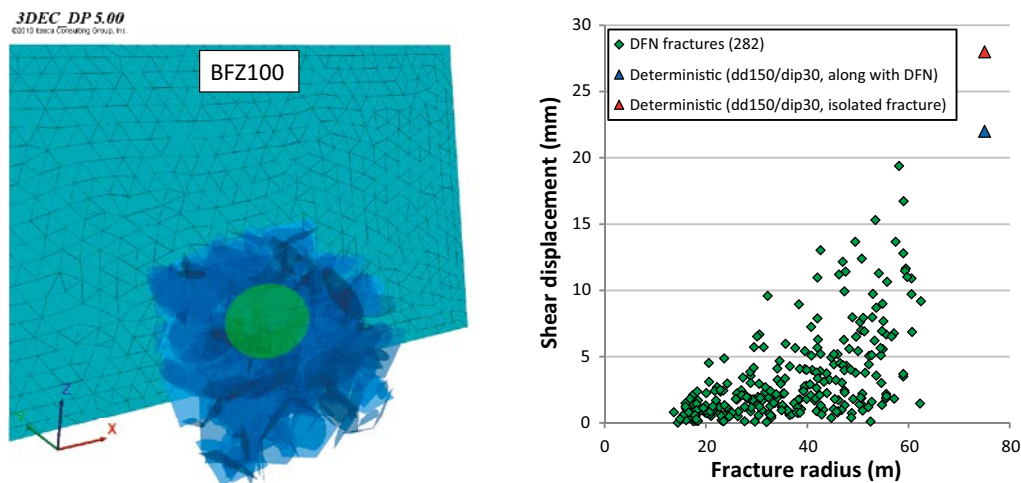


Figure B-1. Preliminary test calculation results from a model based on the BFZ100 simulation reported in Fälth and Hökmark (2011). Left: Earthquake fault (turquoise), DFN (blue) and target fracture (green). Right: Shear displacements along the DFN and the target fracture as functions of fracture radius.

B1.2 Objectives and scope

The objective of this study is to investigate how seismically induced fracture shear displacements along an optimally oriented target fracture are influenced by inelastic movements along surrounding, smaller fractures. The problem is addressed numerically by use of a dynamic, three-dimensional distinct element model of a thrust-faulting earthquake. Given that dynamic models become computationally very demanding with increasing level of detail, the effects of a fracture network are assessed through so called nesting, by combining two types of models: a large-scale model and several smaller, and more detailed, near-field models (cf. Figure B-2b). A method to import boundary conditions from the large-scale model to the near-field models has been developed within the framework of this study.

B1.3 Modelling tool

The problem described above is analysed numerically using the commercially available distinct element software 3DEC, v. 5.0 (Itasca 2013). 3DEC was originally developed for analyses of mechanical processes in discontinuous media such as fractured rock (Itasca 2013). The code handles static as well as dynamic loading and has been used extensively to address seismic issues of relevance for nuclear waste disposal in crystalline rocks (Fälth and Hökmark 2006a, 2011, 2012, 2015, Fälth et al. 2010).

A 3DEC model consists of an assemblage of blocks where the interfaces between the blocks represent fractures. To model a deformable material, the blocks are sub-divided into a mesh of finite-difference elements where each element responds to a prescribed stress-strain law. Similarly, the relative movements of the discontinuities in the normal and shear directions are governed by prescribed force-displacement relations. In this study, we use the “small strain” option in 3DEC (Lemos 2008, Itasca 2013). 3DEC includes a built-in programming language (*FISH*) that extends the capabilities of the software. *FISH* is used in this study to control the earthquake rupture in the large-scale model, to generate and import DFN models, to import and assign mechanical boundary conditions in the near-field models and to assign properties to the fractures.

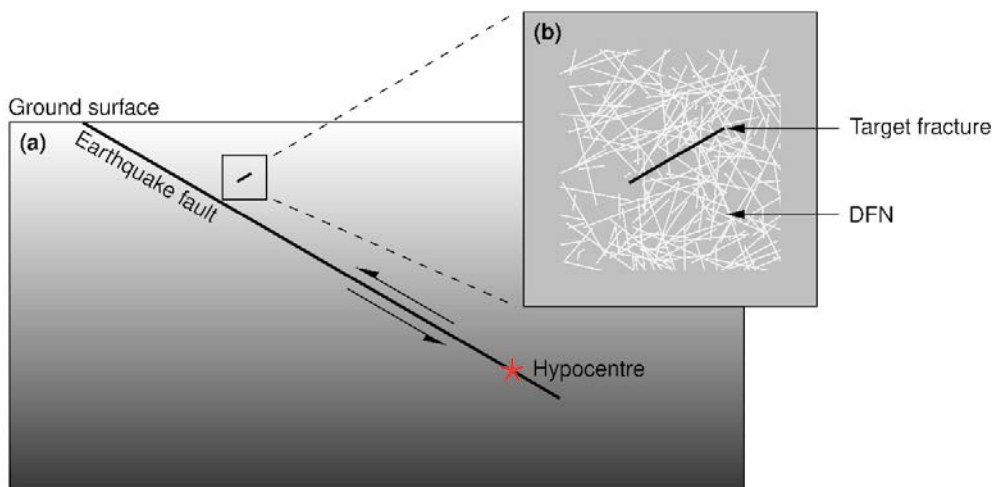


Figure B-2. Schematic illustration of the two types of models: (a) a large-scale model comprising the earthquake fault and one off-fault target fracture and (b) near-field models containing the target fracture surrounded by a discrete fracture network (DFN).

B1.4 Structure

This appendix is structured in three sections. The two first sections describe each aspect of the nested model separately, as follows:

Section 1.2 describes the large-scale earthquake model. This model is primarily used to generate mechanical boundary conditions for the near-field models, but does also serve as a means to, to some degree, verify the modelling approach used in the near-field models.

Section 1.3 describes the near-field models. These models are used to assess the influence of a DFN on the induced maximum shear displacement along a target fracture.

In Section 1.4, the results are discussed, and conclusions are drawn.

B2 Large-scale model

To provide displacement boundary conditions to the near-field model containing the target fracture and the DFN, we perform a simulation of a thrust faulting earthquake. This type of event would typically occur on a gently dipping fault zone, such as the ZFMA2 zone at the Forsmark site, under present-day reverse faulting stress conditions or under end glacial stress conditions (Fälth et al. 2016). In addition to the displacement boundary conditions, we also monitor the target fracture displacement, which is used as reference for the target fracture displacement generated in the near-field model.

B2.1 Model geometry

The model comprises a box which extends 45 km in the x -direction, 45 km in the y -direction and 20 km in the z -direction (Figure B-3, left). The upper boundary of the model represents the ground surface. The fault plane breaches the ground surface and is located close to the model centre. It has 4 km length along strike, 5 km down-dip width and dips 30° with respect to the horizontal. Given the stress field (cf. following section) the shallow dip angle means that it is possible to obtain a low fault stability at all depths using realistic fault strength parameter values and thereby propagate the earthquake rupture over the entire fault plane. The hypocentre is located centrally with respect to fault strike and at 4.5 km down-dip distance (Figure B-3, middle). In the hanging wall of the fault plane we insert a cut plane with dip 30° (Figure B-3, middle and right). Within a circular area on that plane, we assign fracture properties such that a circular target fracture with 75 m radius is formed. The centre of the target fracture is located at 500 m depth and at 300 m perpendicular distance from the fault plane. The target fracture is surrounded by a cube-shaped box with edge length 400 m (Figure B-3, right). Each side of the target fracture box is divided into 64 squares, all with edge length 50 m. At the centre of each square, we monitor the temporal evolutions of displacements in the x -, y -, and z -directions during the rupture. These displacement histories are then used as input to the near-field models. The relevance of using the same set of boundary conditions for all near-field models regardless of choice of DFN model, fracture intensity or parameter values assigned to the DFN may need further investigation in future work.

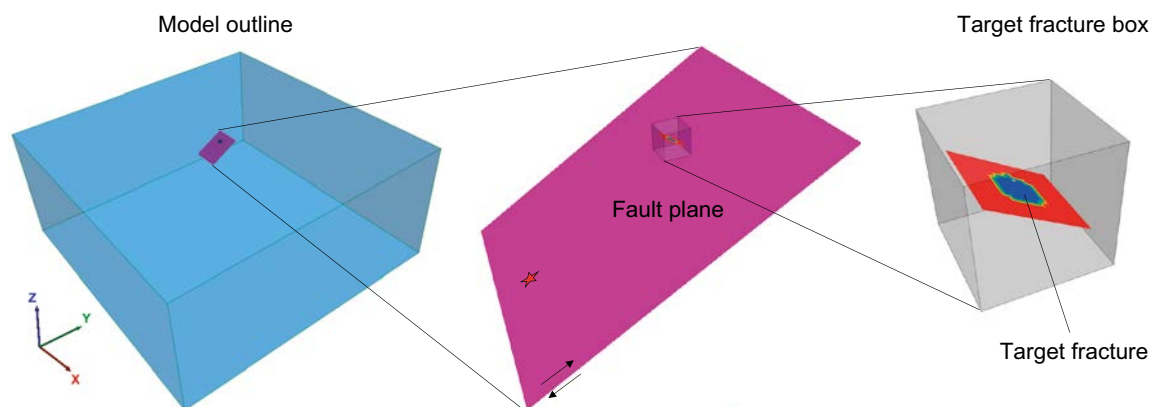


Figure B-3. Large-scale model geometry. The star indicates the hypocentre and the arrows indicate the sense of fault slip.

B2.2 Stresses and properties

Since we simulate a thrust faulting earthquake, we define a reverse type initial stress field. Our stress field is based on the notion of data indicating that the intraplate crust is in a state of frictional failure equilibrium on optimally oriented faults (Zoback and Townend 2001). We construct a stress field using a Mohr-Coulomb failure criterion (see Jaeger and Cook 1979) according to

$$\frac{\sigma_1 - P}{\sigma_3 - P} = (\sqrt{\mu^2 + 1} + \mu)^2 \quad (\text{B-1})$$

Here σ_1 is the major principal stress, σ_3 the minor principal stress, P is the pore pressure and μ is the friction coefficient. Equation (B-1) involves only the major and minor principal stress components. The intermediate principal stress component, σ_2 , is constrained by (after Gephart and Forsyth 1984):

$$R = \frac{\sigma_1 - \sigma_2}{\sigma_1 - \sigma_3} \quad (\text{B-2})$$

Using Equations (B-1) and (B-2), a reverse stress field can be constructed according to

$$\begin{aligned} \sigma_1 &= A(\sigma_3 - P) + P = \sigma_H \\ \sigma_2 &= \sigma_1(1 - R) + R\sigma_3 = \sigma_h, \\ \sigma_3 &= \sigma_v \end{aligned} \quad (\text{B-3})$$

with $A = (\sqrt{\mu^2 + 1} + \mu)^2$. We assume σ_3 to be vertical and to correspond to the weight of the rock overburden, the friction coefficient to be $\mu = 0.6$, in accordance with data of several rock types (Byerlee 1978), $R = 0.5$ and hydrostatic pore pressure. The principal stress components are plotted in Figure B-4. We align the stresses with the model axes such that $\sigma_{xx} = \sigma_2$, $\sigma_{yy} = \sigma_1$ and $\sigma_{zz} = \sigma_3$.

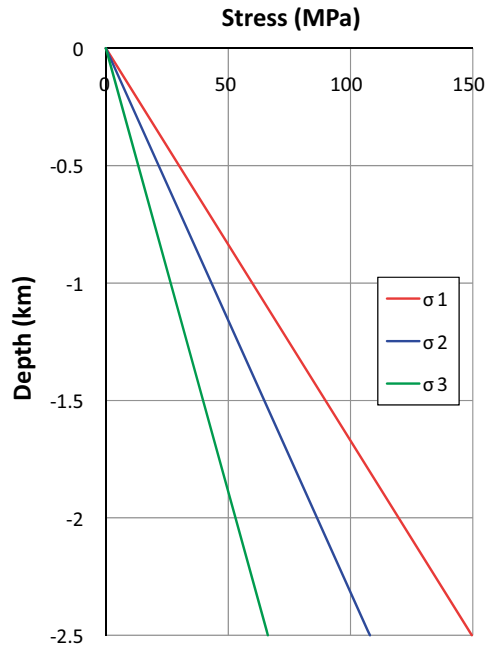


Figure B-4. Initial stresses.

We model the rock mass as a linear elastic, isotropic and homogeneous continuum. The discontinuities (the primary fault and target fracture) are represented by planar joint planes that respond to loads according to an ideal elasto-plastic material model with constant stiffness and a Coulomb failure criterion. The material property parameter values are given in Table B-1.

Table B-1. Material property values.

Component	Parameter	Value
Rock mass	Young's modulus, E (GPa)	70
	Poisson's ratio, ν (-)	0.24
	Density, ρ (kg/m ³)	2700
	P wave speed, V_p (km/s)	5.5
	S wave speed, V_s (km/s)	3.2
Target fracture	Friction angle, ϕ (°)	30
	Cohesion, c (MPa)	0
	Normal stiffness, k_n (GPa/m)	50
	Shear stiffness, k_s (GPa/m)	50
Fault plane	Static friction coefficient, μ_s (-)	0.71
	Dynamic friction coefficient, μ_d (-)	0.43
	Slip-weakening distance, d_c (m)	0.1
	Normal stiffness, k_n (GPa/m)	10
	Shear stiffness, k_s (GPa/m)	10

For the fault rupture simulation, we model the strength break-down according to the widely used slip-weakening law (Ida 1972), where the fault friction coefficient μ is modelled as a linear function of slip u over a slip-weakening distance d_c , i.e.

$$\mu = \begin{cases} \mu_d + (\mu_s - \mu_d) \left(1 - \frac{u}{d_c}\right) & u \leq d_c \\ \mu_d & u > d_c \end{cases} \quad (\text{B-4})$$

To initiate the rupture, we adopt an approach described by Bizzarri (2010). Starting at the hypocentre (Figure B-3, middle) we enforce a radially expanding rupture to propagate at a constant rupture speed v_{force} within a nucleation region Σ_{nucl} . We schematically assume v_{force} to be 50 % of the shear wave speed V_s of the surrounding medium. The friction coefficient is determined by

$$\mu = \begin{cases} \mu_{nucl} = \min\{\mu^{SW}, \mu^{tw}\} & \forall (x, z) \in \Sigma_{nucl} \\ \mu^{SW} & \forall (x, z) \notin \Sigma_{nucl} \end{cases} \quad (\text{B-5})$$

where μ^{SW} is determined by Equation (B-4) and μ^{tw} is given by

$$\mu^{tw} = \begin{cases} \mu_s - (\mu_s - \mu_d) \frac{(t - t_{force})}{t_0} & t - t_{force} < t_0 \\ \mu_d & t - t_{force} \geq t_0 \end{cases} \quad (\text{B-6})$$

Here, t_{force} is the time of rupture initiation and t_0 is the time over which the strength is ramped down from μ_s to μ_d , here set at 0.1 s. At some time during the initiation process, the slip-weakening (SW) law (Equation (B-4)) takes over and the rupture propagates spontaneously.

To obtain stronger secondary stress effects, and thereby larger target fracture displacement, we assign a high value of the dynamic friction coefficient within a circular asperity region close to the target fracture. We want the model to generate strong secondary effects because it makes it easier to see if the DFN has any significant impact on the target fracture displacement. The asperity region has a radius of $a = 300$ m and is located with its centre at 850 m depth. The dynamic friction coefficient within the asperity is varied with radial distance r according to Figure B-5. To obtain a significant effect on the fault slip and on the corresponding secondary effects, we schematically set the strength to an extremely high value.

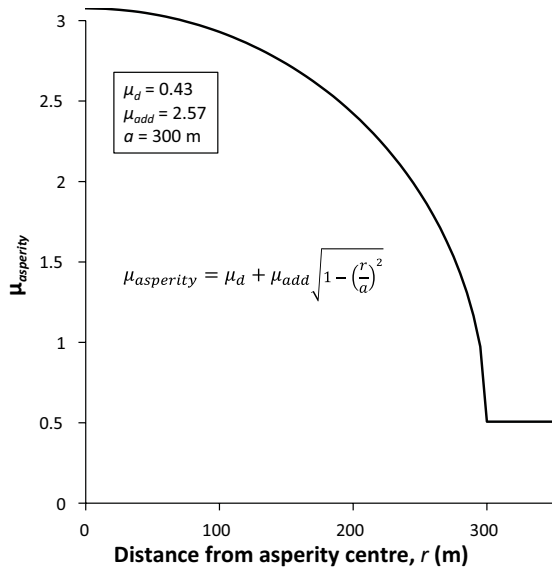


Figure B-5. Dynamic friction coefficient within fault asperity.

B2.3 Calculation sequence

The calculation sequence comprises two phases, the quasi-static phase and the dynamic phase.

During the quasi-static phase, initial stresses are applied (Figure B-4), the primary fault and the target fracture are assigned their properties and the model is allowed to reach static equilibrium under gravity. The bottom boundary is locked for displacements in the z -direction, the vertical boundaries are locked in the x - and y -directions and the top boundary is kept free. The static equilibrium state is the point of departure for the following dynamic phase.

During the dynamic phase, the top boundary is kept free and allows for surface reflections, while the other boundaries are redefined to be viscous, i.e. non-reflecting. The earthquake rupture is initiated and propagated until the entire fault plane has ruptured. The target fracture shear displacement at the fracture centre as well as the x -, y -, and z -displacements at the boundary of the target fracture box (Figure B-3, right) are monitored and recorded.

B2.4 Fault response

The synthetic earthquake generates an average stress drop of about 5.5 MPa, an average slip of 0.53 m and a moment magnitude of M_w 5.6 over a rupture area of 20 km². The relation between rupture area and moment magnitude is in accordance with database regressions based on crustal earthquakes (Leonard 2010). The distributions of slip and of peak slip velocity are shown in Figure B-6. Due to the breaching of the ground surface there is a low slip resistance in the upper parts of the fault and the largest slip is developed in a region at shallow depth. However, the slip is clearly influenced by the high dynamic friction coefficient assigned within the circular area close to the target fracture. The increased fault strength also clearly influences the slip velocities, as seen in the right plot. In that plot, we also see that the slip velocities are in the range 2–3 m/s over a major part of the fault plane. These velocities are in accordance with slip velocities inferred from recorded data (e.g. Wald and Heaton 1994, Ma et al. 2003).

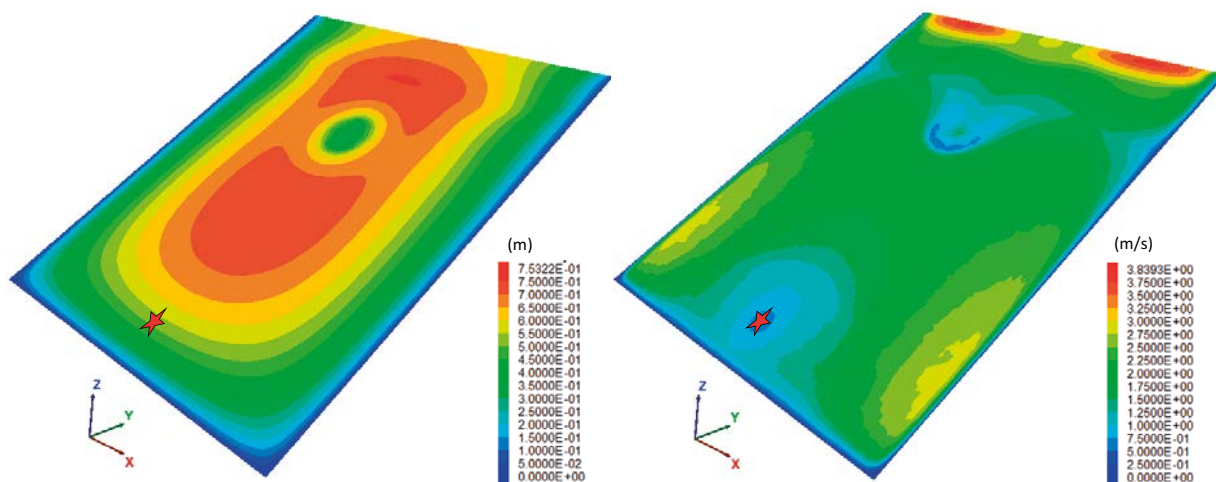


Figure B-6. Fault slip (left) and peak slip velocity (right). The stars indicate the hypocentre.

B3 Near-field models

In this section, we investigate how seismically induced fracture shear displacements along an optimally oriented target fracture are influenced by inelastic movements along surrounding, smaller fractures.

B3.1 Description of 3DEC models

Model geometry

The outline of the near-field model is a cube with side-length 400 m. It is subdivided into two regions: an outer region (essentially some “padding” surrounding the fracture network) and an inner region (a cube with side-length 300 m) in which the target fracture and a discrete fracture network (DFN) are implemented, cf. Figure B-7a. The target fracture is located at the centre of the model and dips 30° along the positive y -axis. As in the large-scale model the target fracture is circular and has a radius of 75 m.

The base-case fracture orientations, sizes and intensities are based on one realisation¹ of the DFN model for the Forsmark site (Fox et al. 2007). It consists of 3 701 fractures (Figure B-8) with radii in the range 10.0 m to 72.6 m located within a cube of side-length 300 m. Noting that it is generally difficult to implement a fracture network consisting of several thousands of fractures in a 3DEC model (e.g. Suikkanen et al. 2016), we limit the DFN fractures to be included in the numerical model to fractures that (1) have a radius of at least 15 m and (2) are fully contained within the 300 m inner cube, i.e. no truncated fractures are considered (cf. Figure B-7a). The DFN fracture planes are inserted into the 3DEC model one by one starting with the largest fracture and continuing in descending order. Any plane that causes an error message in 3DEC is omitted from the model. The simplified Forsmark DFN implemented in 3DEC consists of 704 fractures (see Figure B-7b)² and has a volumetric fracture intensity (P_{32} = total fracture area per unit rock mass volume) of 0.043 m²/m³. The corresponding P_{32} value of the original Forsmark DFN for fractures sizes in the range 15–75 m is 0.064 m²/m³.

As shown in Figure B-7b and Figure B-8, the majority of the Forsmark fractures are either steeply dipping or sub-horizontal. Results from a previous study indicate, however, that fractures with medium dip (30–50°, i.e. those with the lowest initial stability margin) are the ones that slip by the largest amounts during an earthquake (Fälth et al. 2016). We quantify the stability margin in terms of the Coulomb Failure Stress (CFS) where values below zero indicate stability (e.g. Harris 1998). To assess the impact of a fracture network with a higher frequency of fractures with smaller stability margins, we construct a generic DFN model (using the built-in DFN-generator in 3DEC) with uniform size and orientation distributions to be used alongside the site-specific DFN for comparison.

¹ The realization of the Forsmark DFN “r = 10–75 m.fab” was modelled and provided by Raymond Munier, SKB.

² One fracture caused an error message and was omitted from the Forsmark 3DEC model.

The starting point is one realisation of a Uniform DFN with fracture radii in the range 15–71.2 m (the same min-max radius interval as in Figure B-7b). The P_{32} is set, using a trial-and-error method, at $0.097 \text{ m}^2/\text{m}^3$ to achieve the same P_{32} after simplification as in the Forsmark 3DEC-model. The Uniform DFN implemented in 3DEC consists of 247 fractures (see Figure B-7c) and has a P_{32} of $0.043 \text{ m}^2/\text{m}^3$.

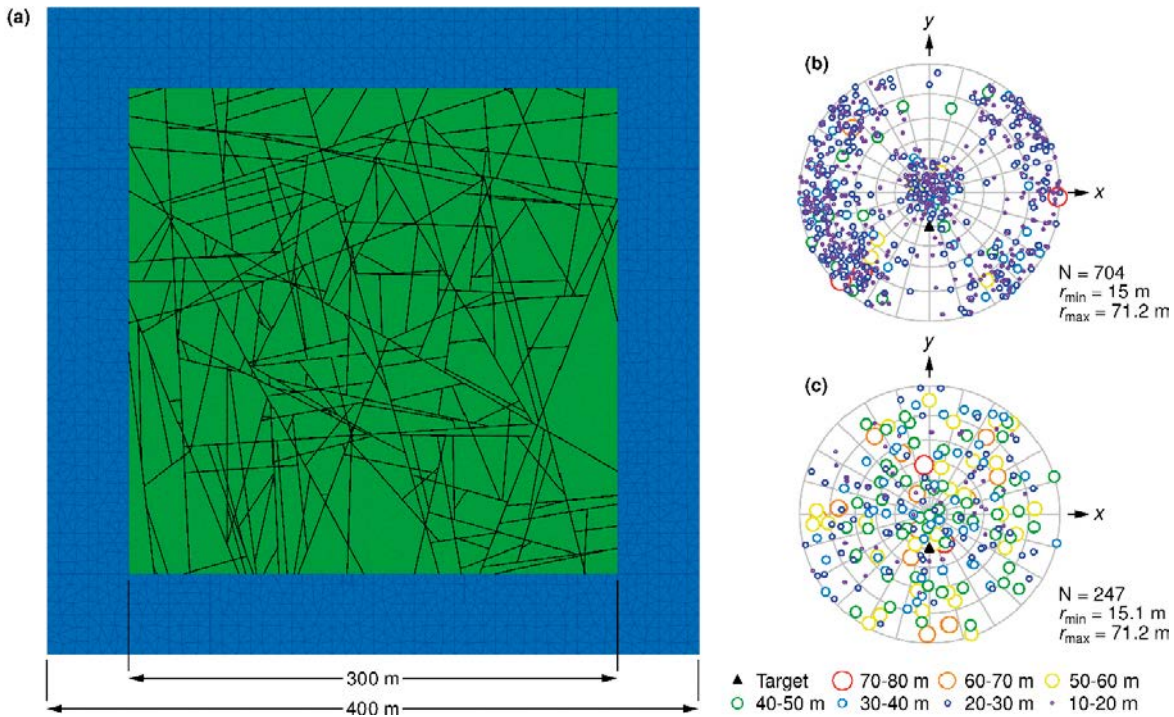


Figure B-7. (a) Cross-section of the numerical model with the Forsmark DFN. (b) and (c) Lower hemisphere projections of the Forsmark and Uniform DFN models, respectively.

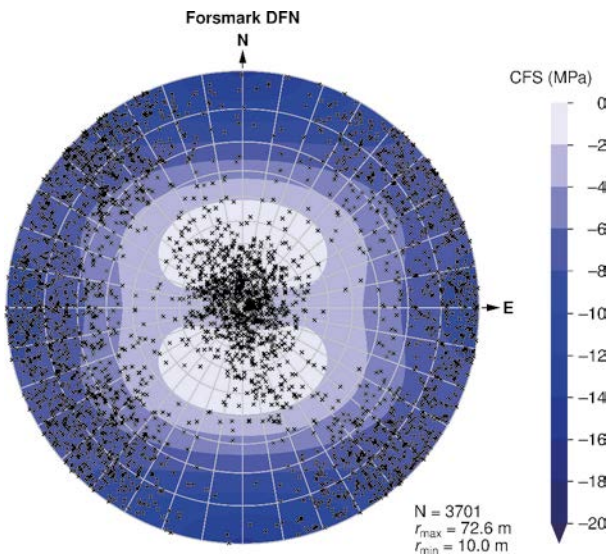


Figure B-8. Lower hemisphere equal angle projection of the Forsmark DFN superimposed on a CFS plot assuming a state of stress at 500 m depth as in Figure B-4, hydrostatic pore pressure and shear strength parameter values as in Table B-2.

The models are discretized with tetrahedral finite-difference elements. We select the edge-lengths of the elements based on the radii of the fractures to achieve a reasonable discretization of all fractures (the target fracture as well as the DFN fractures). The near-field models are, therefore, more finely meshed than the corresponding box in the large-scale model. The model is discretised using finite-difference elements with edge lengths in the range 3.75–8 m. The number of finite-difference elements in the Forsmark model is about 4 millions whereas the corresponding number of elements in the Uniform model about is about 2.9 millions.

Input data

Material properties

The intact rock between and surrounding the joint planes is represented by a homogenous, isotropic and linear elastic material with parameter values set according to the site descriptive model for Forsmark (Glamheden et al. 2007). The fractures are assigned an elastoplastic constitutive relation with constant normal and shear stiffnesses, zero tensile strength and shear strength according to a Mohr-Coulomb criterion. In previous modelling (e.g. Fälth et al. 2016), the fractures have been assigned low stiffness values (~10 GPa/m) to reduce numerical noise and to achieve an acceptable timestep, i.e. a reasonable total calculation time. However, given the representation of fractures in 3DEC as the interfaces between blocks, the models contain more fracture surface area than that given by the DFN models. To minimize the impact on the elastic properties of the rock mass (cf. Brady and Brown 1995, p 136), the normal and shear stiffnesses are set at 100 GPa/m. The shear strength (friction angle and cohesion) are set in agreement with lower bound estimates for the fractures in fracture domain FFM01 (Glamheden et al. 2007). The parameters used in the study are summarized in Table 2.

Table B-2. Material property values. Alternative friction angles assigned to the DFN are shown in brackets.

Component	Parameter	Value
Rock mass	Young's modulus, E (GPa)	70
	Poisson's ratio, ν (-)	0.24
	Density, ρ (kg/m ³)	2700
Fractures	Friction angle, ϕ (°)	30 (40;20;10;5)
	Cohesion, c (MPa)	0
	Normal stiffness, k_n (GPa/m)	100
	Shear stiffness, k_s (GPa/m)	100

In situ stress and groundwater pressure

Contrary to the large-scale models, all spatial variations (e.g. due to gravity) in the *in situ* stress field and groundwater pressure are ignored. The stresses and groundwater pressure are assigned uniformly within the model corresponding to a depth of 500 m (cf. Figure B-4 and Table B-3).

Table B-3. Initial state of stress and groundwater pressure.

$\sigma_1 = \sigma_{yy}$ (MPa)	$\sigma_2 = \sigma_{xx}$ (MPa)	$\sigma_3 = \sigma_{zz}$ (MPa)	P (MPa)
29.9	21.6	13.2	4.9

Calculation sequence and boundary conditions

Similarly, to the large-scale modelling presented in Section 1.2, the near-field modelling comprises two phases: a static phase followed by a dynamic phase.

During the static phase, the boundaries are locked in all directions and the model is allowed to reach static equilibrium. To avoid any non-physical movements along the fractures resulting from unbalanced forces at the beginning of a calculation cycle, the shear strength (cohesion) is ramped

down from an initially high value to zero in small steps (cf. Lönnqvist and Hökmark 2015b). The static equilibrium provides the initial conditions for the dynamic phase. Any aseismic displacements occurring during the static phase are set to zero at the start of the dynamic phase.

During the dynamic phase, the combined effects of the static stress redistributions (e.g. around the fault asperity and around the fault's edges) and of the stress waves generated by the slipping earthquake fault are simulated by controlling the movements of the model's boundaries according to deformation histories imported from the large-scale model. Note that these boundary conditions represent the case of a single target fracture embedded in a linear elastic material. For the purpose of this study, we assume that these deformation histories are representative of the deformations of the system regardless of the choice of DFN model, P_{32} or parameter values assigned to the DFN, i.e. regardless of whether slip along the DFN-fractures effectively makes the material surrounding the target fracture weaker and more compliant. Details regarding the approach to import and assign boundary conditions are presented in the sections at the end of this appendix; a summary is presented here:

- Each of the outer boundaries is divided into 64 equally sized squares (2500 m^2) and labelled 1 to 64 as shown in Figure B-9a.
- For each square, unique displacement histories in the x -, y - and z -direction are imported from the large-scale model. An example is shown in Figure B-9b.
- The displacement histories are converted into velocity histories as shown in Figure B-9c. The velocities are subsequently assigned uniformly (without interpolation) to the square corresponding to the original displacement history.

Timestep

A model with a complex geometry containing small finite-difference elements requires very small timesteps for numerical stability (Itasca 2013). As a result, dynamic models can be very time-consuming. 3DEC also allows for the user to manually set a timestep that is larger than the automatically determined one. The code then calculates and adds sufficient mass to certain grid points to compensate and to achieve numerical stability (Itasca 2013). Based on scoping calculations (see Figure B-20), it appears that up to about 1‰ of mass can be added to a model before the results are affected. To speed-up the calculation time, we, therefore, increase the timestep from the default values to $3.2 \times 10^{-5} \text{ s}$ for the Forsmark DFN model and to $3.5 \times 10^{-5} \text{ s}$ for the Uniform DFN model resulting in an increase in mass by 1.05‰ and 1.01‰, respectively.

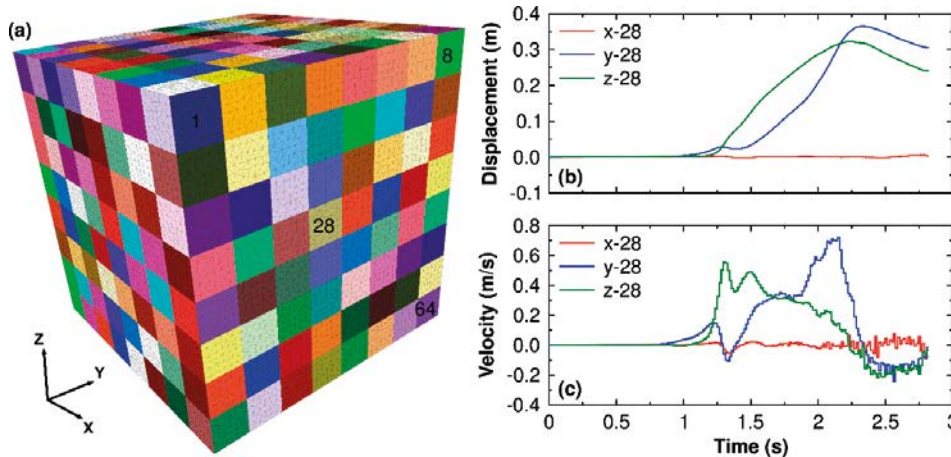


Figure B-9. (a) Division of the near-field model's outer boundaries into squares for assignment of boundary conditions. (b) Example of displacement histories obtained from the large-scale model corresponding to the position on the positive x -side marked "28". (c) Velocity boundary conditions converted from the displacement histories shown in sub-figure (b).

B3.1 Results

Influence of size/orientation distributions and fracture intensity

To investigate the influence of the volumetric intensity (P_{32}) of the fracture network, we analyse the models with different subsets of the DFNs mechanically active as shown in Table B-4. Note that all DFN fractures are geometrically included in the models; fractures that do not contribute to the P_{32} are assigned fictitious high-strength properties to prevent slip.

Table B-4. Volumetric intensity (P_{32}) of the DFN (excluding the target fracture). The number of mechanically active fractures is given in brackets.

Radius interval	Forsmark, P_{32} (m^2/m^3)	Uniform, P_{32} (m^2/m^3)
≥ 70 m	0.002 (3)	0.001 (2)
≥ 60 m	0.003 (5)	0.008 (15)
≥ 50 m	0.005 (11)	0.018 (45)
≥ 40 m	0.008 (26)	0.031 (98)
≥ 30 m	0.013 (69)	0.037 (143)
≥ 20 m	0.030 (318)	0.042 (207)
≥ 10 m (all fractures)	0.043 (704)	0.043 (247)

At the end of analysis, we register the maximum shear displacement along each fracture. Since the maximum shear displacement may be influenced by local stress disturbances along intersecting fractures, we also calculate the average shear displacements.

Figure B-10 shows the induced maximum and average shear displacements along the target fracture as functions of P_{32} (sub-figure 'a') and as functions of the truncation radius R_0 (sub-figure 'b') for the Forsmark DFN and for the Uniform DFN. Here, a P_{32} of zero represents the isolated fracture. The response of the target fracture can be summarized as follows:

- The induced slip along the target fracture is only marginally affected by the introduction of a fracture network with characteristics as in the Forsmark DFN.
- The induced slip along the target fracture embedded in the Uniform DFN displays a decreasing trend with decreasing truncation radius and corresponding increase of P_{32} (more pronounced in the average slip than in the maximum slip). When all fractures in the DFN are mechanically active ($P_{32} = 0.043 \text{ m}^2/\text{m}^3$), the reduction in the maximum slip is about 10 % which is slightly less than in the scoping calculations presented in Figure B-1.

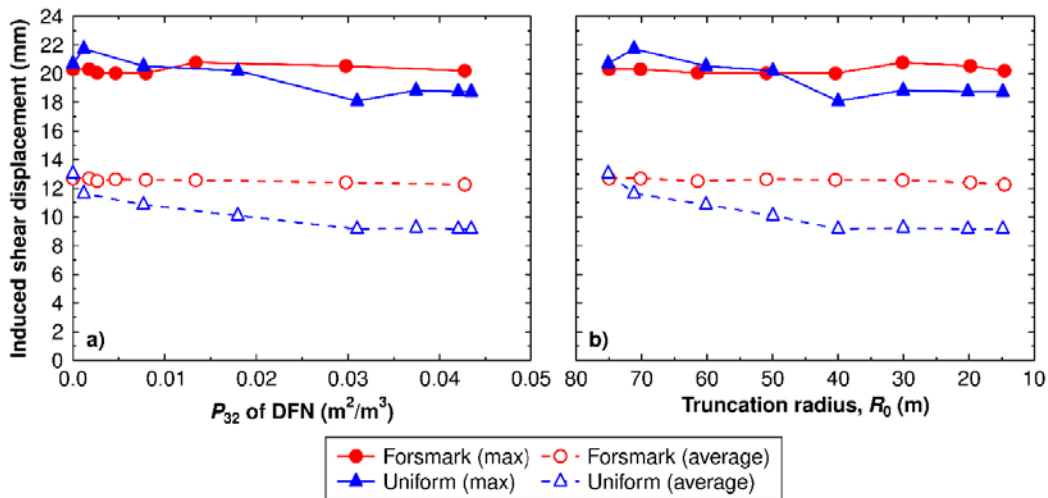


Figure B-10. Maximum and average induced shear displacement along the target fracture as a function of volumetric intensity P_{32} (left) and as a function of truncation radius R_0 (right) of the surrounding DFN. A P_{32} of zero represents the isolated target fracture.

The differences between the two DFN models are more clearly observed in Figure B-11 and Figure B-12 where the induced maximum shear displacements for both the target fracture and the individual DFN fractures are presented as functions of the fracture radius. The majority of the Forsmark DFN fractures are small and slip by small amounts. For example, only 3 out of 704 fractures slipped more than 10 mm (cf. Figure B-11g). The Uniform DFN has a higher frequency of a combination of large and favourably oriented fractures. Consequently, a larger proportion of the fractures slip by larger amounts (cf. Figure B-12).

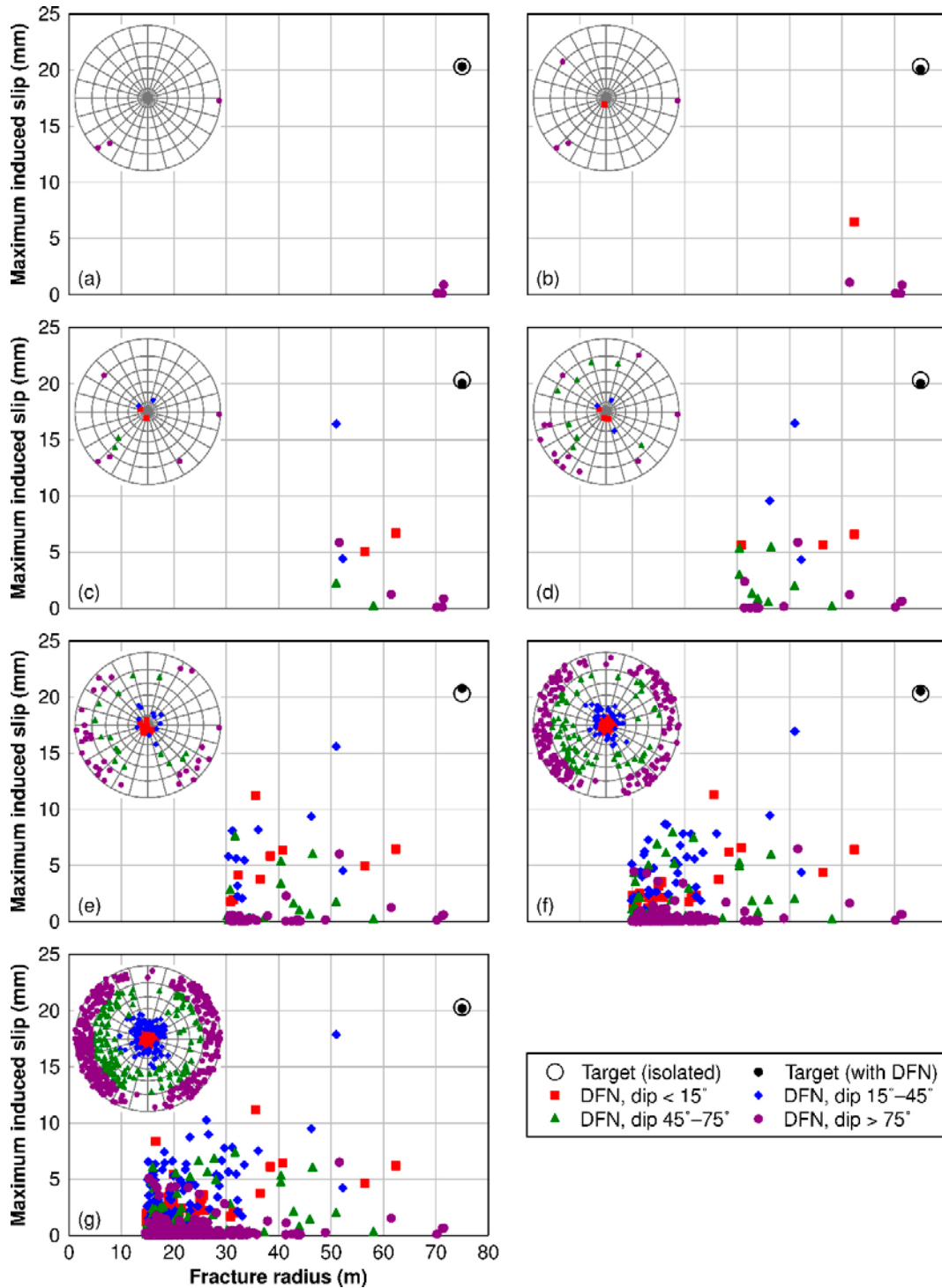


Figure B-11. Maximum induced shear displacements in the Forsmark model along the target fracture and along the DFN fracture as functions of the fracture radius for different radius-intervals mechanically active (a) $r \geq 70$ m, (b) $r \geq 60$ m, (c) $r \geq 50$ m, (d) $r \geq 40$ m, (e) $r \geq 30$ m, (f) $r \geq 20$ m and (g) $r \geq 10$ m (all fractures). Inset to each sub-figure shows the orientations of the mechanically active DFN fractures.

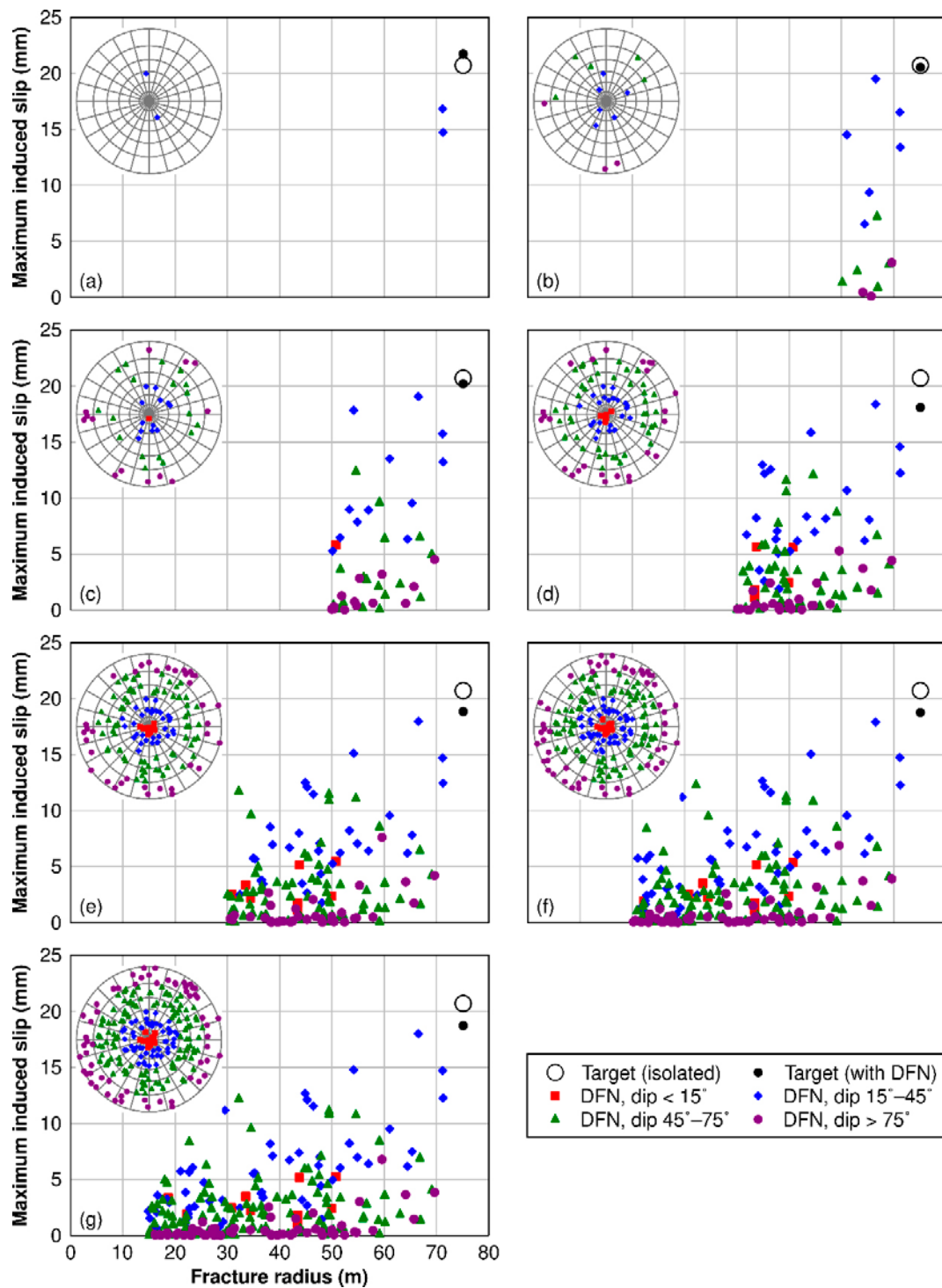


Figure B-12. Maximum induced shear displacements in the Uniform model along the target fracture and along the DFN fracture as functions of the fracture radius for different radius-intervals mechanically active (a) $r \geq 70$ m, (b) $r \geq 60$ m, (c) $r \geq 50$ m, (d) $r \geq 40$ m, (e) $r \geq 30$ m, (f) $r \geq 20$ m and (g) $r \geq 10$ m (all fractures). Inset to each sub-figure shows the orientations of the mechanically active DFN fractures.

Influence of DFN shear strength

In this section, we investigate to what extent the shear strength of the surrounding fracture network influences the induced shear displacements along the target fracture. The starting points are the base-case models presented in the previous section (cf. Figure B-10) with all DFN fractures mechanically active. Alternative friction angle values of 40°, 20°, 10° and 5° are tested. The friction angle assigned to the target fracture is kept at 30° in all models. The isolated case, which corresponds to infinite strength of the DFN, is plotted in the graph below as having a friction angle of 90°. Figure B-13 shows the results:

- The impact of the Forsmark DFN on the slip of the target fracture is small regardless of the value of the friction angle assigned to the DFN-fractures.
- The impact of the Uniform DFN on the slip of the target fracture is very sensitive to the choice of value for the friction angle assigned to the DFN-fractures; an increase of 10° (from the base-case value) in the friction angle suppresses the influence of the DFN very efficiently and the target fracture responds to loading approximately as in the isolated case; a corresponding reduction of 10° in the friction angle reduces the induced maximum shear displacement to a little over 50 % of the value in the isolated case.

Figure B-14 and Figure B-15 show the maximum shear displacements along the target fracture as well as for the DFN fractures as functions of the fracture radius for the Forsmark DFN and for the Uniform DFN, respectively. In these models, all DFN fractures are mechanically active. The inset to each sub-figure shows the initial stability margin expressed in terms of *CFS*. Fractures with an initial *CFS* > 0 MPa will have slipped aseismically during the static phase and thereby relaxed the shear stresses. Although the impact of reducing the shear strength of the DFN is observed for both DFN models, the impact is greatest for the Uniform DFN which has a higher frequency of large and favourably oriented fractures.

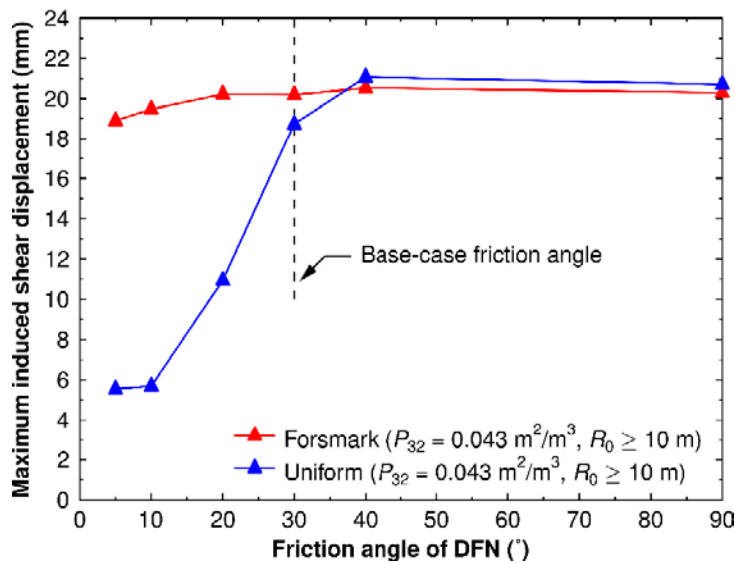


Figure B-13. Maximum induced shear displacement along the target fracture as a function of the friction angle of the DFN. The friction angle of the target fracture is 30°.

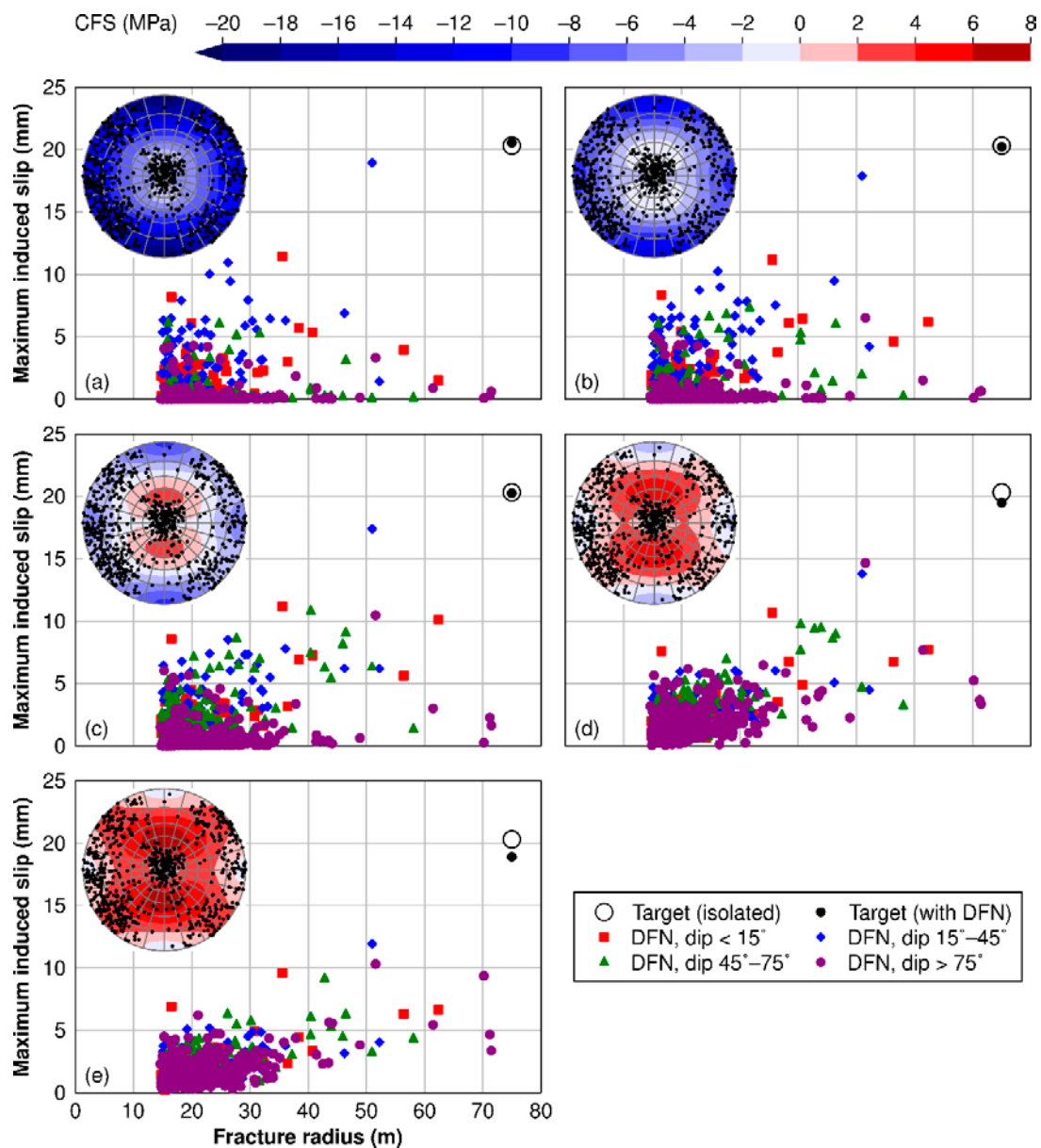


Figure B-14. Maximum induced shear displacements in the Forsmark model along the target fracture and along the DFN fractures as functions of the fracture radius for different values of the friction angle assigned to the DFN (a) 40°, (b) 30° (base-case), (c) 20°, (d) 10° and (e) 5°. Inset to each sub-figure shows the initial stability margin.

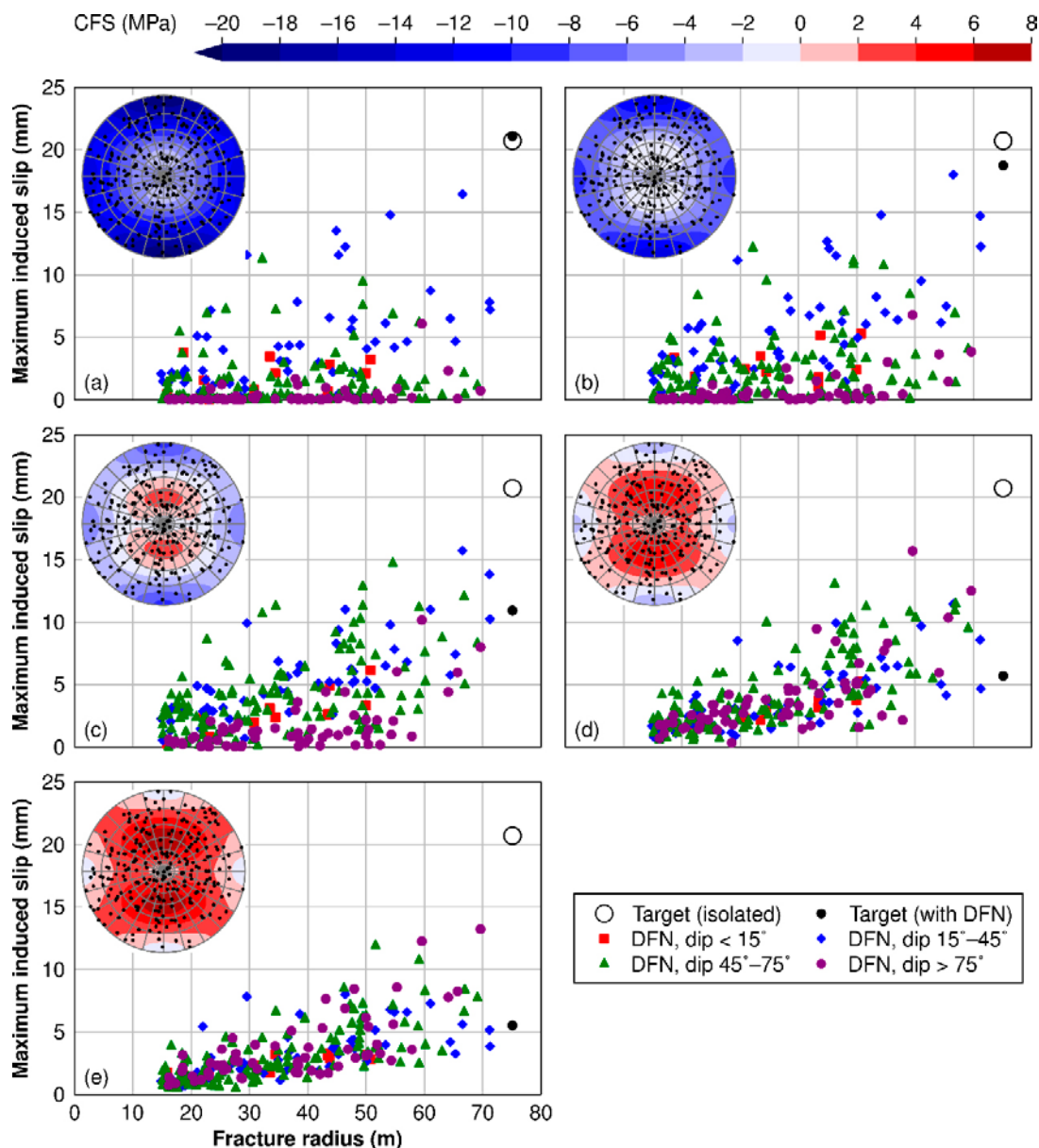


Figure B-15. Maximum induced shear displacements in the Uniform model along the target fracture and along the DFN fractures as functions of the fracture radius for different values of the friction angle assigned to the DFN (a) 40°, (b) 30° (base-case), (c) 20°, (d) 10° and (e) 5°. Inset to each sub-figure shows the initial stability margin.

B4 Conclusions and final remarks

In this study, we have analysed the response of a large and favourably oriented off-fault (target) fracture to the dynamic stress waves generated by a nearby magnitude M_w 5.6 thrust-faulting earthquake rupturing a surface breaching and gently dipping fault. The initial stress field, which controls the stability of the earthquake fault and of the fractures, is of reverse type and thus qualitatively in agreement with the present-day stress field at the Forsmark site (Glamheden et al. 2007) as well as with the stresses expected during end glacial conditions (Lund et al. 2009). This means that the dip angle range (20°–60°) for which the lowest fracture stabilities are found (cf. Figure B-8) would be the same at Forsmark.

We examine how slip on a fracture network possibly could reduce the load on the target fracture and hence the induced co-seismic slip. We test the impact of two fracture networks:

- Network based on a realisation of the DFN for the Forsmark site.
- Network based on a realisation of a generic DFN with uniform distribution of fracture sizes as well as of fracture orientations.

The results demonstrate that inelastic movements along a network of fractures, under certain conditions, will reduce the slip along the target fracture. However, for the impact to be significant, we have to apply the generic DFN model, i.e. the frequency of large and favourably oriented fractures needs to be high compared with that found at repository depth at the Forsmark site (Fox et al. 2007, Glamheden et al. 2007). Given the DFN model of the Forsmark site, our results indicate that there are too few large and favourably oriented fractures for the network to give any significant reduction of target fracture slip.

Here, we have considered only one realisation of the Forsmark DFN and one realisation of the generic DFN. Hence, we cannot totally exclude the possibility that other realisations would generate slightly different results. However, since the trend in the present results is logical and systematic, given the distributions of fracture size and fracture orientation, there are good reasons to believe that other realisations of the same DFNs will generate similar results as those presented here. In addition, we should point out that here we assume that all fractures are planar. This is not the case for real fractures (e.g. Candela et al. 2012). Hence, the stability of the network fractures in our models should be underestimated, rather than overestimated.

In these models, the relevance of using the same set of velocity boundary conditions in the near-field models regardless of fracture intensity or parameter values assigned to the DFN may need further investigation in future work. However, for a fracture network similar to that at the Forsmark site (Fox et al. 2007), i.e. one that consists primarily of small and, for slip, unfavourably oriented fractures, the impact of inelastic fracture movements on the rock mass mechanical response is likely to be small.

The general conclusion of this study is that, given the schematic method of simulating hypothetical earthquakes on simplistically represented fault planes used in the numerous studies referred to here, it cannot be assumed that slip along potentially critical fractures would be limited by slip along neighbouring discrete fractures.

Additional material

FISH functions for import and assignment of boundary conditions

For large and complex problems, it is advantageous to combine models with different sizes and resolutions. The approach whereby e.g. displacements obtained from the interior of a large model are used as mechanical boundary conditions to smaller and more detailed models has routinely been used in quasi-static thermo-mechanical models of a KBS-3 repository (e.g. Fälvh and Hökmark 2006b, Hökmark et al. 2010, Suikkanen et al. 2016). In this section, we present an approach to transfer boundary conditions in dynamic earthquake models.

Description of method to assign boundary conditions

Export of data from the large-scale model

Displacements were recorded in the large-scale model (cf. Section 1.2) at 64 uniformly spaced points on each side of the cube corresponding to the near-field model's boundaries as shown in Figure B-16 and transferred to data files (one file for each side of the cube).

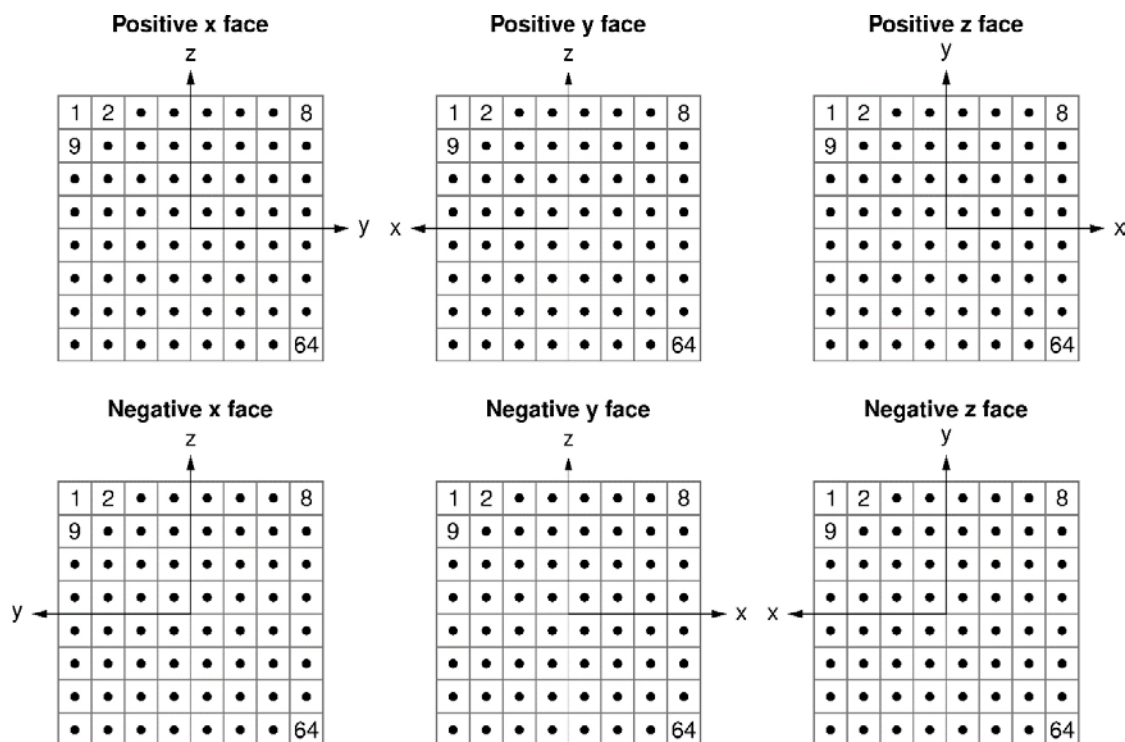


Figure B-16. Description and numbering of the sides of the near-field model's boundaries for assignment of boundary conditions. The dots mark the locations where the displacements were recorded in the large-scale model.

Import of data

The displacements are imported into the near-field model using the *FISH* functions presented in Table B-5. Note that the output from the large-scale model in this study was recorded with an unnecessarily high frequency (~0.3 ms). We have, therefore, used every 50th data point from the data sets as boundary conditions.

Table B-5. *FISH* functions for import of boundary conditions.

```
def var
  mylength1 = 64 ; # of spatial datapoints
  mylength2 = 9152 ; # of temporal datapoints
end
def arrays
  array mytime(mylength2)

  array xneg(mylength2)
  array xpos(mylength2)

  array yneg(mylength2)
  array ypos(mylength2)

  array zneg(mylength2)
  array zpos(mylength2)
end
```

```

def import_bc

    o_status=open('time-hist.dat',0,1)
    r_status=read(mytime,mylength2)
    c_status=close

    o_status=open('xneg-hist.dat',0,1)
    r_status=read(xneg,mylength2)
    c_status=close

    o_status=open('xpos-hist.dat',0,1)
    r_status=read(xpos,mylength2)
    c_status=close

    o_status=open('yneg-hist.dat',0,1)
    r_status=read(yneg,mylength2)
    c_status=close

    o_status=open('ypos-hist.dat',0,1)
    r_status=read(ypos,mylength2)
    c_status=close

    o_status=open('zneg-hist.dat',0,1)
    r_status=read(zneg,mylength2)
    c_status=close

    o_status=open('zpos-hist.dat',0,1)
    r_status=read(zpos,mylength2)
    c_status=close

    myarray0 = get_array(mylength2)

    myarray1 = get_array(mylength2,mylength1)
    myarray2 = get_array(mylength2,mylength1)
    myarray3 = get_array(mylength2,mylength1)
    myarray4 = get_array(mylength2,mylength1)
    myarray5 = get_array(mylength2,mylength1)
    myarray6 = get_array(mylength2,mylength1)

    loop j (1,mylength1)

```

```

loop i (1,183)

  myarray0(i) = mytime(50*i) ; import every 50th datapoint

  xvel = parse(zpos(50*i),1+3*(j-1))
  yvel = parse(zpos(50*i),2+3*(j-1))
  zvel = parse(zpos(50*i),3+3*(j-1))
  myarray1(i,j) = vector(xvel,yvel,zvel)

  xvel = parse(xneg(50*i),1+3*(j-1))
  yvel = parse(xneg(50*i),2+3*(j-1))
  zvel = parse(xneg(50*i),3+3*(j-1))
  myarray2(i,j) = vector(xvel,yvel,zvel)

  xvel = parse(xpos(50*i),1+3*(j-1))
  yvel = parse(xpos(50*i),2+3*(j-1))
  zvel = parse(xpos(50*i),3+3*(j-1))
  myarray3(i,j) = vector(xvel,yvel,zvel)

  xvel = parse(yneg(50*i),1+3*(j-1))
  yvel = parse(yneg(50*i),2+3*(j-1))
  zvel = parse(yneg(50*i),3+3*(j-1))
  myarray4(i,j) = vector(xvel,yvel,zvel)

  xvel = parse(ypos(50*i),1+3*(j-1))
  yvel = parse(ypos(50*i),2+3*(j-1))
  zvel = parse(ypos(50*i),3+3*(j-1))
  myarray5(i,j) = vector(xvel,yvel,zvel)

  xvel = parse(zneg(50*i),1+3*(j-1))
  yvel = parse(zneg(50*i),2+3*(j-1))
  zvel = parse(zneg(50*i),3+3*(j-1))
  myarray6(i,j) = vector(xvel,yvel,zvel)

endloop
endloop

void = lose_array(mytime)
void = lose_array(zpos)
void = lose_array(xneg)
void = lose_array(xpos)
void = lose_array(yneg)
void = lose_array(ypos)
void = lose_array(zneg)

end

```

Assignment of boundary conditions

The movements of the boundaries are controlled by velocity-type boundary conditions obtained from the displacements imported from the large-scale model. For the purpose of this study, we assume that the boundary displacements increase/decrease linearly between two temporal data points, i.e. that the velocity is constant between the two data points. Here, each velocity history is assigned without interpolation to the associated square on the model's boundaries as shown in Figure B-16. The *FISH* functions used to convert the displacements to velocities and to assign them to the model's boundaries are presented in Table B-6.

Table B-6. FISH function for assignment of boundary conditions.

```
def find_bou_pos
  n = 0
  loop j (1,8)
    loop i (1,8)
      n = n + 1
      command
        mark sreg [100+n] range x [-200+(i-1)*50] [-200+(i)*50] y [200-(j-1)*50] [200-(j)*50] z [199.9] [200.1] ; z-plus

        mark sreg [200+n] range x [-200.1] [-199.9] y [200-(i-1)*50] [200-(i)*50] z [200-(j-1)*50] [200-(j)*50] ; x-minus
        mark sreg [300+n] range x [199.9] [200.1] y [-200+(i-1)*50] [-200+(i)*50] z [200-(j-1)*50] [200-(j)*50] ; x-plus

        mark sreg [400+n] range x [-200+(i-1)*50] [-200+(i)*50] y [-200.1] [-199.9] z [200-(j-1)*50] [200-(j)*50] ; y-minus
        mark sreg [500+n] range x [200-(i-1)*50] [200-(i)*50] y [199.9] [200.1] z [200-(j-1)*50] [200-(j)*50] ; y-plus

        mark sreg [600+n] range x [200-(i-1)*50] [200-(i)*50] y [200-(j-1)*50] [200-(j)*50] z [-200.1] [-199.9] ; z-minus

      endcommand
    endloop
  endloop
end

def find_boundaries
  loop i (1,6)
    loop j (1,64)
      bh = block_head
      loop while bh # 0
        section
          bf = b_face(bh)
          loop while bf # 0
            if face_sreg(bf) == 100*i+j
              loop n (1,face_ngp(bf))
                gp = face_gp(bf,n)
                gp_extra(gp,1) = i
                gp_extra(gp,2) = j
                pp = uds_create(gp_pos(gp))
                uds_value(pp) = i
              endloop
            endif
            bf = face_next(bf)
            exit section
          endsection
        endloop
        bh = b_next(bh)
      endloop
    endloop
  endloop
end
```

```

def assign_bc(name)
  m = 0
  loop n (1,183)
    m = m+1
    t = float(myarray0(n))
    dt = t-time

    bh = bou_head
    loop while bh # 0

      gp = bou_gp(bh)

      myside = gp_extra(gp,1)
      mybox = gp_extra(gp,2)

      caseof myside

        case 1
          bou_vel(bh) = (myarray1(n,mybox)-gp_dis(gp))/(dt)
        case 2
          bou_vel(bh) = (myarray2(n,mybox)-gp_dis(gp))/(dt)
        case 3
          bou_vel(bh) = (myarray3(n,mybox)-gp_dis(gp))/(dt)
        case 4
          bou_vel(bh) = (myarray4(n,mybox)-gp_dis(gp))/(dt)
        case 5
          bou_vel(bh) = (myarray5(n,mybox)-gp_dis(gp))/(dt)
        case 6
          bou_vel(bh) = (myarray6(n,mybox)-gp_dis(gp))/(dt)
        endcase

      bh = bou_next(bh)
    endloop

    command
      solve time @dt rat 1e-10
    endcommand

    if m%5 == 0
      ii = out(m)
      filename = string(name)+'_Temp.sav'
      command
        save @filename
      endcommand
    endif

  endloop
end

```

Verification example

Description of 3DEC model

To verify that a small-scale model with imported boundary conditions can reproduce the results from the large-scale model, a simplified 3DEC model is built and analysed. The verification model consists of a cube with side length 400 m and contains one, isolated target fracture (cf. Figure B-17). The same base-case material properties and *in situ* stresses as described in Section 1.3.1 are used. A number of cases are tested:

- Mesh density in the region surrounding the target fracture (fine = 12.5 m; coarse = 20 m). The elements in the remaining parts of the model are assigned side-lengths of 25 m.
- Influence of gravity.
- Influence of fracture stiffness ($k_n = k_s = 50$ GPa/m or 100 GPa/m).

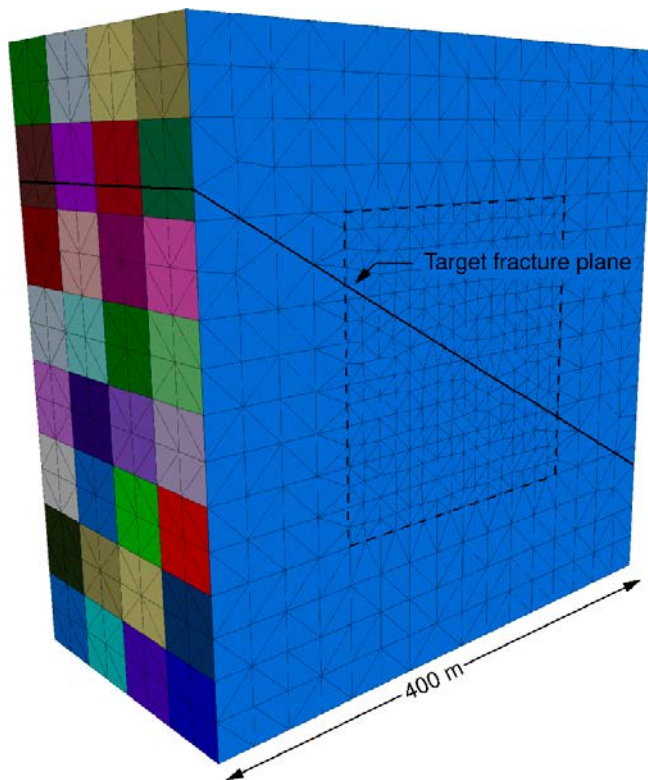


Figure B-17. Illustration of the verification-model geometry. Note that parts of the model is hidden to expose its interior. The model contains a region (marked with dashed lines) with increased mesh-density of either 12.5 m (shown in the figure) or 20 m. the remainder of the model is meshed with 25 m elements.

Results

To test the method, we compare shear displacements along the target fracture obtained from the large-scale model with corresponding results obtained from each of the near-field models (see Figure B-18). The results obtained from the near-field models are in qualitative agreement with the large-scale model but differ quantitatively:

- The more finely meshed models overestimate the shear displacement during the early stages of the modelling period but the final results are approximately the same.
- The more coarsely meshed model also overestimates the shear displacements during the early stages of the modelling but underestimates it during later stages of the modelling period.
- Gravity has a negligible influence on the results.
- The choice of fracture stiffness (50 GPa/m or 100 GPa/m) has a negligible influence on the results.

Influence of partial density scaling

General

Large dynamic models with complex fracture networks and small finite-difference elements can be very time consuming. Since one of the objectives of this study is to assess the influence of volumetric fracture intensity (P_{32}) on the slip of an optimally oriented target fracture, the 3DEC models should ideally include as many fractures as possible from the DFN models (e.g. Figure B-8) whilst minimizing the total calculation time. One approach is to introduce “partial density scaling” to increase the timestep (Itasca 2013). This approach allows for the user to manually set a timestep that is larger than the automatically determined one. The code then calculates and adds sufficient mass to certain gridpoints to compensate and achieve numerical stability (Itasca 2013). In this section, we investigate by how much the timestep can be increased (or rather how much additional mass can be introduced into the model) without influencing the results by any significant amount.

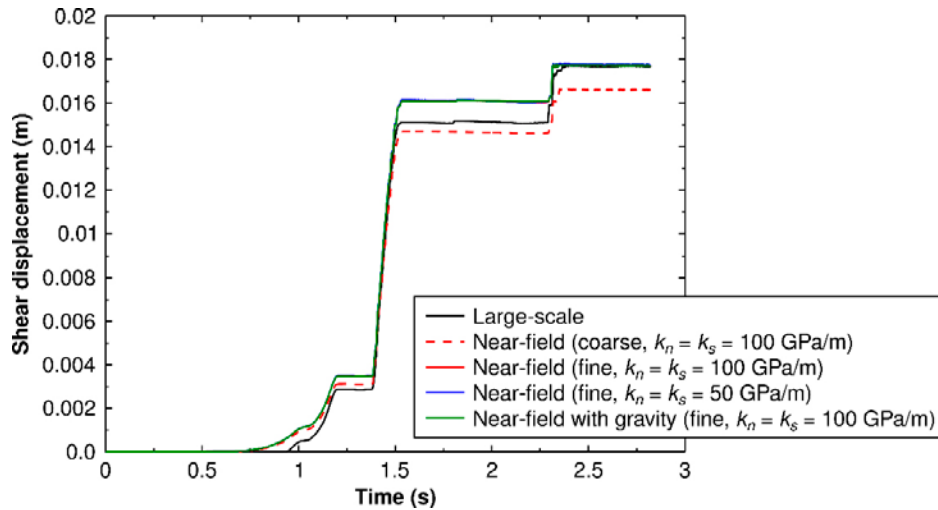


Figure B-18. Temporal evolution of the shear displacement at the centre of the target fracture. Comparison between results obtained from the large-scale model in Section 1.2 and the near-field model.

Description of model

For the purpose of testing the method of partial density scaling, we build a 3DEC model with a simplified version of the Forsmark DFN presented in Figure B-8. The input data (see Table B-2 and Table B-3) and meshing are the same as in Section 1.3 (except the minimum edge length, which is set at 4.25 m here). The simplifications are made to achieve a default timestep that results in an acceptable total calculation time (at most a few weeks).

The outline of the near-field model is a cube with side-length 400 m. It is subdivided into an outer region and an inner region (a cube with side-length 300 m) in which the target fracture and the DFN are implemented. Similarly to the model presented in Section 1.3, we include only the fractures that are fully contained within the inner region. The dip angles and dip directions of these fractures are rounded to the nearest integer multiple of 15° to avoid thin blocks with very small finite-difference elements.

The DFN fracture planes are inserted into the 3DEC model one by one starting with the largest fracture and continuing in descending order. A trial-and-error method is used to find a minimum block size (combination of minimum edge-lengths and minimum volumes) that in combination with meshing and other input data gives an acceptable default timestep. Fracture planes that split blocks into parts that are smaller than the acceptable minimum are removed from the DFN. The resulting DFN is presented in Figure B-19. This model has a default timestep of about 1.6×10^{-6} s and takes approximately two weeks to analyse. For comparison, the default timesteps in the models presented in Section 1.3 are between 6×10^{-9} s and 2×10^{-8} s.

Results

To test the influence of changes in the time step, we analyse additional models in which the timestep is increased to 1.0×10^{-5} s, 5.0×10^{-5} s, 7.5×10^{-5} s or 1.0×10^{-4} s. Two versions of the model are analysed for each timestep: one where the target fracture is isolated (i.e. the network is assigned fictitious high-strength properties to prevent slip) and one model where all DFN fractures are mechanically active. The increase in total mass and approximate total calculation times for each timestep are presented in Table B-7.

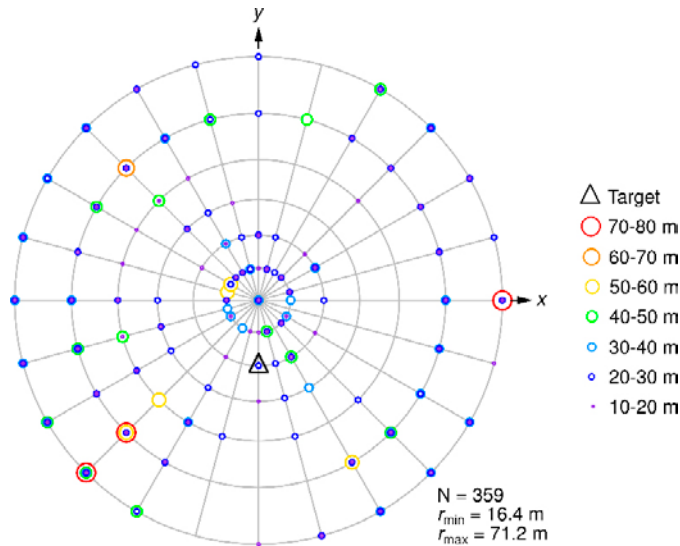


Figure B-19. Lower hemisphere equal angle projection of the simplified version of the Forsmark DFN implemented in the 3DEC model.

Table B-7. Summary of tested timesteps, the increase in total mass and approximate total calculation time per model.

Timestep (s)	Increase in total mass (%)	Approximate total calculation time (days)
1.6×10^{-6} (default)	-	13
1.0×10^{-5}	0.000068	2
5.0×10^{-5}	0.14	0.5
7.5×10^{-5}	1.3	0.3
1.0×10^{-4}	6.7	0.2

Figure B-20 shows the temporal evolution of the shear displacement at the centre of the target fracture for each of the tested timesteps. For these models, about 1% of mass can be added before the results are affected. This value is used as a guideline in Section 1.3 to determine suitable timesteps for the near-field models. Note, however, that no sensitivity analyses have been performed with regard to the size of the individual added masses or to their distribution within the model.

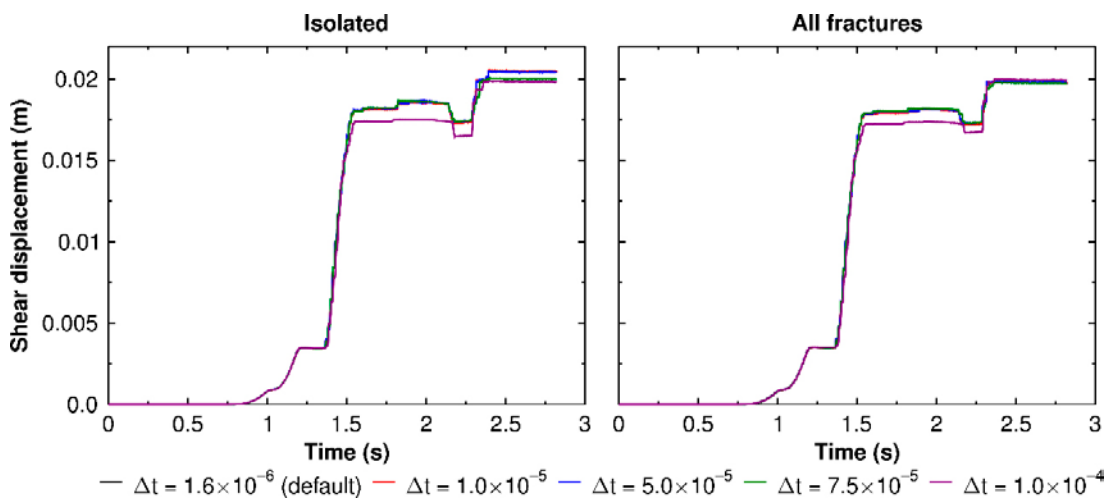


Figure B-20. Temporal evolution of the shear displacement at the centre of the target fracture in the isolated case (left) and with all DFN fractures mechanically active (right).

